Exotic Superfluidity in Imbalanced Fermi Mixtures

PhD thesis

Koos B. Gubbels

Koos Gubbels
Exotic Superfluidity in Imbalanced Fermi Mixtures
PhD thesis
Institute for Theoretical Physics
Utrecht University
ISBN: 978-90-3935267-0
Cover design by Roos d'Hont and Koos Gubbels
Printed by Gildeprint Drukkerijen, Enschede

Exotic Superfluidity in Imbalanced Fermi Mixtures

Exotische Superfluïditeit in Niet-gebalanceerde Fermi-mengsels

(met een samenvatting in het Nederlands)

Proefschrift

ter verkrijging van de graad van doctor aan de Universiteit Utrecht op gezag van de rector magnificus, prof.dr. J.C. Stoof, ingevolge het besluit van het college voor promoties in het openbaar te verdedigen op woensdag 13 januari 2010 des middags te 2.30 uur

door

Koos Bart Gubbels

geboren op 27 augustus 1982 te Tilburg

Promotor: Prof.dr.ir. H.T.C. Stoof

Dit proefschrift werd (mede) mogelijk gemaakt met financiële steun van de Stichting voor Fundamenteel Onderzoek der Materie (FOM) en de Nederlandse Organisatie voor Wetenschappelijk Onderzoek (NWO).

Parts of this thesis are directly based on refereed articles.

- Section 2.3 and Chapter 6 are based on: K. B. Gubbels and H. T. C. Stoof, *Theory for p-Wave Feshbach Molecules*, Phys. Rev. Lett. **99**, 190406 (2007).
- Section 2.4 is based on: K. B. Gubbels, D. B. M. Dickerscheid, and H. T. C. Stoof, *Dressed Molecules in an Optical Lattice*, New J. Phys. **8**, 151 (2006).
- Section 3.4 is based on: K. B. Gubbels, M. W. J. Romans, and H. T. C. Stoof, *Sarma Phase in Trapped Unbalanced Fermi Gases*, Phys. Rev. Lett. **97**, 210402 (2006).
- Chapter 4 is based on: K. B. Gubbels and H. T. C. Stoof, *Renormalization Group Theory for the Imbalanced Fermi Gas*, Phys. Rev. Lett. **100**, 140407 (2008).
- Chapter 5 is based on: K. B. Gubbels, J. E. Baarsma, and H. T. C. Stoof, *Lifshitz Point in the Phase Diagram of Resonantly Interacting ^6Li-^{40}K Mixtures*, Phys. Rev. Lett. **103**, 195301 (2009).

Other articles that the author has contributed to:

- J. M. Diederix, K. B. Gubbels, and H. T. C. Stoof, *Inhomogeneous Fermi Mixtures at Unitarity: Bogoliubov-de Gennes vs. Landau-Ginzburg*, arXiv:0907.0127, submitted to Phys. Rev. A.
- J. E. Baarsma, K. B. Gubbels, and H. T. C. Stoof, *Population and Mass Imbalance in Atomic Fermi Mixtures*, in preparation.
- K. Gubbels, G. Meijer and B. Friedrich, *Analytic wave model of Stark deceleration dynamics*, Phys. Rev. A **73**, 063406 (2006).

The author is also a co-author of the following textbook:

- H. T. C. Stoof, K. B. Gubbels, and D. B. M. Dickerscheid, *Ultracold Quantum Fields* (Springer, Dordrecht, 2009).

The Dutch summary is based on:

- Koos Gubbels, *Ultrakoude Fermi-mengsels zijn Super*, submitted to Nederlands Tijdschrift voor Natuurkunde.

Contents

Contents

Chapter 1

Introduction

The field of many-body quantum physics has a long history of fundamental discoveries, many of which have gone far beyond our wildest imagination. These include the study of novel states of matter, the observation of previously unseen phase transitions, and the discovery of new macroscopic quantum effects, which arise when the intriguing rules of quantum mechanics are no longer restricted to the subatomic world, but rather determine the collective behavior of systems that are observable with the naked eye. One of the first and most important examples that illustrates all of the above is the discovery of superconductivity by Kamerlingh Onnes [1]. In 1911, he found that the resistance of mercury suddenly dropped to zero at a temperature of about 4 K. It was not immediately realized that a macroscopic quantum effect caused superconductivity, an important reason being that quantum mechanics was only developed more than a decade later. In fact, it would take nearly half a century before superconductivity could be microscopically explained from first principles by Bardeen, Cooper and Schrieffer (BCS) [2], who showed that in particular the pairing of electrons plays a crucial role.

The fundamental mechanism of pairing occurs in nature when two particles stick together due to an attractive interaction. This attractive force may be strong, such that the pair is deeply bound and is hard to separate. The attraction may also be weak, such that the constituents of the pair are much further apart and already a slight disruption can break the pair up. The group behavior of pairs can be quite different from their individual behavior, which is particularly true for fermionic many-body systems. Here, pairing gives rise to a bosonic degree of freedom, whose statistics is freed from the Pauli principle that governs the behavior of the fermions. In particular, a macroscopic number of pairs can occupy the same single-pair quantum state, lifting this quantum state from the microscopic to the macroscopic world. The macroscopically occupied quantum state gives rise to the phase of matter known as a Bose-Einstein condensate (BEC), which was already predicted by Einstein in 1925 to occur in a noninteracting gas of bosons [3]. When Kapitsa, Allen and Misener discovered flow without friction

in the strongly interacting bosonic liquid ^{4}He in 1938 [4, 5], it took only a few months before a qualitative link between superfluidity and Bose-Einstein condensation was made by London [6].

However, in fermionic systems it took much more time before the link between superconductivity and condensation was noticed, such that only in 1956 the microscopic BCS theory of superconductivity was ultimately formulated. BCS theory showed that a weak attraction between electrons, mediated by the subtle mechanism of lattice vibrations in metals (phonons), caused the formation of loosely bound Cooper pairs, which could subsequently Bose-Einstein condense [2]. The BCS theory of pairing in Fermi mixtures revolutionized many-body quantum physics. It turned out to describe a very general mechanism that pops up under a wide range of circumstances. An important reason for this is that most of the matter in the world around us is made out of fermions, whether they are quarks, electrons, protons, neutrons, or more complicated composed particles, like fermionic atoms or molecules. Moreover, these fermions only need very little attraction to form Cooper pairs. Indeed, Cooper showed that an infinitesimal amount of attraction is enough in the presence of a Fermi sea [7]. As a result, paired condensates have been observed or predicted to occur not only in a wide range of condensed-matter systems, but for example also in ultracold atomic gases [8, 9] or in the cores of neutron stars [10, 11].

The BCS variational wavefunction itself also turned out to be much more general than initially expected. The many-body wavefunction was intended to describe the case of weak interactions between fermions that leads to the formation of loosely bound pairs, whose size is much larger than the average interparticle distance. This regime is also called the BCS limit. As realized by Eagles [12] and later by Leggett [13], the BCS Ansatz also describes the case of strong attraction between the fermions leading to the formation of tightly bound molecules, whose size is much smaller than the interparticle distance. This regime is also called the BEC limit. Eagles and Leggett predicted that the two extremes are continuously connected by a crossover, which was recently verified in a series of ground-breaking cold-atom experiments by the group of Jin using ^{40}K [9] and the groups of Ketterle, Thomas, Grimm, Salomon, and Hulet using ^{6}Li [14, 15, 16, 17, 18].

The crossover experiments could be performed in the field of atomic quantum gases, because they have the unique feature that the effective interparticle interaction strength can be varied over an infinite range by means of a so-called Feshbach resonance [19, 20]. In a Feshbach-resonant collision, two atoms collide and virtually form a long-lived molecule with a different spin configuration than the incoming atoms, after which the molecule ultimately decays into two atoms again. The two different spin configurations are also called the two different channels of the resonance, as explained more carefully in Chapter . The scattering properties of the colliding atoms depend very sensitively on the energy difference of the molecular state with respect to the threshold of the two-atom continuum, which can be changed with an applied magnetic field. The theoretical prediction for the presence of tunable resonances in alkali atoms [21] and their actual realization in experiments [22] have enormously enhanced the power and scope

of the experimental possibilities, especially in the case of ultracold Fermi mixtures. To illustrate this, we notice that already shortly after Bose-Einstein condensation was achieved in a dilute gas of bosonic alkali atoms by the group of Cornell and Wieman in 1995 [23], it was predicted that the superfluid regime could also be reached in a dilute mixture of fermionic atoms [8]. However, since the temperature for the BCS transition is exponentially suppressed for weak attractive interactions, the critical temperatures initially turned out to be beyond the reach of experiments with ultracold Fermi mixtures. By using Feshbach resonances the interaction could be effectively enhanced, which finally allowed for the observation of fermionic superfluidity and the BEC-BCS crossover.

The crossover physics is usually studied in a two-component Fermi mixture with an equal number of atoms in each of the two different spin states, the reason being that in this way a maximal number of Cooper pairs is created. This we can understand in the following way. At low temperatures, two particles predominantly interact through low-energy collisions for which the angular momentum is zero, also called s-wave collisions. Since for identical fermions the wavefunction should be anti-symmetric upon particle exchange, and since the two-particle wavefunction for s-wave scattering is symmetric in coordinate space, we conclude that s-wave interactions can only take place if the wavefunction is anti-symmetric in spin space. This is impossible to achieve if the particles only have access to one spin state. As a result, the fully polarized gas can typically be considered as noninteracting at ultralow temperatures, so that pairs between particles of the same spin are not formed. However, in the case of two spin states an anti-symmetric combination of the two spin states can be made and s-wave attractive interactions are possible. In the case of an equal amount of particles in both spin states, each particle can find another particle of a different spin to pair with, which leads to the formation of a superfluid after condensation of the pairs.

From the above discussion it becomes immediately clear that something interesting must happen as a function of spin imbalance or polarization, defined as $P = (N_+ - N_-)/(N_+ + N_-)$ with N_σ the number of particles in spin state σ. Indeed, since at ultralow temperatures the gas is in a superfluid state for a spin-balanced mixture with attractive interactions, while it is noninteracting and thus in the normal state for a fully polarized mixture, it must undergo a phase transition as a function of polarization. This transition is illustrated in Fig. 1.1. It was observed experimentally for the first time by the groups of Ketterle at MIT [24] and Hulet at Rice University [25], whose intriguing results induced a huge amount of experimental and theoretical activity. A main goal of this thesis is to achieve a detailed understanding of the phase diagram for the imbalanced Fermi mixture in the strongly interacting regime. Due to the generality of the pairing mechanism in fermionic many-particle systems, this topic is also of direct interest to condensed-matter, nuclear and astroparticle physics [11, 26].

Although in the past century an impressive amount of understanding about pairing in Fermi mixtures has been achieved, many questions still remain. An important example is the phenomenon of high-temperature superconductivity, which was discovered in a certain class of ceramic materials in 1986 [27]. Here, the microscopic nature of the

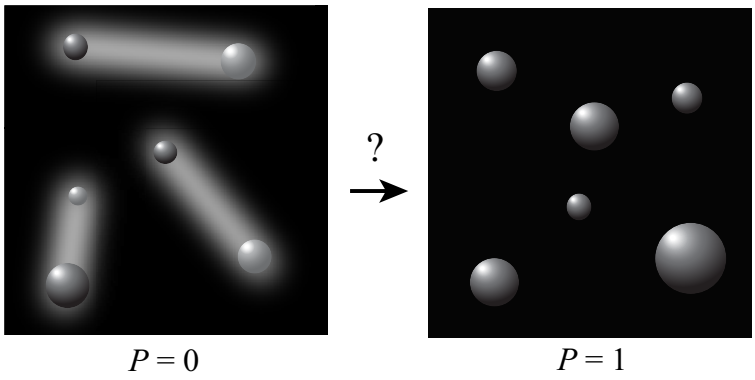

Figure 1.1: Illustration of the superfluid-to-normal transition as a function of polarization P in a two-component Fermi mixture. In the balanced case, $P = 0$, attractive interactions between particles of different spin allow for the formation of a Cooper-pair condensate. Since the fully polarized case, $P = 1$, can be considered noninteracting, it leads to the normal state. Obtaining a detailed understanding of the system's evolution between these two limits is an important goal of this thesis.

pairing has turned out to be one of nature's best kept secrets. In order to address the many remaining fundamental open questions that involve pairing in Fermi mixtures, it is extremely helpful to have a physical system that is experimentally very clean, highly tunable and easy to probe. Such a system then gives rise to a well-defined microscopic Hamiltonian, for which the interactions between the particles are accurately known. It is thus an ideal starting point for calculations of thermodynamic functions that govern the macroscopic properties of the system. These calculations go hand in hand with detailed experimental studies, where either experiments set benchmarks for sophisticated theoretical studies, or where theoretical predictions give rise to landmark experimental discoveries. In this way, a much more detailed understanding of fermionic superfluidity is achieved. Such a system is indeed nowadays available, namely in the field of ultracold atomic quantum gases. Whether the mystery of high-temperature superconductivity will ultimately be unravelled in the world of cold atoms still remains to be seen, but many fundamental discoveries have already followed each other up at a dazzling speed, while many more are likely to follow soon [28, 29, 30].

1.1 Ultracold atomic quantum gases

When a BEC was ultimately realized in trapped gases of bosonic atoms by the groups of Cornell and Wieman, Hulet, and Ketterle [23, 31, 32], a completely new category of systems for studying macroscopic quantum effects became available. A crucial ingredient for reaching BEC was the invention of laser cooling [33], with which atoms are made to absorb and emit photons such that a momentum transfer takes place. This

was used to create a friction force for atoms, slowing them down to a near standstill and thereby making the gas cloud enter the microKelvin regime. Equally important was the trapping of the atoms in a magnetic trap [34]. As a result, the gas could be held together without making contact to material walls that cannot be cooled to such ultralow temperatures. Moreover, the depth of the magnetic trap was easily lowered which allows the most energetic atoms to escape. If the remaining atoms undergo elastic collisions, then they re-thermalize at a lower temperature, allowing for an evaporative cooling of the trapped quantum gas [35]. This mechanism is similar to the way in which a cup of coffee gets cold during lunch time. Evaporative cooling turned out to be extremely efficient, allowing experimentalists to reach a temperature of 170 nK at a particle density of 2.5×10^{12} cm^{-3}, where BEC was finally observed [23]. Note that this means that an ultracold atomic quantum gas is typically about ten million times thinner than air. Moreover, it also means that a condensed gas of alkali atoms is strictly speaking in a metastable state, because at these ultralow temperatures the stable state is actually a solid. However, the solid formation takes so long on the time scales of the experiment, that we can consider the dilute gas to be in thermodynamic equilibrium.

Although the discovery of the Bose-Einstein condensed state of matter was extremely exciting in itself, it turned out to be only the beginning for the exploration of new macroscopic quantum effects in ultracold gases. A reason for the fruitfulness of atomic many-particle systems is their extreme cleanness, meaning that there are essentially no impurities in the experiments. This is in a sharp contrast to solid-state systems, where the understanding of many-body experiments can be extremely severed due to an uncontrolled amount of imperfections in the materials. Disorder in atomic gases is typically negligibly small, unless it is deliberately added as in the experiment by Billy *et al.* [36], which gave rise to a very controlled study of Anderson localization.

This brings us automatically to a second reason for the fruitfulness of degenerate quantum gases, namely the amazing amount of experimental control that is currently achieved [28]. We have already mentioned the two-channel Feshbach resonance with which the interatomic interaction strength can be tuned. Another important example of control is the external trapping potential of the gas cloud, which can be precisely tailored experimentally. A particularly convenient setup is achieved when the atoms are optically trapped with the use of the strong electric fields in laser beams. The laser beams can be made to counter-propagate each other, which leads to an intense standing wave of light. This creates a periodic potential for the atoms due to the Stark effect, giving rise to a so-called optical lattice [37]. Optical lattices can be used to simulate ionic lattices, which offers the opportunity to explore various aspects of condensed-matter physics in the very clean environment of ultracold atoms [29]. The depth of the periodic potential is now easily tunable by varying the laser intensity, while the period of the lattice is directly related to the frequency of the laser light. An even more flexible possibility to create arbitrary potential landscapes for the atoms is achieved by shining a laser onto a holographic mask [38].

In the so-called Hubbard model [39], a paradigm in condensed-matter physics, par-

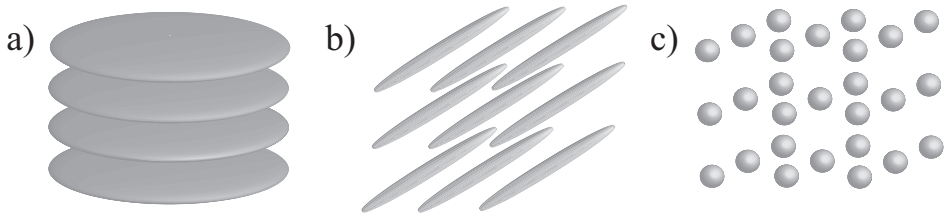

Figure 1.2: Sketch of several configurations that are realizable with optical lattices. a) If an intense standing wave of laser light is applied in one direction, then the potential landscape for the atoms becomes a stack of quasi-two-dimensional 'pancakes'. b) If a second standing wave is added in a perpendicular direction, then an array of quasi-one-dimensional 'cigars' arises. c) If counter-propagating laser beams are added in the third direction, then a lattice of point-like sites arises.

ticles are allowed to tunnel between adjacent lattice sites and they have an on-site interaction. When an interacting atomic gas at ultralow temperatures is loaded into an optical lattice, then an essentially perfect manifestation of the Hubbard model is realized. This was first shown theoretically by Jaksch *et al.* [40], who treated repulsively interacting bosons. Considering the case of an equal number of atoms and lattice sites, then the bosons are expected to form a delocalized superfluid state, when the tunnelling strength t is dominant. However, when the on-site interaction strength U is dominant, the ground state is given by the so-called Mott-insulator state, which has precisely one localized atom at each lattice site. At zero temperature, a transition occurs between these two phases as a function of t/U, which is solely driven by quantum fluctuations and not by thermal fluctuations [41]. It is thus called a quantum phase transition and it was observed in a landmark atomic physics experiment by Greiner *et al.* [42]. Here, the tunnelling strength was varied by simply changing the laser intensity. Note that an analogous control over the tunnelling would be hard to achieve in a condensed-matter system. An ultracold Fermi mixture can also be loaded into an optical lattice, which leads to a realization of the fermionic Hubbard model. In the absence of doping, this gives rise to the possibility of observing the anti-ferromagnetic Néel state [43]. Since the doped fermionic Hubbard model has been conjectured to encompass high-temperature d-wave superconductivity, it seems exciting to study this model in the controlled environment of ultracold atomic gases.

There are many more interesting applications of optical lattices. For example, they can be used to create low-dimensional quantum gases. Consider a lattice which is very deep in, let's say, the x direction, such that the ultracold particles can only occupy the lowest-lying quantum state with an energy $\hbar\omega_x/2$ in this direction. Then, the kinetic degrees of freedom are frozen out in the x direction, which effectively lowers the dimension of the system. In particular, with a very deep optical lattice in two directions it is possible to create a two-dimensional array of effectively one-dimensional tubes, while a very deep optical lattice in one direction leads to a one-dimensional stack

of two-dimensional pancakes, as shown in Fig. 1.2. Low-dimensional quantum gases are a universe of their own, giving rise to intriguing strongly correlated behavior that is very different from the three-dimensional case. Experimentally observed examples are the exotic Berezinskii-Kosterlitz-Thouless phase transition in two dimensional gases [44], or the thermodynamic behavior of exactly solvable models in one dimension [45].

But the control in ultracold atomic gases goes further. Feshbach resonances are for example not restricted to s-wave scattering, so that also resonances with higher angular momentum have been observed. This has led to the formation of p-wave Feshbach molecules [46], which upon condensation would give rise to superfluidity in a nonzero angular momentum state. Analogous to liquid ^{3}He, this superfluid has a more complex order-parameter structure [47], which may give rise to exotic features such as the presence of Majorana fermions in vortex excitations and topological quantum phase transitions [48, 49]. Another exciting line of research is the creation of condensates, where the particles interact through long-ranged anisotropic dipole-dipole interactions. Dipolar effects have already been observed in condensates of ^{52}Cr atoms [50], whose magnetic moment leads to weak dipole interactions. The interaction is much stronger for heteronuclear molecules that have a permanent electric dipole moment. An ultracold gas of ground-state ^{40}K^{87}Rb molecules has been achieved by associating ^{40}K and ^{87}Rb atoms using a Feshbach resonance and then optically pumping the ^{40}K^{87}Rb dimers to their rotational and vibrational ground state [51]. The interesting possibilities with dipolar molecules vary all the way from the stabilization of supersolid phases [52] to the possibility of quantum computing [53]. Another important example of control is the preparation of the atomic gas in a selective set of internal quantum states. In a two-component ^{6}Li mixture it is possible to precisely control the atom number in each of lithium's two lowest hyperfine states by inducing nuclear spin flips [24, 25]. As a result, the fundamental phase diagram of the two-component Fermi mixture can be studied as a function of temperature, polarization and interaction strength. Moreover, if two different atomic species are used, then a fourth axis enters the phase diagram, namely that of a mass imbalance.

To make a long story short, the possibilities seem endless and the field of ultracold atoms is able to address fundamental questions about many-body quantum physics in great detail. Therefore, atomic quantum gases are sometimes also referred to as ideal quantum simulators. They allow for systematic studies of an enormous variety of Hamiltonians, ranging from weakly interacting to strongly interacting, from one dimensional to three dimensional, from disordered to clean, from homogeneous to periodic, where the microscopic parameters are always precisely known and widely tunable.

1.2 The BEC-BCS crossover

As just discussed, if fermions in a different spin state attract each other, they have the tendency to form pairs, which may result in a paired condensate at ultralow temperatures [2, 8]. However, if these fermions repel each other, then they have the tendency

to align in spin space, leading to (itinerant) ferromagnetism [54, 55]. In this thesis, we consider the attractive case. Since in ultracold atomic gases the range of the interaction is typically very small compared to the interparticle distance, it is convenient to use a contact potential $V(\mathbf{r}) = V_0\delta(\mathbf{r})$ to incorporate interaction effects. The Fourier transform of the potential is then a constant, which leads to a particularly simple form of the Lippmann-Schwinger equation in momentum space [30]. We encounter this equation in Chapter 2, where we find that its solution is given in terms of the two-body transition matrix $\hat{T}^{2\mathrm{B}}$. The latter is directly related to the scattering cross section of the interacting particles, so that it can be seen as describing the effective interaction strength. For s-wave collisions, the transition matrix is at zero momentum and energy given by

$$\frac{1}{T^{2\mathrm{B}}(0)} = \frac{1}{V_0} + \frac{1}{\mathcal{V}}\sum_{\mathbf{k}}\frac{1}{2\epsilon_{\mathbf{k}}}, \tag{1.1}$$

where the kinetic energy of a particle with mass m and wavevector $\mathbf{k}$ equals $\epsilon_{\mathbf{k}} = \hbar^2k^2/2m$ and $\mathcal{V}$ is the volume of the system.[1] Note that the sum on the right-hand side of Eq. (1.1) is actually not convergent, which is caused by the anomalous behavior of the contact potential at high momenta. This is usually not a problem, since we are only interested in the low-energy properties of the interaction. Therefore, we can always use Eq. (1.1) to eliminate the contact potential from our theory in favor of the T matrix, which at zero energy is related to the s-wave scattering length a through $T^{2\mathrm{B}}(0) = 4\pi\hbar^2a/m$. This scattering length can be directly extracted from experiment, as we see in Chapter 2.

An equivalent approach to regularize the contact potential is to consider only wavevectors up to a certain cut-off Λ_0 for the sum in Eq. (1.1), after which we find

$$V_0 = \frac{4\pi\hbar^2a}{m}\frac{\pi}{\pi - 2a\Lambda_0}, \tag{1.2}$$

whose result is plotted in Fig. 1.3. The weakly interacting regime, where both a and V_0 are small and negative, is also called the BCS regime, since it is analogous to the weakly attractive case known from ordinary superconductors. In the BCS regime, the two-body potential is too weak to support a bound state, so that Cooper pairing is truly a many-body effect that occurs only in the presence of a Fermi sea [7]. The size of these Cooper pairs then turns out to be much larger than the interparticle distance. When $V_0 = -2\pi^2\hbar^2/m\Lambda_0$, we see that the scattering length diverges. This resonance in the cross section physically comes from a bound state that enters the attractive potential [56]. To see the latter more clearly, we can consider a slightly more realistic interaction potential, namely a square well. The exact solution to the resulting problem shows that, upon increase of the well depth, the scattering length diverges each time a new bound state enters the square-well potential [57]. Such resonances are called single-channel shape resonances. Note that it is not so clear how to tune a shape

[1] In actual analytical or numerical evaluations of the sum over states in $\mathbf{k}$-space, we make use of the continuum limit $\sum_{\mathbf{k}} 1/\mathcal{V} \to \int d\mathbf{k}/(2\pi)^3$.

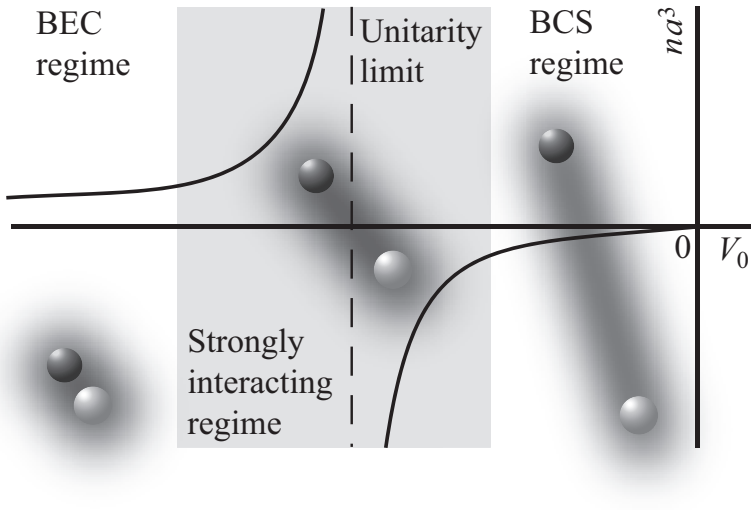

Figure 1.3: Schematic representation of the BEC-BCS crossover. In the BCS regime, the microscopic interaction strength, given by V_0, and the effective interacting strength, given by the scattering length a, are both negative and small, namely $|a| < n^{-1/3}$ with n the total particle density. Pairing is then a many-body effect and the size of the Cooper pairs is much larger than the average interparticle distance. When $|a| > n^{-1/3}$, we enter the strongly interacting regime. At $V_0 = -2\pi^2\hbar^2/m\Lambda_0$, the scattering length diverges, which is also called the unitarity limit. Here, the pair size is comparable to the interparticle distance. For stronger microscopic attractions, a two-body molecular bound state enters the interaction potential. When $|a| < n^{-1/3}$, we enter the BEC regime. The size of the molecules is here much smaller than the interparticle distance and the ground state of the system is a weakly interacting molecular Bose gas.

resonance experimentally, because it is usually not possible to precisely control the interatomic interaction potential. However, in Chapter 2, we discuss the more flexible mechanism of a two-channel Feshbach resonance, which is nowadays routinely used by experimentalists to vary the scattering length at will.

The region where the scattering length becomes infinite is commonly referred to as the unitarity limit. Here, the size of the Cooper pairs turns out to be comparable to the average interparticle distance. The unitary regime is also called the strongly interacting limit. This as opposed to the regime where the microscopic attraction has become so strong that there is a deep bound state in the interaction potential. As a result, bosonic molecules are formed, whose size is much smaller than the average interparticle distance. This regime is then called the BEC regime. It is unique that the complete evolution from the BEC regime to the BCS regime can be explored in ultracold quantum gases [28]. From Fig. 1.3 we might be surprised that the evolution merely leads to a crossover. Namely, the system is seen to evolve through a true resonance in the effective interaction strength, which we might have expected to profoundly

influence the thermodynamics of the mixture. Moreover, theoretical predictions based on perturbative approaches are expected to fail near resonance. This particularly holds for the mean-field BCS theory, which was used to predict the crossover. As a result, there has been a huge theoretical and experimental interest in the BEC-BCS crossover, and in particular in the behavior of the Fermi mixture in the unitary regime.

A second reason for the interest in the crossover is the beautiful unification of BEC-like superfluidity and BCS-like superfluidity as two-sides of the same coin. Both can be viewed as a coherent state (or Bose-Einstein condensate) of fermionic pairs, which is signalled by a nonzero expectation value of the pair annihilation operator, i.e. $\langle\hat{\psi}_-(\mathbf{R}+\mathbf{r}/2)\hat{\psi}_+(\mathbf{R}-\mathbf{r}/2)\rangle$. Here, we introduced the annihilation operator $\hat{\psi}_\sigma(\mathbf{x})$ for a single atom with spin σ at position $\mathbf{x}$, while $\mathbf{R}$ is the center-of-mass coordinate and $\mathbf{r}$ the relative coordinate of the pair. This puts us in the position to define the BCS order parameter Δ, given by

$$\begin{aligned}\langle\Delta(\mathbf{R})\rangle &= \int d\mathbf{r}\; V(\mathbf{r})\left\langle\hat{\psi}_-\left(\mathbf{R}+\frac{\mathbf{r}}{2}\right)\hat{\psi}_+\left(\mathbf{R}-\frac{\mathbf{r}}{2}\right)\right\rangle = V_0\langle\hat{\psi}_-(\mathbf{R})\hat{\psi}_+(\mathbf{R})\rangle \\ &= \frac{V_0}{\mathcal{V}}\sum_{\mathbf{K},\mathbf{k}}\langle\hat{\psi}_{\frac{\mathbf{K}}{2}+\mathbf{k},-}\hat{\psi}_{\frac{\mathbf{K}}{2}-\mathbf{k},+}\rangle e^{i\mathbf{K}\cdot\mathbf{R}}, \end{aligned} \tag{1.3}$$

where $\hbar\mathbf{K}$ is the center-of-mass momentum and $\hbar\mathbf{k}$ is the relative momentum. Because Eq. (1.3) is seen to involve an integral over the attractive interaction, the order parameter also describes the energy cost to break up a Cooper pair. For this reason, $\langle\Delta(\mathbf{R})\rangle$ is also referred to as the (local) pairing gap. Usually, the paired state of lowest energy is at zero momentum, $\hbar\mathbf{K}=0$, which upon pair condensation gives rise to an order parameter that is spatially independent, namely

$$\langle\Delta\rangle = \frac{V_0}{\mathcal{V}}\sum_{\mathbf{k}}\langle\hat{\psi}_{\mathbf{k},-}\hat{\psi}_{-\mathbf{k},+}\rangle. \tag{1.4}$$

The equation above reveals that in this case the Cooper pairing occurs in momentum space between particles of opposite spin and momentum.

1.3 Exotic superfluidity and this thesis

Although in three dimensions the formation of a BEC typically goes hand in hand with the onset of superfluidity, they are not identical phenomena. For example, the enhancement of fluctuation effects in lower dimensions can destroy the condensate while keeping the property of superfluidity intact. Moreover, in three dimensions the ideal Bose gas is fully condensed at zero temperature, but it is usually not considered to be a superfluid. The latter is because its critical velocity, which is the highest velocity for the gas to flow without friction, turns out to be zero. However, in this thesis we only consider the interacting three-dimensional case, such that we use the terms Cooper-pair condensate and superfluid state interchangeably. In particular, we are interested

in the onset of pair condensation in various experimentally relevant situations that differ fundamentally from the well-studied BCS-like case. The latter is characterized by weak s-wave interactions between identical particles in two different spin states that are equally populated. The first example we encounter of such a different situation is when there is a population imbalance between the two spin states of the Fermi mixture, so that not all particles can find a partner to pair up with. This was realized in the landmark experiments at MIT by Zwierlein *et al.* [24] and at Rice University by Partridge *et al.* [25]. Pairing in imbalanced Fermi mixtures is a topic of fundamental interest to various areas of physics [11, 26], where we can think of neutron-proton pair condensation in nuclear physics [58], or color superconductivity of strongly degenerate quark matter in the core of neutron stars [10].

In Chapters 3 and 4, we study the phase diagram of the spin-imbalanced mixture in the unitarity limit, where we consider both the presence and the absence of a trapping potential. Due to the richness of the system, we encounter two additional superfluid phases that are not present in the spin-balanced case. First of all, we find the occurrence of a phase-separated phase at temperatures close to zero. This phase can arise because there is a discontinuous or first-order transition in the system between a superfluid state that has a small polarization and a normal state that has a high polarization. The phase-separated state then occurs when the total polarization of the system is in between these two extremes. As a result, the system spatially separates into a superfluid region and a normal region, between which there is a first-order interface, i.e. a domain wall. In the presence of a trap, the superfluid region is then found in the center of the trap, while the normal region surrounds it. The second exotic phase occurs at higher temperatures, where we find that the excitation spectrum of the superfluid can become gapless. The resulting polarized superfluid phase is called the Sarma phase [59, 60], because Sarma first considered this possibility in the context of weakly interacting superconductors. Sometimes the phase is also referred to as the interior-gap phase or the breached-pair phase [61, 62, 63]. The Sarma phase remains a polarized superfluid even at zero temperature, where the gapped BCS phase is unpolarized. However, the Sarma phase unfortunately becomes unstable at very low temperatures, preventing the observation of the quantum phase transition between the gapped BCS and the gapless Sarma superfluid. At nonzero temperatures, where we find that the Sarma phase is stabilized, it is connected to the BCS regime via a crossover.

Another exciting possibility, which we explore in Chapter 5, is that there is not only a population imbalance, but also a mass imbalance between the two different components in the Fermi mixture. This situation is being explored by various experimental groups [64, 65, 66], although pair condensation with different masses has not been observed yet. We study the phase diagram for the ^{6}Li-^{40}K mixture, which is currently the experimentalist's favorite. The phase diagram of this mixture not only encompasses all the exciting physics known from the mass-balanced case, but is even much richer. Namely, next to the presence of Sarma physics and phase separation, we find also a Lifshitz point in the phase diagram. At this point the effective mass of the Cooper pairs turns negative, which signals a transition to an inhomogeneous

superfluid. This exotic possibility was early investigated for the mass-balanced case by Larkin and Ovchinnikov (LO) [67], who considered a superfluid with a standing-wave order parameter, namely $\langle\Delta(\mathbf{R})\rangle = \Delta_0 \cos(\mathbf{K}\cdot\mathbf{R})$. The order parameter spontaneously breaks translational symmetry, and because the atom densities depend on the absolute value of the superfluid order parameter, the densities also oscillate in space. The combination of superfluidity with crystalline order in the densities makes the LO phase a supersolid [68, 69]. Moreover, the phase is energetically more favorable than a plane-wave order parameter $\langle\Delta(\mathbf{R})\rangle = \Delta_0 e^{i\mathbf{K}\cdot\mathbf{R}}$, which was considered independently by Fulde and Ferrell (FF) [70]. The FF phase leads to a propagating superfluid that spontaneously beaks time-reversal symmetry, while it does not give rise to oscillating particle densities. Both the FF and LO phases have intrigued the condensed-matter community for many decades, but it has been experimentally very challenging to prove their existence unambiguously [11]. The same holds for supersolidity in general, where a famous example is the heavily debated experiment with ^{4}He by Kim and Chan [71].

A last example of exotic superfluidity that we consider theoretically is the condensation of atoms into a paired state with nonzero angular momentum ℓ. Pair formation with $\ell \neq 0$ can be strongly enhanced near a corresponding Feshbach resonance, so that pairs ranging from p-wave symmetry ($\ell = 1$) all the way to l-wave symmetry ($\ell = 8$) have been observed [46, 72]. Unfortunately, condensation of such pairs has not been achieved yet in ultracold atomic gases mainly due to limited lifetimes [46]. In Chapter 6, we consider the possibility of superfluidity in a fully polarized Fermi gas close to a p-wave Feshbach resonance. If the condensation of pairs with angular momentum ℓ occurs in a state of specific projection m_ℓ, then we obtain an angular-dependent order parameter given by $\Delta_{\ell,m_\ell} Y_{\ell,m_\ell}(\vartheta,\varphi)$, where Y_{ℓ,m_ℓ} is the corresponding spherical harmonic. As a result, the superfluid order parameter can become zero at the Fermi surface in certain directions, giving rise to an excitation spectrum with gapless nodes. Interestingly, if we now study the evolution from the BEC to the BCS side of the p-wave Feshbach resonance, then it is not a crossover anymore at zero temperature, so that a true quantum phase transition occurs [48, 49]. Moreover, if an atomic quantum gas is superfluid close to a two-channel Feshbach resonance, then it is possible to study coherent Rabi or Josephson oscillations between the superfluid components in each of the two channels [57, 73]. By studying the frequency of these oscillations near the p-wave resonance, we find a clear signature of the quantum phase transition that can be observed in experiments.

Chapter 2

Scattering theory

In this chapter, we look in detail at elastic scattering of two interacting particles. The discussion forms the basis for later chapters, where interacting many-body systems are considered. We start out with recapitulating the machinery of scattering theory that is of most relevance to us. This puts us then in the position to discuss two-channel Feshbach resonances, which provide an extremely useful tool for experimentally controlling the scattering cross sections. Physically, a Feshbach resonance in the scattering of two atoms arises from the coupling with a bound molecular state $|\psi_{\rm m}\rangle$ that has a different spin configuration than the colliding atoms. As a result, this molecule is said to be in a different channel than the scattering atoms, which are described by $|\psi_{\rm aa}\rangle$. In general, the eigenstates of the coupled Feshbach problem are linear superpositions of $|\psi_{\rm m}\rangle$ and $|\psi_{\rm aa}\rangle$, where the amplitude in the molecular channel is called Z. We focus in first instance on collisions with zero angular momentum ($\ell = 0$), also called s-wave scattering. As an example of particular interest, we look at the widely used s-wave Feshbach resonance of ^{6}Li at a magnetic field strength of 834 G. We determine Z near this extremely broad resonance and find that it is very small for a wide region in magnetic field strength. As a result, we may use in later chapters the so-called single-channel model for this Feshbach resonance, which means that the presence of the barely populated molecular state is ignored, except for its effect on the two-body scattering properties. The resonance at 834 G is the one that is used for the experiments on the spin-imbalanced ^{6}Li mixtures that we discuss in Chapters 3 and 4.

Having obtained a detailed understanding of s-wave resonances puts us in the position to also consider resonances of higher angular momentum, where we focus in first instance on p-wave scattering ($\ell = 1$). In particular, we determine the physical properties of Feshbach molecules near a p-wave resonance in fully spin-polarized ^{40}K and compare the results with experiments by Gaebler *et al.* [46]. We show that for p-wave resonances, the amplitude Z to be in the molecular channel is actually large. As a result, the single-channel model does not apply. In Chapter 6, we then discuss

an explicit example of interesting two-channel many-body physics near a p-wave resonance. Finally, we treat the two-body s-wave Feshbach problem in a harmonic trap. It is of interest, because external harmonic potentials are applied experimentally to confine the atomic gas clouds in space. Nowadays many experiments also make use of optical lattice potentials to study solid-like behavior. To a good approximation, each site in such a lattice also gives rise to a harmonic potential for the particles. Therefore, our obtained solution is of practical importance to lattice experiments near a Feshbach resonance.

2.1 Single-channel scattering

Consider two particles of mass m that scatter elastically from each other under the influence of an interaction potential $V(\mathbf{r})$ that depends on the relative coordinate $\mathbf{r}$ of the particles. If the Schrödinger equation is now separated into a part describing the center-of-mass motion and a part describing the relative motion of the two particles, then the center-of-mass part behaves like a single free particle of mass $2m$, while the relative part behaves like a single particle with reduced mass $m/2$ moving in a potential $V(\mathbf{r})$. The machinery to deal with scattering problems has been well established and can be found in most textbooks on quantum mechanics [74, 75, 76]. Here, we only briefly state the results that are of most relevance to us. Starting point is the relative Schrödinger equation

$$\left\{\hat{H}_0 + \hat{V}\right\}|\psi\rangle = E|\psi\rangle, \tag{2.1}$$

where we have that $\hat{H}_0 = -\hbar^2\boldsymbol{\nabla}^2/m$ for the relative kinetic-energy operator. We start by looking at solutions that have the particles entering the scattering region in a plane wave state $|\mathbf{k}\rangle$ with energy $E = \hbar^2k^2/m = 2\epsilon_{\mathbf{k}}$, which is conserved in the elastic collision. The state $|\mathbf{k}\rangle$ also solves the problem in the absence of the interaction potential. Since Eq. (2.1) is the time-independent Schrödinger equation, it may be interpreted as describing a steady-state solution for a continuous stream of particles in state $|\mathbf{k}\rangle$ scattering from a potential. It turns out to also describe the scattering of wavepackets, provided that the typical wavelength of the packets is much larger than the range of the interaction [75]. This condition is typically well satisfied for ultracold atoms, which have very large de Broglie wavelengths. Moreover, we consider interactions that are short ranged, which is a particularly valid assumption in the case of dilute atomic quantum gases where the range of the interatomic interaction is much smaller than the interparticle distance or the typical wavelength of the colliding atoms.

Eq. (2.1) can be formally solved by introducing scattering states $|\psi^{(+)}_{\mathbf{k}}\rangle$ that satisfy the following recursion relation, also known as the Lippmann-Schwinger equation,

$$|\psi^{(+)}_{\mathbf{k}}\rangle = |\mathbf{k}\rangle + \hat{G}_0(2\epsilon_{\mathbf{k}})\hat{V}|\psi^{(+)}_{\mathbf{k}}\rangle, \tag{2.2}$$

where $\hat{G}_0(2\epsilon_{\mathbf{k}}) \equiv (2\epsilon_{\mathbf{k}} - \hat{H}_0 + i0)^{-1}$ with the infinitesimal positive imaginary part being the standard way to treat the singular nature of the operator. In a time-dependent

formulation, this limiting procedure follows immediately from demanding that the particles were free in the remote past [75]. In scattering theory a central role is played by the two-body transition matrix, defined through $\hat{V}|\psi_{\mathbf{k}}^{(+)}\rangle \equiv \hat{T}^{2\mathrm{B}}(2\epsilon_{\mathbf{k}})|\mathbf{k}\rangle$. As a result, Eq. (2.2) leads to

$$\hat{T}^{2\mathrm{B}}(2\epsilon_{\mathbf{k}})|\mathbf{k}\rangle = \left\{\hat{V} + \hat{V}\hat{G}_0(2\epsilon_{\mathbf{k}})\hat{T}^{2\mathrm{B}}(2\epsilon_{\mathbf{k}})\right\}|\mathbf{k}\rangle. \tag{2.3}$$

This form of the Lippmann-Schwinger equation can also be generalized to an operator equation, whose recursive solution gives rise to the so-called Born series

$$\hat{T}^{2\mathrm{B}}(z) = \hat{V} + \hat{V}\hat{G}_0(z)\hat{V} + \hat{V}\hat{G}_0(z)\hat{V}\hat{G}_0(z)\hat{V} + \ldots, \tag{2.4}$$

where in general z is now allowed to be complex. More shortly,

$$\hat{T}^{2\mathrm{B}}(z) = \hat{V} + \hat{V}\hat{G}(z)\hat{V}, \tag{2.5}$$

where $\hat{G}(z) = (z - \hat{H}_0 - \hat{V})^{-1}$. The last equation indicates that singularities in the transition matrix are found at the exact eigenenergies of the two-body problem.

More insight is gained by realizing that away from the scattering region the influence of the scattering potential becomes negligible, which leads to a noninteracting radial Schrödinger equation. Here, we demand that the solution describes an incoming plane wave with wavevector $\mathbf{k}$ and a freely propagating outward radial flow of probability flux. It is possible to show that the solution behaves for large $\mathbf{r}$ as [30]

$$\psi_{\mathbf{k}}^{(+)}(\mathbf{r}) \simeq e^{i\mathbf{k}\cdot\mathbf{r}} + f(\mathbf{k}', \mathbf{k})\frac{e^{ikr}}{r}, \tag{2.6}$$

where $\mathbf{k}' = k\hat{\mathbf{r}}$, and where the scattering amplitudes satisfy [30]

$$\begin{aligned} f(\mathbf{k}', \mathbf{k}) &= -\frac{m}{4\pi\hbar^2}\langle\mathbf{k}'|\hat{V}|\psi_{\mathbf{k}}^{(+)}\rangle = -\frac{m}{4\pi\hbar^2}\langle\mathbf{k}'|\hat{T}^{2\mathrm{B}}(2\epsilon_{\mathbf{k}})|\mathbf{k}\rangle \\ &= \sum_{\ell=0}^{\infty}(2\ell+1)f_\ell(k)P_\ell(\cos\vartheta) = -\sum_{\ell=0}^{\infty}\frac{(2\ell+1)m}{4\pi\hbar^2}T_\ell^{2\mathrm{B}}(k)P_\ell(\cos\vartheta). \end{aligned} \tag{2.7}$$

In the second line the partial-wave method was employed to expand the scattering amplitude and the transition matrix, where $P_\ell(x)$ are the Legendre polynomials and ϑ is the angle between $\mathbf{k}$ and $\mathbf{k}'$ [75, 76]. We note that in obtaining the expression of Eq. (2.7) the normalization $\langle\mathbf{r}|\mathbf{k}\rangle = e^{i\mathbf{k}\cdot\mathbf{r}}$ was used for the plane waves [30]. This actually means that the ket $|\mathbf{k}\rangle$ itself is not dimensionless, which is a direct result of using the continuum limit for the states in $\mathbf{k}$ space. Moreover, the expansion in Eq. (2.7) is useful for a spherically symmetric interaction, for which the scattering problem is symmetric around the axis of incidence. From the conservation of angular momentum and probability flux, it follows that [75]

$$f_\ell(k) = \frac{1}{k\cot[\delta_\ell(k)] - ik}, \tag{2.8}$$

where $\delta_\ell(k)$ is the phase shift of the ℓ-th partial wave due to the elastic scattering.

At low energies, the phase shift is governed by the expansion [74]

$$k^{2\ell+1}\cot[\delta_\ell(k)] = -\left(\frac{1}{a_\ell}\right)^{2\ell+1} + \mathcal{O}(k^2), \tag{2.9}$$

so that for small wavevectors the partial scattering amplitudes behave as $f_\ell(k) \simeq -a_\ell^{2\ell+1}k^{2\ell}$ with a_ℓ the so-called scattering length of the ℓ-th partial wave. This means that at low momenta the scattering with zero angular momentum ($\ell = 0$) is dominant, which is also called s-wave scattering. The reason why collisions with higher angular momentum are suppressed is also readily understood from a more physical point of view. Namely, for $\ell \neq 0$ the relative radial Schrödinger equation contains a repulsive centrifugal term $\hbar^2\ell(\ell+1)/mr^2$, which acts as an energy barrier. At low temperatures the particles do not have enough kinetic energy to overcome this barrier and thus the higher-order partial waves do not feel the short-ranged interaction. These waves behave as if the interaction potential were not there, giving rise to quickly vanishing phase shifts. For s-wave scattering, we have for the scattering length

$$a_0 = -\lim_{k\to 0}\frac{\delta_0(k)}{k}. \tag{2.10}$$

Moreover, we find from Eq. (2.8) that $f_0(0) = -a_0$ and from Eq. (2.7) that $T_0(0) = 4\pi\hbar^2 a_0/m$. In the specific case of a hard-core potential, the scattering problem can easily be solved analytically, which leads to the s-wave scattering length being equal to the radius of the impenetrable core [57]. Therefore, in general a positive s-wave scattering length can be interpreted as the the effective hard-core radius of the interaction. For $\ell = 1$, or p-wave scattering, we have that

$$a_1^3 = -\lim_{k\to 0}\frac{\delta_1(k)}{k^3}, \tag{2.11}$$

where a_1^3 is also often called the scattering volume [49]. From Eq. (2.8) it then follows that for small momenta $f_1(k) = -a_1^3k^2$ and from Eq. (2.7) that $T_1(k) = 4\pi\hbar^2 a_1^3 k^2/m$. This again shows that at ultralow temperatures p-wave scattering is strongly suppressed compared to s-wave scattering.

As already mentioned in the Introduction, it is important to note that the solution to the radial Schrödinger equation with no angular momentum is symmetric in real space. This is most clearly seen if we write the scattering wave with $\ell = 0$ at large $\mathbf{r}$ in the following way [76]

$$\psi_{\mathbf{k}}^{(+)}(r) \simeq \frac{\sin\left[kr + \delta_0(k)\right]}{kr}, \tag{2.12}$$

which only depends on $|\mathbf{r}|$. If the two particles are interchanged, such that the relative coordinate changes sign, then the wavefunction stays the same. However, for two identical fermions the total wavefunction should be antisymmetric under particle exchange.

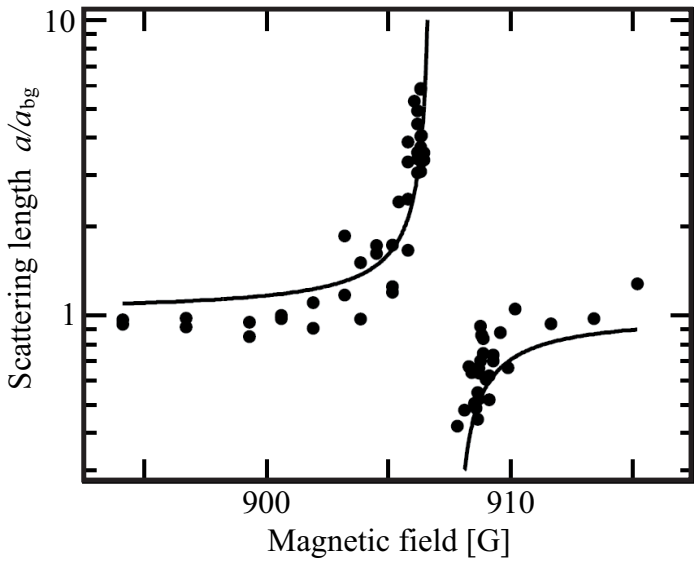

Figure 2.1: The scattering length a as a function of magnetic-field strength, measured in a gas of ^{23}Na atoms. Near the resonance at 907 G, the scattering length is seen to diverge. Far from resonance, it approaches the background value a_{bg}. Adapted from Ref. [22].

As a result, fermions that are in the same spin state do not undergo s-wave scattering. If there is more than one spin state available, then the wavefunction for the two fermions can be made antisymmetric in spin space. As a result, the total wavefunction is now allowed to be symmetric in real space and s-wave scattering between particles of different spin can occur. Identical fermions can interact via p-wave scattering, although this is typically a very weak effect at low temperatures. An exception to this rule occurs close to a p-wave Feshbach resonance, which we discuss in Section 2.3 and Chapter 6.

2.2 Feshbach resonances

In the previous section the transition matrix was introduced, which gives access to an exact knowledge of the system's interacting properties, such as the scattering amplitudes. Moreover, we saw that at low energies the transition matrix is dominated by the s-wave scattering length, which can therefore be interpreted as giving the effective interaction strength. As a result, the scattering length is an extremely useful quantity to know in the description of ultracold atomic gases. The calculation of the scattering length from first principles can be a tedious task for atomic collisions, also because the atomic interaction potentials are typically not very accurately known. Fortunately, the scattering length can be directly measured experimentally as shown in Fig. 2.1. In this experiment by Inouye *et al.* [22], the scattering length for collisions of ^{23}Na atoms was investigated near a magnetic-field strength of 907 G. The experimental data

shows a pronounced resonance, which implies a tunability of the effective interaction strength over an infinite range by varying the applied magnetic field. The mechanism that allows for this extremely useful control is nowadays called a Feshbach resonance [19], due to the analogy with Feshbach's analysis of two-channel resonances in nuclear physics. In atomic physics, two-channel resonances were first discussed by Stwalley in his study of stable hydrogen and deuterium [20], where he warned to avoid the regions of magnetic-field strength near resonance. Feshbach resonances were re-discovered in collisions of alkali atoms by Tiesinga, Verhaar and Stoof [21], who were also the first to realize their usefulness for experiments. In this section we discuss the two-body physics near a Feshbach resonance along the lines of the approach by Duine and Stoof, which is explained in detail in Ref. [57]. More recent reviews about Feshbach resonances can be found in Refs. [28, 77].

In an atomic Feshbach-resonant collision, two alkali atoms collide and virtually form a long-lived molecule with a different spin configuration than the incoming atoms, where the molecule ultimately decays into two atoms again. The scattering properties of the colliding atoms depend very sensitively on the energy difference of the molecular state with respect to the threshold of the two-atom continuum, which can be changed with an applied magnetic field. The reason for the latter is that the difference in spin states between the incoming atoms and the molecule lead to a different Zeeman shift. To further quantify the above physical discussion, we study a two-channel model as illustrated in Fig. 2.2. The atoms approach each other in the atomic channel, while there is a bound state close to the threshold of the atomic continuum in the molecular channel. We are interested in the regime where the collisional energy is lower than the Zeeman splitting, so that due to energy conservation the molecular channel is inaccessible for the atoms at large separations from each other after the collision. Therefore, the molecular channel is also called the closed channel, while the atomic channel is called the open channel. We consider only the bound state in the molecular channel that is closest to the atomic continuum, since this state is dominant in affecting the scattering process.

In the absence of a coupling between the channels, the molecule is described by the wavefunction $|\psi_{\mathrm{m}}\rangle$, which we call the bare molecular state, and has an energy δ_{B}, which we call the bare detuning. The bare molecular state and the bare detuning are only a solution to the uncoupled Schrödinger equation in the closed channel. This is to be contrasted with the so-called dressed molecular state, which is the bound-state solution when the two channels are coupled. In the open channel the two atoms interact through a short-ranged potential $\hat{V}_{\mathrm{bg}}$, which depends on their relative coordinate $\mathbf{r}$ and which is called the background interaction. The atomic and the molecular channel are coupled by $\hat{V}_{\mathrm{am}}$ due to the possibility of electronic spin flips caused by hyperfine interactions. To find the energy and the wavefunction of the dressed molecule, the two-body problem is separated into a center-of-mass part and a relative part. The center-of-mass part gives rise to a trivially solvable free-body problem, while the relative Schrödinger equation

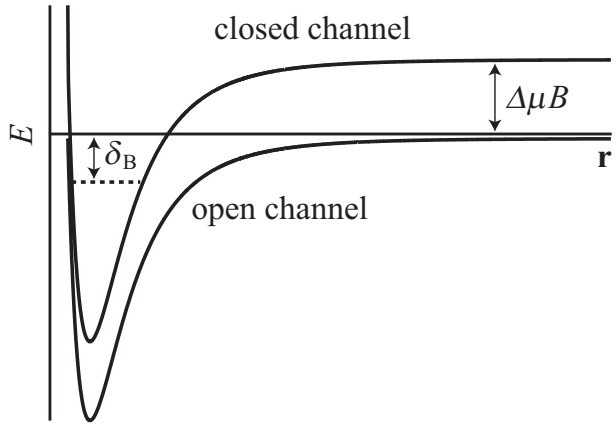

Figure 2.2: Illustration of the two-channel structure of a Feshbach resonance. Shown are the atomic or open channel and the molecular or closed channel in the absence of a coupling between the two. The interaction potential in the open channel is called the background interaction $V_{\rm bg}(\mathbf{r})$, which depends on the interatomic separation $\mathbf{r}$. The relevant feature of the closed channel is a bound state, also called the bare molecular state, that has a small energy difference $\delta_{\rm B}$ with the atomic continuum. Due to a different spin configuration of the atoms in the two channels, there is a Zeeman shift of $\Delta\mu B$ with $\Delta\mu$ the difference in magnetic moments and B the magnetic-field strength.

becomes

$$\begin{pmatrix} \hat{H}_0 + \hat{V}_{\rm bg} & \hat{V}_{\rm am} \\ \hat{V}_{\rm am} & \delta_{\rm B} \end{pmatrix} \begin{pmatrix} \sqrt{1-Z}|\psi_{\rm aa}\rangle \\ \sqrt{Z}|\psi_{\rm m}\rangle \end{pmatrix} = E \begin{pmatrix} \sqrt{1-Z}|\psi_{\rm aa}\rangle \\ \sqrt{Z}|\psi_{\rm m}\rangle \end{pmatrix}, \tag{2.13}$$

where $|\psi_{\rm aa}\rangle$ denotes the wavefunction in the atomic channel, $|\psi_{\rm m}\rangle$ is the wavefunction of the bare molecular state, Z is the so-called wavefunction renormalization factor that normalizes the wavefunction of the dressed molecule to unity, and $\hat{H}_0 = -\hbar^2\nabla^2_{\mathbf{r}}/m$ is again the relative kinetic energy operator.

In this section we consider only s-wave scattering, while in the next section we discuss p-wave resonances. As explained in the previous section, s-wave scattering of fermions only occurs between particles in two different internal states. In the experiments with ^{6}Li of interest to us, a two-component mixture is prepared in the lowest two hyperfine states of the ground state. They are denoted by $|1\rangle$ and $|2\rangle$, which are shown in Fig. 2.3(b). Ultracold ^{6}Li is an experimentalist's favorite due to the easily accessible Feshbach resonance at a magnetic-field strength of $B_0 = 834$ G, which is extremely broad. The resonance is shown in Fig. 2.3(a). Near 834 G, the two lowest lying hyperfine states have the single valence electron of lithium anti-aligned with the applied magnetic field, i.e. $m_{\rm s} = -1/2$ [78]. These states then differ in their projection of the nuclear spin. If two incoming atoms in state $|1\rangle$ and $|2\rangle$ collide, then the electronic spins of the atoms point in the same direction, so that the open channel gives rise to a spin triplet potential. During the collision an electronic spin can be flipped, which

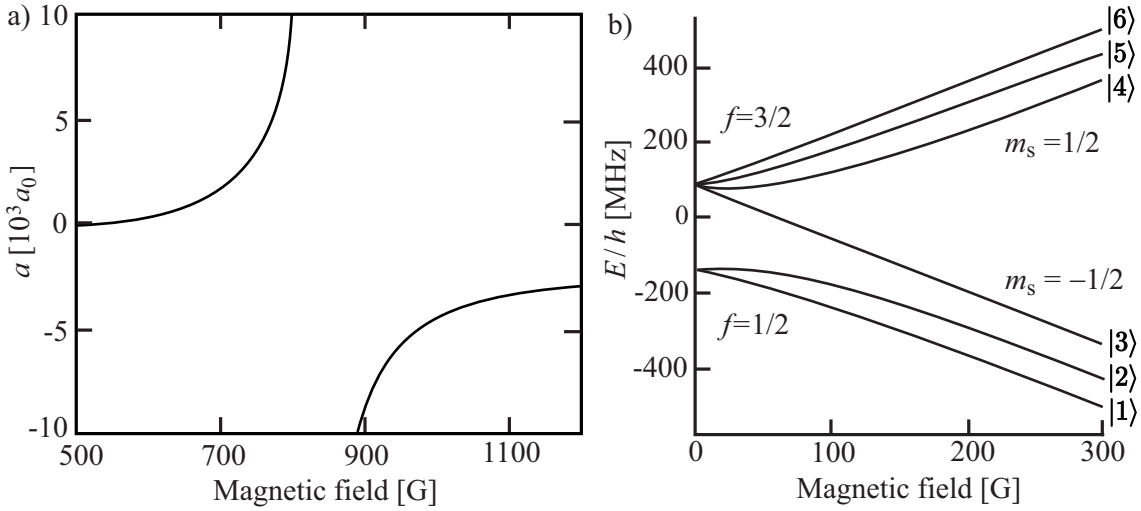

Figure 2.3: a) The scattering length as a function of magnetic-field strength near the very broad resonance of ^{6}Li at 834 G. It is given in terms of the Bohr radius a_0. b) Hyperfine structure of the electronic ground state in ^{6}Li as a function of magnetic-field strength, where E is the internal energy and h is Planck's constant. The nuclear spin of ^{6}Li is given by $i = 1$, so that the spin of the outer electron gives rise to $f = 3/2$ or $f = 1/2$ for the total angular momentum. At large magnetic-field strength, the hyperfine energies are predominantly determined by the projection m_s of the electron spin. The experiments with imbalanced spin mixtures that we consider later on in this thesis, are performed with states $|1\rangle$ and $|2\rangle$.

brings the two atoms in the closed spin singlet channel. The difference in magnetic moments between the two channels is $\Delta\mu = 2\mu_B$ with μ_B the Bohr magneton. As we increase the magnetic-field strength B from the resonance strength B_0, then the triplet potential is lowered in energy by an amount $\delta = \Delta\mu(B - B_0)$, which shifts the atomic continuum down with respect to the bare molecular bound state as shown in Fig. 2.4. Equivalently, we can also say that the bare molecular bound-state energy δ_B has been raised by δ with respect to the atomic continuum. The difference in Zeeman energy from the resonance position is also called the (experimental) detuning δ. As a result, the bare detuning δ_B varies linearly with the experimental detuning δ, although they are not the same. As we may infer from Fig. 2.4 and as we also show next, they are separated by a constant shift.

2.2.1 Dressed molecules

We continue by looking for negative energy solutions of Eq. (2.13), meaning that we want to find the wavefunction and the energy of stable dressed molecules. We start by rewriting Eq. (2.13) to obtain the following equation

$$\langle\psi_m|\hat{V}_{am}\hat{G}_a(E)\hat{V}_{am}|\psi_m\rangle = E - \delta_B, \tag{2.14}$$

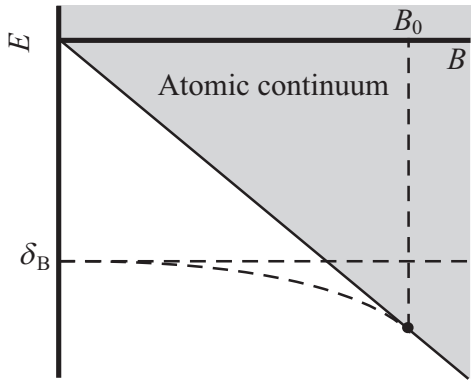

Figure 2.4: Schematic representation of the physics near the resonance at $B_0 = 834$ G of ^{6}Li. The atomic continuum is in a electronic spin triplet channel, whose energy is lowered upon an increase of the magnetic field strength B. The bare molecule is in a electronic spin singlet channel and its bare energy is therefore not altered by the magnetic field. Due to interaction with the atomic continuum the bare molecule becomes dressed. When the dressed molecular energy reaches the atomic continuum the resonance takes place. In this section, we actually rotate the picture, namely the threshold of the atomic continuum stays at zero energy, while δ_B depends linearly on B.

with $\hat{G}_a^{-1}(E) = E - \hat{H}_0 - \hat{V}_{bg}$. Assuming that we have been able to exactly solve the atomic part of the scattering problem, namely $(\hat{H}_0 + \hat{V}_{bg})|\psi_{\mathbf{k}}^{(+)}\rangle = 2\epsilon_{\mathbf{k}}|\psi_{\mathbf{k}}^{(+)}\rangle$, we insert a completeness relation of the exact scattering states in the open channel $|\psi_{\mathbf{k}}^{(+)}\rangle$, which gives

$$E - \delta_B = \int \frac{d\mathbf{k}}{(2\pi)^3} \frac{|\langle\psi_m|\hat{V}_{am}|\psi_{\mathbf{k}}^{(+)}\rangle|^2}{E - 2\epsilon_{\mathbf{k}}} \equiv \hbar\Sigma(E), \tag{2.15}$$

where we have interpreted the expression containing the integral in Eq. (2.15) as the molecular selfenergy $\hbar\Sigma(E)$. Note that for simplicity we have ignored the possibility of bound states in the atomic background potential. If they are important, then they can be easily taken into account along the lines of Ref. [79]. We thus see that the exact equation for the molecular bound state energy has the intuitive form $E = \delta_B + \hbar\Sigma(E)$. As we see soon, the resonance takes place when the energy E of the dressed molecule reaches the threshold of the atomic continuum, i.e. when $E = 0$ and $\delta_B = -\hbar\Sigma(0)$. Therefore, we define the (experimental) detuning as $\delta \equiv \delta_B + \hbar\Sigma(0)$, such that we find for the energy equation $E = \delta + \hbar\Sigma'(E)$ with $\hbar\Sigma'(E) \equiv \hbar\Sigma(E) - \hbar\Sigma(0)$. Since the resonance now takes place for $\delta = 0$, we indeed have that $\delta = \Delta\mu(B - B_0)$.

To make further progress with Eq. (2.15) we realize that the matrix element behaves for low momenta as [57]

$$\langle\psi_m|\hat{V}_{am}|\psi_{\mathbf{k}}^{(+)}\rangle = \langle\psi_m|\hat{V}_{am}\hat{V}_{bg}^{-1}\hat{T}_{bg}^{2B}|\mathbf{k}\rangle = \frac{g}{1 + ika_{bg}}, \tag{2.16}$$

where a_{bg} is the s-wave scattering length of the background interaction and g is by

definition the coupling strength at zero momentum. In the limit of vanishing background interaction, the above equation reduces to $\langle\psi_{\rm m}|\hat{V}_{\rm am}|\mathbf{k}\rangle = g$, which means we have used a momentum-independent or local atom-molecule coupling. This approximation is appropriate, because the spatial extent of the molecular wavefunction and the atom-molecule coupling is very small compared to the de Broglie wavelength of the scattering atoms. Using for the same reason also a local or momentum-independent background interaction $\hat{V}_{\rm bg}$, then the momentum dependence in Eq. (2.16) is thus caused by the low-momentum behavior of the background transition matrix, which according to Eqs. (2.7), (2.8) and (2.9) is proportional to $(1 + ika_{\rm bg})^{-1}$.

Using Eqs. (2.15) and (2.16), we obtain that

$$\begin{aligned}\hbar\Sigma'(E) &\equiv \hbar\Sigma(E) - \hbar\Sigma(0) = \int \frac{d\mathbf{k}}{(2\pi)^3}\frac{g^2}{1+k^2a_{\rm bg}^2}\left(\frac{1}{E-2\epsilon_{\mathbf{k}}}+\frac{1}{2\epsilon_{\mathbf{k}}}\right)\\ &= \frac{\eta\sqrt{-E}}{1-a_{\rm bg}\sqrt{-mE}/\hbar}\end{aligned} \tag{2.17}$$

with $\eta = g^2m^{3/2}/4\pi\hbar^3$ and where we have assumed a negative background scattering length, which is indeed the case for ^{6}Li. The bound-state equation is now an analytically solvable cubic equation, although its solution is somewhat cumbersome [78]. A simpler result is obtained when we ignore $a_{\rm bg}$, which is allowed close to resonance, where E goes to zero. Then, we find

$$E = \delta + \frac{\eta^2}{2}\left(\sqrt{1-\frac{4\delta}{\eta^2}}-1\right), \tag{2.18}$$

such that for $\delta \to 0$ we have $E = -\delta^2/\eta^2$. This implies that the bound-state energy of the dressed molecule goes to zero quadratically with the applied magnetic-field strength B, although the bare molecular energy varies linearly with B. Moreover, from Eq. (2.13) it follows that the dressed molecular state is given by $|\psi_{\rm dr}\rangle = \sqrt{Z}|\psi_{\rm m}\rangle + \sqrt{1-Z}|\psi_{\rm aa}\rangle$, where

$$\frac{1-Z}{Z} = \langle\psi_{\rm m}|\hat{V}_{\rm am}\hat{G}_{\rm a}(E)^2\hat{V}_{\rm am}|\psi_{\rm m}\rangle = -\frac{\partial\hbar\Sigma(E)}{\partial E} = -\frac{\partial\hbar\Sigma'(E)}{\partial E}. \tag{2.19}$$

Eqs. (2.17) and (2.19) then allow us to calculate $Z(E)$, i.e. the amplitude of the dressed molecular state in the closed channel, where for the energy E we must substitute the solution to the bound-state equation.

2.2.2 Resonant atomic interaction

Having solved for all molecular properties, we now examine the effect of the Feshbach resonance on the atomic physics in the open channel. Solving Eq. (2.13) for the atomic channel, we find that

$$\left\{\hat{H}_0 + \hat{V}_{\rm bg} + \hat{V}_{\rm m}\right\}|\psi_{\rm aa}\rangle = E|\psi_{\rm aa}\rangle, \tag{2.20}$$

where $\hat{V}_{\rm m}$ is the molecule-mediated interaction given by

$$\hat{V}_{\rm m} = \frac{\hat{V}_{\rm am}|\psi_{\rm m}\rangle\langle\psi_{\rm m}|\hat{V}_{\rm am}}{E-\delta_{\rm B}}, \tag{2.21}$$

and we also used that in our model $|\psi_{\rm m}\rangle\langle\psi_{\rm m}|$ is the unity matrix in the closed channel. As a result, the total interaction in the open channel is given by $\hat{V} = \hat{V}_{\rm bg} + \hat{V}_{\rm m}$. From Eq. (2.5), we have that the exact transition matrix in the open channel is given by

$$\begin{aligned} \hat{T}^{\rm 2B} &= \hat{V} + \hat{V}\hat{G}\hat{V} \\ &= \hat{T}^{\rm 2B}_{\rm bg} + \hat{T}^{\rm 2B}_{\rm bg}\hat{V}^{-1}_{\rm bg}\hat{V}_{\rm m}(1-\hat{G}_{\rm a}\hat{V}_{\rm m})^{-1}\hat{V}^{-1}_{\rm bg}\hat{T}^{\rm 2B}_{\rm bg} \equiv \hat{T}^{\rm 2B}_{\rm bg} + \hat{T}^{\rm 2B}_{\rm res} \end{aligned} \tag{2.22}$$

with $\hat{G}^{-1}(E) = E - \hat{H}_0 - \hat{V}_{\rm bg} - \hat{V}_{\rm m}$. The exact two-body T matrix is thus seen to consist of a purely background part $\hat{T}^{\rm 2B}_{\rm bg}$ and a resonant part $\hat{T}^{\rm 2B}_{\rm res}$. The first is given by $\hat{T}^{\rm 2B}_{\rm bg} = \hat{V}_{\rm bg} + \hat{V}_{\rm bg}\hat{G}_{\rm a}\hat{V}_{\rm bg}$, which, as before, leads for s-wave scattering at zero momentum to $T^{\rm 2B}_{\rm bg}(0) = 4\pi\hbar^2 a_{\rm bg}/m$.

The momentum dependence of the resonant part may be further evaluated by

$$\langle\mathbf{k}'|\hat{T}^{\rm 2B}_{\rm res}(2\epsilon_{\mathbf{k}})|\mathbf{k}\rangle = \frac{\langle\mathbf{k}'|\hat{T}^{\rm 2B}_{\rm bg}\hat{V}^{-1}_{\rm bg}\hat{V}_{\rm am}|\psi_{\rm m}\rangle\langle\psi_{\rm m}|\hat{V}_{\rm am}\hat{V}^{-1}_{\rm bg}\hat{T}^{\rm 2B}_{\rm bg}|\mathbf{k}\rangle}{2\epsilon_{\mathbf{k}} - \delta_{\rm B} - \hbar\Sigma(2\epsilon_{\mathbf{k}})}, \tag{2.23}$$

so that together with Eq. (2.16) we find that at zero momentum and energy $T^{\rm 2B}_{\rm res}(0) = -g^2/(\hbar\Sigma(0)+\delta_{\rm B}) = -g^2/\delta$. This indeed shows that for $\delta = 0$ the transition matrix in the open channel goes to infinity at zero energy, implying a diverging scattering length. We thus have that

$$T^{\rm 2B}(0) = \frac{4\pi\hbar^2 a}{m} = \frac{4\pi\hbar^2 a_{\rm bg}}{m} - \frac{g^2}{\delta} = \frac{4\pi\hbar^2 a_{\rm bg}}{m}\left(1 - \frac{\Delta B}{B-B_0}\right), \tag{2.24}$$

where the width of the resonance ΔB, the location B_0 and the background scattering length are readily determined experimentally by fitting to the data. As a result, the atom-molecule coupling constant g can be expressed in terms of the experimentally known parameters as $g = \sqrt{4\pi\hbar^2 a_{\rm bg}\Delta B\Delta\mu/m}$. We note that our present expression for the coupling constant is suited for Bose or Fermi mixtures, while for fully polarized bosonic or fermionic systems it is more common to introduce the coupling constant as $g = \langle\psi_{\rm m}|\hat{V}_{\rm am}|\mathbf{k}\rangle/\sqrt{2}$. The reason is that this choice leads to the standard form of the many-body Hamiltonian [57]. As a result, the same calculations lead for fully polarized bosons to $g = \sqrt{2\pi\hbar^2 a_{\rm bg}\Delta B\Delta\mu/m}$, while fully polarized fermions do not undergo s-wave scattering. Fermions in the same internal state can interact through p-wave interactions, although this is usually a weak effect at ultralow temperatures. However, near a p-wave resonance these interactions are greatly enhanced, which is the topic of the next section.

To summarize, we have solved for the properties of the dressed molecular state near a Feshbach resonance. Moreover, we have studied what the effect of this molecular state

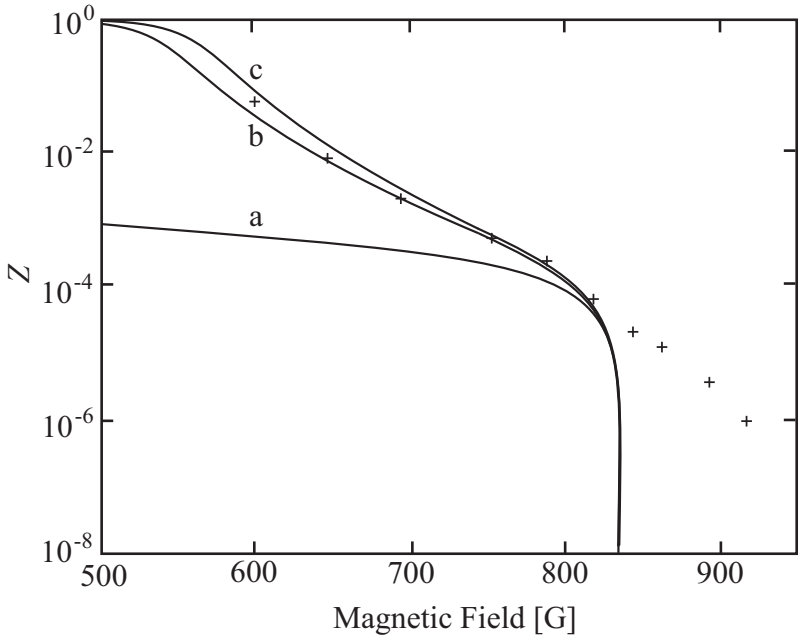

Figure 2.5: Wavefunction renormalization factor Z as a function of magnetic field strength, as adapted from Ref. [79]. Curve (a) is calculated without background interactions, curve (b) with a constant background scattering length $a_{\rm bg}$ and (c) with a magnetic-field dependent $a_{\rm bg}$ as determined in Ref. [80]. The experimental data is from Ref. [18]. At resonance, Z goes to zero, while for positive detuning, the molecule is not stable in the two-body case. To get agreement with the experimental data also for positive detuning, a many-body calculation is needed [81].

is on the transition matrix in the open channel. In particular, we have seen when the resonant part of the transition matrix diverges and gives rise to an infinite scattering length. Since the location of the resonance, its width, and the background scattering length are easily determined by fitting to the experimental data, we have access to all relevant parameters for a quantitative study of the molecular selfenergy from Eq. (2.17) and the wavefunction renormalization factor from Eq. (2.19). The results for Z are shown in Fig. 2.5 for the broad resonance of ^{6}Li near $B_0 = 834$ G, as determined in Ref. [79]. It shows that the amplitude of the dressed molecule in the closed channel is very small over a very wide range near resonance. As a result, all the action happens in the open channel, where, apart from allowing the resonance to actually take place, the bare molecular state hardly plays any role. This observation then leads to the so-called single-channel model of a Feshbach resonance, where only the atomic channel is taken into account with the transition matrix given by Eq. (2.24). The single-channel model is valid for wide resonances, where Z is small. As we see next, it is less applicable to p-wave resonances, which are typically narrow, so that Z is large.

2.3 Theory for p-wave Feshbach molecules

The two-body problem near a p-wave Feshbach resonance can be treated along the same lines as the corresponding problem for the s-wave resonance.[1] We consider two fermionic particles that are in the same hyperfine spin state and that interact with each other through a coupling with a closed molecular channel and through a p-wave background interaction in the open channel, both with angular momentum projection m_ℓ. As in the s-wave case [57], the scattering due to the background interaction gives rise to a dressed atom-molecule coupling, given by

$$g_{m_\ell}(\mathbf{k}) = \frac{1}{\sqrt{2}}\langle\psi_{\rm m}|\hat{V}_{\rm am}|\psi^{(+)}_{\mathbf{k}}\rangle = \frac{g_{m_\ell}k_{m_\ell}}{1+i(ka^{\rm bg}_{m_\ell})^3}, \tag{2.25}$$

where $|\psi^{(+)}_{\mathbf{k}}\rangle$ is the scattering state with momentum $\mathbf{k}$ in the open channel and $\hat{V}_{\rm am}$ is the coupling potential between the open and closed channels. The notation m_ℓ refers to the projection of the angular momentum $m_\ell = 0, \pm 1$, such that $k_0 = k_z$ and $k_{\pm 1} = \mp(k_x \pm ik_y)/\sqrt{2}$, while the coupling constant g_{m_ℓ} characterizes the strength of atom-molecule interactions. The p-wave background scattering length $a^{\rm bg}_{m_\ell}$ comes from the background transition matrix with projection m_ℓ in the open channel. In the case of background p-wave scattering from a hard-core potential, we have that the above introduced scattering length $a^{\rm bg}_{m_\ell}$ is directly related to the hard-core radius $a_{\rm hc}$ of the background potential through $a^{\rm bg}_{m_\ell} = a_{\rm hc}/3^{1/3}$.

With the dressed atom-molecule coupling from Eq. (2.25), we can calculate the two-body molecular selfenergy analytically, analogous to the s-wave case of Eq. (2.17), so that

$$\begin{aligned}\hbar\Sigma'_{m_\ell}(z) &= \hbar\Sigma_{m_\ell}(z) - \hbar\Sigma_{m_\ell}(0) = \frac{2}{\mathcal{V}}\sum_{\mathbf{k}}|g_{m_\ell}(\mathbf{k})|^2\left(\frac{1}{z-2\epsilon_{\mathbf{k}}}+\frac{1}{2\epsilon_{\mathbf{k}}}\right)\\ &= \frac{mg^2_{m_\ell}}{18\pi\hbar^2|a^{\rm bg}_{m_\ell}|^3}\frac{-\zeta(2+\sqrt{-\zeta})}{1+2\sqrt{-\zeta}-\zeta(2+\sqrt{-\zeta})},\end{aligned} \tag{2.26}$$

where $\epsilon_{\mathbf{k}} = \hbar^2k^2/2m$ is the kinetic energy. The dimensionless energy ζ is given by $\zeta = m{a^{\rm bg}_{m_\ell}}^2 z/\hbar^2$. To obtain this result we have renormalized the selfenergy $\hbar\Sigma_{m_\ell}(z)$ by subtracting $\hbar\Sigma_{m_\ell}(0)$. As in the s-wave case, this is convenient because in the equation for the bound state energy of the dressed molecule, namely $E - \delta^{\rm B}_{m_\ell} = \hbar\Sigma_{m_\ell}(E)$, we can subtract $\hbar\Sigma_{m_\ell}(0)$ on both sides, which also renormalizes the bare detuning $\delta^{\rm B}_{m_\ell}$ to the renormalized or experimental detuning δ_{m_ℓ}, and leads to $E - \delta_{m_\ell} = \hbar\Sigma'_{m_\ell}(E)$. The two-body resonance now indeed occurs when the bound-state energy reaches the atomic continuum, i.e. at $E = 0$ and $\delta_{m_\ell} = 0$. Therefore, the renormalized detuning is the experimentally relevant quantity and given by $\delta_{m_\ell} = \Delta\mu(B - B_{m_\ell})$, with B the applied magnetic field and B_{m_ℓ} the location of the Feshbach resonance. Note that in

[1] This section is directly based on K. B. Gubbels and H. T. C. Stoof, *Theory for p-Wave Feshbach Molecules*, Phys. Rev. Lett. **99**, 190406 (2007).

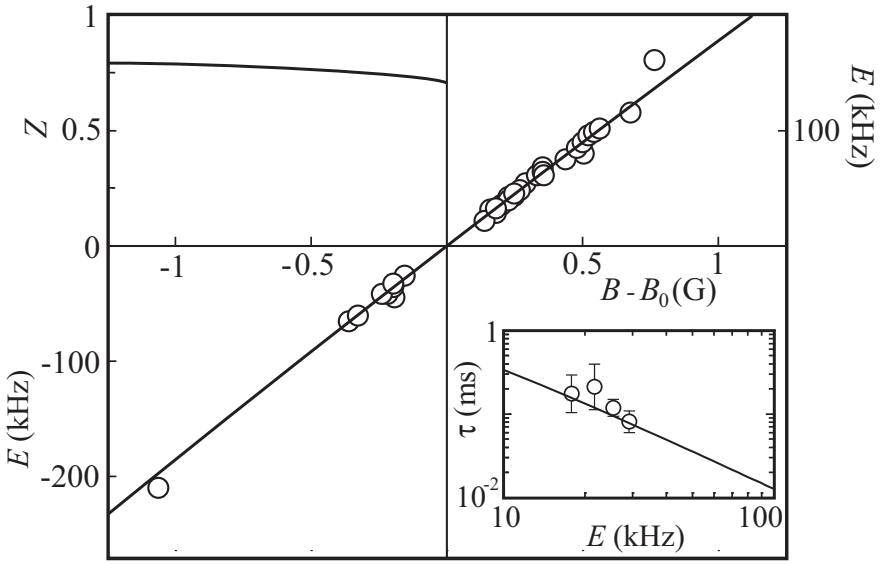

Figure 2.6: Two-body physics near the $m_\ell = 0$ p-wave resonance of ^{40}K located at $B_0 = 198$ G. The upper left panel shows the probability Z to be in the closed Feshbach channel as a function of the magnetic field B. In the lower left and the upper right panel the black line shows the binding energy E as a function of magnetic field. For positive detuning the molecules are not stable, resulting in a finite lifetime τ, shown in the lower right panel. The open circles are data from the experiments of Gaebler *et al.* [46].

general the Feshbach resonances with different values of m_ℓ need not be located at the same magnetic-field strength. In Ref. [82], it was shown how magnetic dipole-dipole interactions between the valence electrons of alkali atoms can lead to an energy shift between Feshbach molecular states that depends on the angular momentum projection m_ℓ. Also note that by using the dressed atom-molecule coupling, the right-hand side of Eq. (2.26) is finite, so no arbitrary, undetermined cutoff needs to be introduced. For small energy we obtain that

$$\hbar\Sigma'_{m_\ell}(z) \simeq \frac{m g_{m_\ell}^2}{\hbar^2}\left\{\frac{-mz}{9\pi\hbar^2|a_{m_\ell}^{\rm bg}|} - \frac{(-mz/\hbar^2)^{3/2}}{6\pi}\right\}. \tag{2.27}$$

The 'universal' coefficient of $(-mz/\hbar^2)^{3/2}$ is in agreement with Refs. [49, 83].

The binding energy of p-wave Feshbach molecules in a gas of spin-polarized ^{40}K atoms near the $m_\ell = 0$ Feshbach resonance at 198 G has been accurately measured as a function of magnetic field by Gaebler *et al.* [46], where they find an almost perfectly linear behavior. From the slope, which is given by $Z\Delta\mu$, we obtain $\Delta\mu = 0.175\mu_{\rm B}$ with $\mu_{\rm B}$ the Bohr magneton. However, for small detuning they report tiny deviations in this linear behavior. In Fig. 2.6 we have calculated the binding energy with the use of Eq. (2.26), where we extract the relevant Feshbach parameters $a_0^{\rm bg}$ and g_0 from the collisional phase shift of the considered p-wave resonance obtained in Ref. [82]. This

results in $a_0^{\rm bg} = 98a_0$ and $g_0 = 33a_0^{1/2}\hbar^2/m$, with a_0 the Bohr radius. We see that the agreement with our two-body calculation is excellent. The nonlinearities arise from the slight variation of Z with magnetic field.

Having obtained the selfenergy and the equation for the binding energy of the molecules, we can also determine the two-body wavefunction renormalization factor Z, given by $Z = [1 - \partial\hbar\Sigma'_{m_\ell}(E)/\partial E]^{-1}$ with E the solution of the equation for the binding energy. The behavior of Z as a function of magnetic field is shown in Fig. 2.6. We observe that for the considered p-wave resonance Z is very large at unitarity, namely $Z \simeq 0.7$, which shows the two-channel nature of the p-wave molecules near this resonance. Since the difference in magnetic moment between a dressed molecule and two atoms is $Z\Delta\mu$, we see that this difference does not go to zero at a p-wave resonance. As a result, the binding energy of the dressed molecule vanishes only as $(B - B_{m_\ell})$ and not as $(B - B_{m_\ell})^2$, where the latter is the previously seen behavior in the s-wave case [83, 84].

In the two-body case, there are only stable molecules for negative detuning and strictly speaking Z ceases to have meaning for positive detuning. In the many-body case the Feshbach molecules are also stable at the BCS side, due to the presence of a Fermi sea, preventing decay into the atomic continuum [79]. It is then possible to determine Z at the BCS side using many-body techniques, which has been done for the s-wave case both theoretically [79] and experimentally [18]. In the two-body case the p-wave molecules are not stabilized by a Fermi sea and the decay rate Γ is readily calculated from the selfenergy by $\Gamma = -2\mathrm{Im}[\Sigma'_{m_\ell}(E + i0)]$. The lifetime is thus $\tau = 1/\Gamma$. The calculated lifetimes are shown in Fig. 2.6, leading to good agreement with the experimentally observed lifetimes without any adjustable parameters. We have thus determined all two-body properties near a p-wave Feshbach resonance exactly and found good agreement with experiments. Of particular interest is the two-channel nature of the p-wave resonance characterized by the large value of Z. This allows for the observation of interesting aspects of two-channel many-body physics, of which we discuss an example in Chapter 6.

2.4 Two atoms near resonance in a harmonic trap

So far, we have discussed the Feshbach problem for homogeneous systems, although experiments are usually performed in a harmonic trap. In the next chapter, we find that trap effects in many-body systems can most easily be taken into account when the trapping frequency gives rise to a small energy scale compared to other relevant energy scales in the system. Then, the so-called local-density approximation (LDA) applies, which considers the many-body system to be locally homogeneous in the trap with a spatially varying chemical potential. However, the conditions for LDA are not always satisfied by experiments and therefore the approximation may break down. Moreover, many experiments are nowadays done in optical lattices, where on each lattice site the trapping potential can be approximated as being harmonic. In an optical lattice, the

on-site trapping frequency ω is large and thus it does not provide a small energy scale. For these situations, it is important to also have an exact solution of the two-body Feshbach problem in a harmonic trap. In particular, we again show how background scattering processes can be taken into account, which is important for experiments with ^{6}Li that has a very large s-wave background scattering length.

Consider the s-wave Feshbach problem for two atoms in a harmonic trap. In particular, we have two fermionic ^{6}Li atoms in mind that occupy the two lowest hyperfine states of their ground state.[2] The atoms interact with each other through the central potential $\hat{V}_{\rm bg}$, while the atom-molecule coupling is given by $\hat{V}_{\rm am}$. The resulting problem is separated into a center-of-mass part and a relative part. The center-of-mass part now results in the noninteracting harmonic-oscillator problem [56], whose solution is known. The relative Schrödinger equation for the two-channel Feshbach problem in the trap is given by Eq. (2.13), where the relative noninteracting Hamiltonian $\hat{H}_0$ is now given by

$$\hat{H}_0 = -\frac{\hbar^2\nabla_{\mathbf{r}}^2}{m} + \frac{1}{4}m\omega^2\mathbf{r}^2. \tag{2.28}$$

We assume that the energy $\delta_{\rm B}$ of the bare molecular state $|\psi_{\rm m}\rangle$ is not affected by the presence of the harmonic trap. This is well justified in practice, since the spatial extent of the bare molecular wavefunction, centered around $\mathbf{r} = 0$, is very small compared the the harmonic oscillator length $l_{\rm a} \equiv \sqrt{\hbar/m\omega}$. Furthermore, we can rewrite Eq. (2.13) to obtain as before

$$\langle\psi_{\rm m}|\hat{V}_{\rm am}\frac{1}{E - \hat{H}_0 - \hat{V}_{\rm bg}}\hat{V}_{\rm am}|\psi_{\rm m}\rangle = E - \delta_{\rm B}. \tag{2.29}$$

2.4.1 No background atom-atom scattering

For many atoms of interest, such as for example rubidium or potassium, we have that the background interaction is small such that in first instance it may be neglected. The resulting problem was solved in Ref. [85] and here we highlight the most important results. The eigenfunctions of $\hat{H}_0$ can be written in terms of the generalized Laguerre polynomials

$$\phi_n^{\rm aa}(r) = \langle\mathbf{r}|\phi_n^{\rm aa}\rangle = \frac{e^{-r^2/4l_{\rm a}^2}L_n^{1/2}(r^2/2l_{\rm a}^2)}{(2\pi l_{\rm a}^2)^{3/4}\sqrt{L_n^{1/2}(0)}}, \tag{2.30}$$

which correspond to the eigenenergies

$$E_n = (2n + 3/2)\hbar\omega, \tag{2.31}$$

for $n = 0, 1, 2, ...$ Note that only states with zero angular momentum are considered, because we wish to describe a two-channel s-wave scattering process. Using the completeness relation of the eigenfunctions $|\phi_n^{\rm aa}\rangle$ in the open channel, Eq. (2.29) can be

[2] This section is directly based on K. B. Gubbels, D. B. M. Dickerscheid, and H. T. C. Stoof, *Dressed Molecules in an Optical Lattice*, New J. Phys. **8**, 151 (2006).

rewritten as

$$\sum_n \frac{|\langle\psi_{\rm m}|\hat{V}_{\rm am}|\phi_n^{\rm aa}\rangle|^2}{E-E_n} = E - \delta_{\rm B}. \tag{2.32}$$

Invoking the pseudopotential approxiation for fermions, which means that $\langle\mathbf{r}|\hat{V}_{\rm am}|\psi_{\rm m}\rangle = g\delta(\mathbf{r})$, yields

$$\begin{aligned} E - \delta_{\rm B} &= g^2 \sum_n \frac{\phi_n^{\rm aa*}(0)\phi_n^{\rm aa}(0)}{E-E_n} \\ &= g^2 \left[\frac{\Upsilon(E)}{2\sqrt{2}\pi l_{\rm a}^3 \hbar\omega} - \lim_{r\to 0} \frac{m}{4\pi\hbar^2 r} \right], \end{aligned} \tag{2.33}$$

where the function $\Upsilon(E)$ is given by

$$\Upsilon(E) \equiv \frac{\Gamma(-E/2\hbar\omega + 3/4)}{\Gamma(-E/2\hbar\omega + 1/4)} \tag{2.34}$$

with $\Gamma(x)$ the gamma function. The energy-independent divergence in Eq. (2.33) is an ultraviolet divergence resulting from the use of pseudopotentials, and was first obtained by Busch *et al.* in the context of a single-channel problem [56]. It can be dealt with using the following renormalization procedure. We define the renormalized detuning δ as

$$\delta \equiv \delta_{\rm B} - \lim_{r\to 0} \frac{mg^2}{4\pi\hbar^2 r}, \tag{2.35}$$

which has two major advantages. Not only do we absorb the ultraviolet divergence in the definition of δ, but this renormalized detuning also has direct experimental relevance, in contrast to $\delta_{\rm B}$.

Namely, as before δ corresponds to the detuning from the magnetic field B_0, at which the Feshbach resonance takes place in the absence of the harmonic trap. This can be understood from the treatment of the homogeneous Feshbach problem without trapping potential and background interaction [57]. The ultraviolet divergence of Eq. (2.33) is seen to be exactly the same divergence that we would have for $\hbar\Sigma(0)$ in Eq. (2.17) when we would take $a_{\rm bg}$ to be zero. Moreover, in the absence of the trap we have that the condition for the location of the Feshbach resonance is given by the dressed molecular energy becoming equal to the threshold of the atomic continuum, i.e. $E = 0$. This leads to the resonance condition

$$\delta_{\rm B} = -\hbar\Sigma(0) = \lim_{r\to 0} \frac{mg^2}{4\pi\hbar^2 r}. \tag{2.36}$$

As a result, the definition in Eq. (2.35) places the resonance in the absence of the harmonic trap conveniently at $\delta = 0$ and, by construction, the (renormalized) detuning is of the form

$$\delta(B) = \Delta\mu(B - B_0), \tag{2.37}$$

where $\Delta\mu$ is the difference in magnetic moment between the atoms in the open channel and the bare molecule in the closed channel. Substituting Eq. (2.35) in Eq. (2.33) gives

$$E - \delta = \frac{g^2 \Upsilon(E)}{2\sqrt{2}\pi l_{\mathrm{a}}^3 \hbar\omega}, \tag{2.38}$$

which allows us to calculate the eigenenergies of the Feshbach problem in a trap given a certain detuning δ.

So far, we have neglected background atom-atom scattering effects. These effects are particularly important for the fermion ^{6}Li, which has a very large background atom-atom scattering length a_{bg} near the extremely broad Feshbach resonance at $B_0 = 834$ G, namely approximately $-1.4 \cdot 10^3 a_0$, where a_0 is the Bohr radius.

2.4.2 With background atom-atom interaction

The relative Schrödinger equation for two atoms in a harmonic potential interacting through the pseudopential $V_{\mathrm{bg}}(\mathbf{r}) = V_0 \delta(\mathbf{r})$ without coupling to a molecular state

$$(\hat{H}_0 + \hat{V}_{\mathrm{bg}})|\phi_\nu\rangle = E_\nu |\phi_\nu\rangle \tag{2.39}$$

can be solved analytically for s-wave scattering following a treatment along the lines of Ref. [56]. The eigenvalues of Eq. (2.39) are given by $E_\nu = (2\nu + 3/2)\hbar\omega$, which are the solutions to the equation

$$\sqrt{2}\frac{\Gamma(-E_\nu/2\hbar\omega + 3/4)}{\Gamma(-E_\nu/2\hbar\omega + 1/4)} = \frac{l_{\mathrm{a}}}{a_{\mathrm{bg}}}, \tag{2.40}$$

where ν is in general not an integer and where a_{bg} is the scattering length resulting from the interaction. The corresponding eigenfunctions $\phi_\nu^{\mathrm{aa}}(r) = \langle r|\phi_\nu^{\mathrm{aa}}\rangle$ have the following form

$$\phi_\nu^{\mathrm{aa}}(r) = A_\nu e^{-r^2/4l_{\mathrm{a}}^2} \Gamma(-\nu) U(-\nu, 3/2, r^2/2l_{\mathrm{a}}^2), \tag{2.41}$$

where A_ν is a normalization constant and $U(-\nu, 3/2, r^2/2l_{\mathrm{a}}^2)$ is a so-called confluent hypergeometric function of the second kind. We can determine A_ν analytically by applying a limiting procedure to theorem 7.622 of Ref. [86], resulting in

$$A_\nu^2 = \frac{\Gamma(-\nu - 1/2)}{4\sqrt{2}\pi^2 l_{\mathrm{a}}^3 \Gamma(-\nu)[\psi^0(-\nu) - \psi^0(-\nu - 1/2)]}, \tag{2.42}$$

in which ψ^0 denotes the digamma function. Furthermore, we can use the completeness relation of the eigenfunctions $|\phi_\nu^{\mathrm{aa}}\rangle$ to rewrite Eq. (2.29), which yields

$$\sum_\nu \frac{|\langle\psi_{\mathrm{m}}|\hat{V}_{\mathrm{am}}|\phi_\nu^{\mathrm{aa}}\rangle|^2}{E - E_\nu} = E - \delta_{\mathrm{B}}. \tag{2.43}$$

In order to proceed from Eq. (2.43), we realize that the spatial integral in the matrix element $\langle\psi_{\rm m}|\hat{V}_{\rm am}|\phi_\nu^{\rm aa}\rangle$ only acquires a sizeable contribution from a very small region around $\mathbf{r}=0$, because the spatial extent of the molecular wavefunction $\psi_{\rm m}$ and the atom-molecule coupling $V_{\rm am}$ is very small. This means that we are only interested in $\phi_\nu^{\rm aa}(r)$ for small values of r, giving

$$\begin{aligned}\phi_\nu^{\rm aa}(r) &= -\sqrt{\pi}A_\nu\left(\frac{2\Gamma(-\nu)}{\Gamma(-\nu-1/2)}-\sqrt{2}\frac{l_{\rm a}}{r}+\mathcal{O}\left(\frac{r}{l_{\rm a}}\right)\right)\\ &= -\sqrt{2\pi}l_{\rm a}A_\nu\left(\frac{1}{a_{\rm bg}}-\frac{1}{r}+\mathcal{O}\left(\frac{r}{l_{\rm a}^2}\right)\right),\end{aligned} \tag{2.44}$$

where in the second line we used Eq. (2.40). The eigenfunctions $\phi_\nu^{\rm aa}(r)$ behave the same for small r as the s-wave scattering states in the absence of a harmonic trap $\psi_{\mathbf{k}}^{(+)}(r)$, which we encountered earlier this chapter. To show this, we use the following form of the s-wave scattering states [76]

$$\psi_{\mathbf{k}}^{(+)}(r)=\frac{\sin\left[kr+\delta_0(k)\right]}{kr}, \tag{2.45}$$

where k is the relative momentum of the scattering state and $\delta_0(k)$ is the s-wave phase shift, which are determined by the following relations

$$k = \sqrt{\frac{mE_\nu}{\hbar^2}}, \tag{2.46}$$

$$\delta_0(k) = \tan^{-1}(-ka_{\rm bg}). \tag{2.47}$$

Indeed, for small r, we have

$$\begin{aligned}\psi_{\mathbf{k}}^{(+)}(r) &= \cos\delta_0(k)+\frac{\sin\delta_0(k)}{kr}+\mathcal{O}(kr)\\ &= -\frac{\sin\delta_0(k)}{k}\left(\frac{1}{a_{\rm bg}}-\frac{1}{r}+\mathcal{O}(k^2r)\right),\end{aligned} \tag{2.48}$$

where in the second line we used Eq. (2.47). As a result, for small r

$$\phi_\nu^{\rm aa}(r)=\sqrt{2\pi}\frac{kl_{\rm a}A_\nu}{\sin\delta_0(k)}\psi_{\mathbf{k}}^{(+)}(r). \tag{2.49}$$

This relation is illustrated by Fig. 2.7, where $\phi_\nu^{\rm aa}$, $\psi'_{\mathbf{k}}\equiv\sqrt{2\pi}kl_{\rm a}A_\nu\psi_{\mathbf{k}}^{(+)}/\sin\delta_0$ and their difference are plotted as a function of r. We see that the difference indeed vanishes for small r and increases with increasing r. The scattering states $\psi_{\mathbf{k}}^{(+)}(r)$ are the solutions of the relative two-atom s-wave scattering problem without optical lattice and without atom-molecule coupling [57]. The physical reason for the similarity between $\phi_\nu(r)$ and $\psi_{\mathbf{k}}^{(+)}(r)$ near $r=0$ is due to the following: for small r compared to $l_{\rm a}$, the atoms experience an effectively constant harmonic potential by which they are not affected.

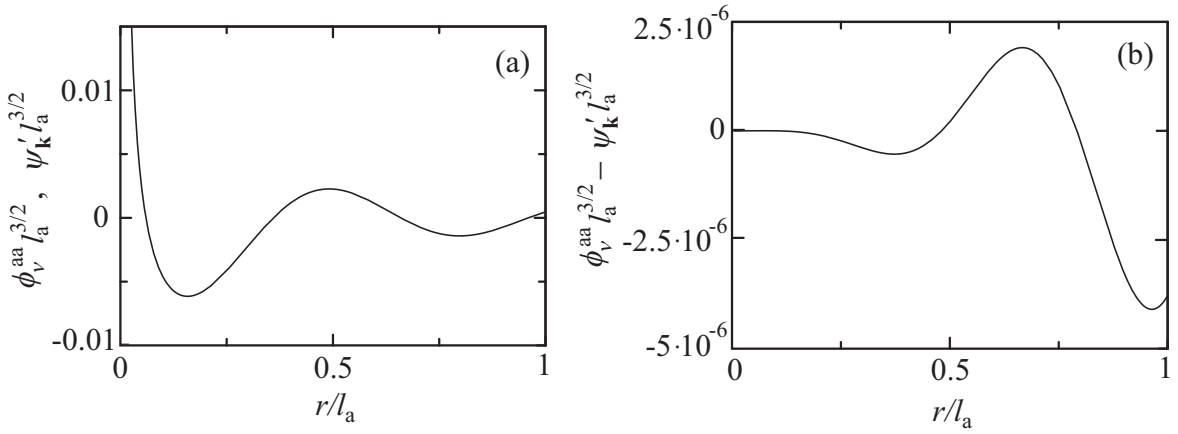

Figure 2.7: (a) Plot of the wavefunctions ϕ_ν^{aa} and $\psi'_{\mathbf{k}}$ as a function of the interatomic distance r. On the scale of the figure, the two wavefunctions cannot be distuinguished. (b) Plot of the difference between the wavefunctions ϕ_ν^{aa} and $\psi'_{\mathbf{k}}$ as a function of the interatomic distance r. Note that this difference is extremely small compared to the value of the wavefunctions themselves. All quantities on the axes are made dimensionless using the atomic harmonic oscillator length l_{a}.

.

Therefore, for small r the wavefunction from the theory with optical lattice should, up to a normalization, reduce to the wavefunction from the theory without optical lattice. Since we have seen in Section 2.2 how to solve the homogeneous Feshbach problem without an optical lattice [57], we are able to profit from this knowledge. This is what we do in the next paragraph.

2.4.3 Solving the two-atom Feshbach problem

By combining Eqs. (2.43) and (2.49), we obtain

$$\sum_\nu \frac{2\pi k^2 l_{\mathrm{a}}^2 A_\nu^2}{\sin^2\delta_0(k)} \frac{|\langle\psi_{\mathrm{m}}|V_{\mathrm{am}}|\psi_{\mathbf{k}}^{(+)}\rangle|^2}{E-E_\nu} = E - \delta_{\mathrm{B}}. \tag{2.50}$$

From Eq. (2.16), we have that [57]

$$\langle\psi_{\mathrm{m}}|\hat{V}_{\mathrm{am}}|\psi_{\mathbf{k}}^{(+)}\rangle = \frac{g}{1+ia_{\mathrm{bg}}k}. \tag{2.51}$$

Substituting Eqs. (2.42) and (2.51) into Eq. (2.50) and rewriting the result with the use of Eq. (2.47) yields

$$\frac{g^2}{2\pi a_{\mathrm{bg}} l_{\mathrm{a}}^2} \sum_\nu \frac{1}{[E-(2\nu+3/2)]\left[\psi^0(-\nu)-\psi^0(-\nu-1/2)\right]} = E - \delta_{\mathrm{B}}. \tag{2.52}$$

Just like in Paragraph 2.4.1, we would like to renormalize the bare detuning δ_{B} to the experimental detuning δ, where the latter gives the detuning from the magnetic

field B_0 at which the Feshbach resonance takes place in the absence of an optical lattice. In Paragraph 2.2.1 we discussed the homogeneous theory that takes $a_{\rm bg}$ into account [57], for which we have at resonance that

$$\delta_{\rm B} = -\hbar\Sigma(0) = \frac{g^2 m}{4\pi\hbar^2|a_{\rm bg}|}. \tag{2.53}$$

Defining the renormalized detuning δ as $\delta \equiv \delta_{\rm B} - g^2 m_{\rm a}/4\pi\hbar^2|a_{\rm bg}|$ places the Feshbach resonance in the absence of an optical lattice conveniently at $\delta = 0$ and brings Eq. (2.52) into its final form

$$\begin{aligned} E - \delta \;\; = \;\; & \frac{g^2}{2\pi a_{\rm bg} l_{\rm a}^2} \sum_{\nu} \frac{1}{\left[E - (2\nu + 3/2)\right]\left[\psi^0(-\nu) - \psi^0(-\nu - 1/2)\right]} \\ & + \frac{g^2 m}{4\pi\hbar^2|a_{\rm bg}|}, \end{aligned} \tag{2.54}$$

where by construction $\delta = \Delta\mu(B - B_0)$ again. As in Paragraph 2.4.1, the term on the right-hand side of equation (2.54) can be interpreted as a (renormalized) molecular selfenergy $\hbar\Sigma'(E) = \hbar\Sigma(E) - \hbar\Sigma(0)$.

For ^{6}Li, which has a very large $a_{\rm bg}$, we expect the effects of the background scattering to be of particular importance. Therefore, in the next paragraph, we study Eq. (2.54) for the specific case of ^{6}Li to see if it leads to significant differences from the results given by Eq. (2.38), which doesn't take background scattering into account.

2.4.4 Lithium

Fig. 2.8(a) shows the energy levels of two interacting ^{6}Li atoms in the hyperfine states $|1\rangle$ and $|2\rangle$ near the Feshbach resonance at 834 G in a harmonic trap. The solid lines have been obtained by numerically solving equation (2.54), where we used the known experimental values for $g(B)$ and $a_{\rm bg}(B)$ corresponding to ^{6}Li [80]. Note that for the extremely broad Feshbach resonance at 834 G these parameters depend on the magnetic field B. Furthermore, we took $l_{\rm a} = 10^{-7}$ m, corresponding to $\omega = 10^6$ s^{-1}, which is a typical value for the trapping frequency in an optical lattice. In Fig. 2.8(b) the same energy-level diagram is shown, but this time without taking the background atom-atom scattering into account. Here, the solid lines have been obtained by numerically solving Eq. (2.38), where again the experimental value of the parameter $g(B)$, corresponding to ^{6}Li, was substituted.

From Fig. 2.8, we see that for ^{6}Li near the Feshbach resonance at 834 G it is important to include background atom-atom interactions, since it leads to a significant adjustment of the corresponding two-body energy-level diagram. Upon inclusion of the background atom-atom interactions, the horizontal asymptotes are shifted to different energy values, and the avoided crossings, see also Ref. [85], become much less broad. Physically, this is a result of the fact that the large value of $a_{\rm bg}$ effectively reduces

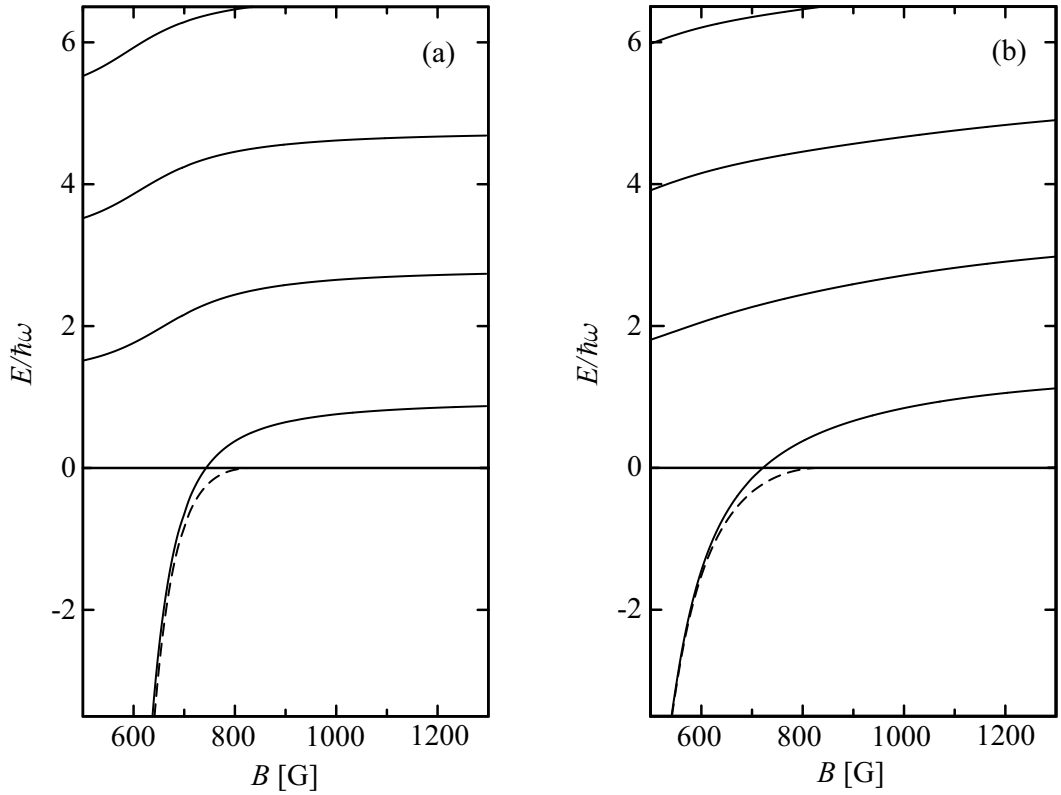

Figure 2.8: (a) Relative energy levels (solid lines) as a function of the magnetic field B for a system consisting of two ^{6}Li atoms in the hyperfine states $|1\rangle$ and $|2\rangle$ near the Feshbach resonance at 834 G in a harmonic potential of $\omega = 10^6$ s^{-1} with background atom-atom scattering taken into account. The dashed line corresponds to the binding energy of a dressed $^6Li_2$-molecule in the absence of an optical lattice. Note that as the eigenenergy of the dressed molecular ground state with optical lattice (solid line) decreases, it converges to the dressed molecular eigenenergy without optical lattice (dashed line). (b) Similar to panel (a), only this time the background atom-atom scattering is not taken into account. Note that as a result both panels differ significantly.

the atom-molecule coupling. The difference between Eqs. (2.38) and (2.54) in the case of ^{6}Li becomes even clearer when we look at the corresponding wavefunction renormalization factors Z_α given by

$$Z_\alpha = \left(1 - \left.\frac{\partial \hbar\Sigma'(E)}{\partial E}\right|_{E=\epsilon_\alpha}\right)^{-1}, \tag{2.55}$$

where $\alpha = 0$ denotes the ground state, $\alpha = 1$ the first excited state, and so on. For the calculation of Z_α we need the (renormalized) molecular selfenergy $\hbar\Sigma'$, which is given by the right-hand side of equation (2.38) for the case without background atom-atom scattering and by the right-hand side of equation (2.54) for the case with background atom-atom scattering. In Fig. 2.9, the corresponding wavefunction renormalization factors Z_α are plotted for both cases as a function of the magnetic field B. Note that

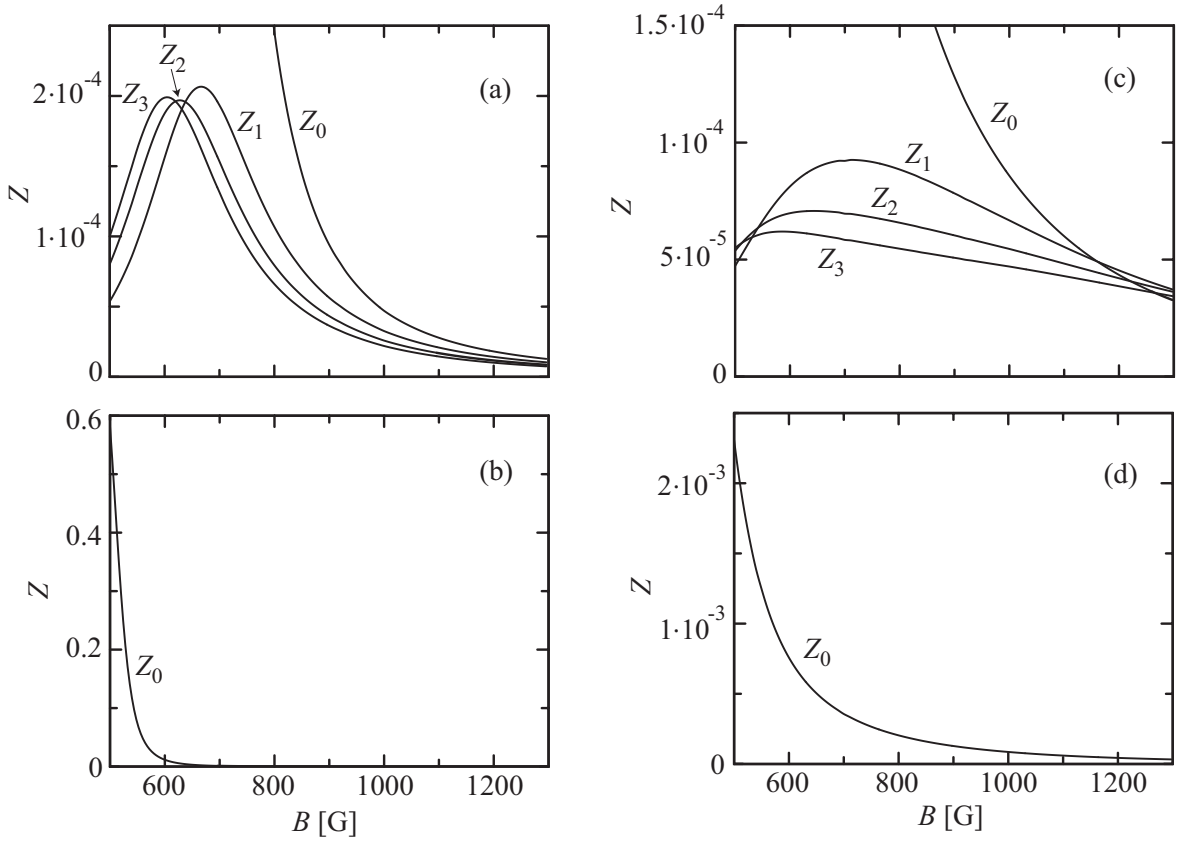

Figure 2.9: (a),(b) Wavefunction renormalization factors Z_α for ^{6}Li near the Feshbach resonance at 834 G as a function of the magnetic field B with background atom-atom scattering taken into account. Z_0 is the renormalization factor corresponding to the ground state of the two-body on-site Feshbach problem, Z_1 is the renormalization factor corresponding to the first excited state, and so on. (c),(d) Wavefunction renormalization factors Z_α for ^{6}Li as a function of the magnetic field B without background atom-atom scattering. Note that the panels on the left differ significantly from the panels on the right.

the two-body renormalization factors Z_α in Fig. 2.9(a) obtained including background interactions, are very different from the factors in Fig. 2.9(b) obtained without background interactions. Also note that these factors are directly experimentally observable as demonstrated by Partridge *et al.* [18]. We thus conclude that background atom-atom scattering plays a significant role for an atomic gas of ^{6}Li atoms in an optical lattice near the Feshbach resonance at 834 G.

In summary, we showed how to exactly solve the two-channel Feshbach problem for two atoms in a harmonic trap including background atom-atom scattering. The solution was applied to ^{6}Li near the experimentally relevant Feshbach resonance at 834 G. In particular, the two-body energy levels and the wavefunction renormalization factors Z_σ were determined. These are also important input parameters for the generalized Hubbard Hamiltonian of Ref. [85], which is used to describe the many-body physics in

an optical lattice near resonance. For a macroscopic number of particles in a shallow trap, the resulting inhomogeneous many-body problem is actually more conveniently treated using the local-density approximation, which we discuss in the next chapter.

Chapter 3

Polarized Fermi mixtures with strong interactions

We study the strongly interacting two-component Fermi mixture with a population imbalance. We start out by applying the mean-field BCS theory to calculate the homogeneous phase diagram. Although perturbative approaches are not expected to be quantitatively correct for strong interactions, mean-field theory is useful for explaining the relevant physics in the system. In order to also arrive at the phase diagram for the trapped case, we use the local-density approximation. The latter assumes that locally in the trap, the gas behaves as if it were homogeneous. From the mean-field phase diagram, we can understand the qualitative aspects of the landmark experiments exploring the imbalanced Fermi mixture, performed by Zwierlein *et al.* [24] and Partridge *et al.* [25]. Moreover, the mean-field theory leads to the additional prediction that a gapless Sarma superfluid is present at nonzero temperatures, although more measurements would be needed to unambiguously identify this prediction [60]. We also discuss intuitive ways in which the thermodynamic potential from BCS theory can be improved, such that very good agreement with Monte-Carlo calculations is realized. The combination of the improved theory with the local-density approximation ultimately leads to quantitative agreement with the experimentally obtained density profiles by Shin *et al.* [87].

3.1 Introduction

In the beginning of 2006, two experimental groups, namely the group of Ketterle at MIT and the group of Hulet at Rice University, obtained a full control over the spin imbalance or polarization P in an ultracold atomic Fermi mixture. This polarization is defined by $P = (N_+ - N_-)/(N_+ + N_-)$ with N_σ the total number of particles in the hyperfine state σ. The pioneering experiments at MIT by Zwierlein *et al.* [24] and at

Rice University by Partridge *et al.* [25] realized a strongly interacting mixture of ^{6}Li atoms in the two lowest hyperfine states of the ground state (see Fig. 2.3), where the atom number in each of the two states could be precisely tuned. These experiments immediately induced a flurry of theoretical activity [88, 89, 90, 91, 92, 93, 94, 95, 96, 97, 98, 99, 100, 101]. The interesting aspect of a polarization in the system is that not all atoms can find a partner to pair up with, because the fermions only have attractive s-wave interactions when they are in different hyperfine states. Since pairing is the mechanism behind fermionic superfluidity, the following fundamental question arises: what happens to a superfluid paired Fermi mixture upon increasing the polarization? As mentioned in Chapter 1, this is a topic of direct interest to condensed-matter, nuclear and astroparticle physics.

The ^{6}Li experiments of Zwierlein *et al.* [24, 102] and Partridge *et al.* [25] were performed in a trap to confine the atomic clouds in space. Both experiments revealed that superfluidity in an ultracold Fermi mixture with attractive interactions is in first instance maintained upon going to an imbalance in spin populations. However, on a more detailed level rather contradictory results were obtained for the behavior of the trapped mixture as a function of polarization. Namely, Zwierlein *et al.* observed a rather smooth phase transition between a phase with a superfluid core and a phase that was fully normal at a high critical polarization of about 0.7. These two phases are illustrated in Figs. 3.1(a) and (b). However, Partridge *et al.* seemed to observe a transition between two different trapped superfluid phases at a low critical polarization of about 0.1, which are illustrated in Figs. 3.1(b) and (c). Moreover, Partridge *et al.* did not observe a vanishing of the superfluid core in their experiments, where even at their highest imbalances ($P > 0.90$) the core seemed fully paired.

More experimental and theoretical studies followed in order to try to understand these differences. In a later study at MIT, Shin *et al.* showed that their trapped Fermi mixture was described by a shell structure consisting of an equal-density superfluid core, surrounded by a partially polarized normal shell and a fully polarized outer region [104]. As a function of polarization, the MIT data showed a smooth onset of the superfluid condensate in the center of the trap, which agreed with a continuous, or second-order, phase transition. Also at Rice University a further study was performed, where Partridge *et al.* observed a deformation of the superfluid core at their lowest temperatures [105]. This deformation was explained in terms of a first-order interface between the superfluid core and the normal outer region in the trap [94, 103], see also Fig. 3.1(c). Namely, a first-order interface in general gives rise to surface tension, which energetically favors a minimal area of the interface, i.e. a spherical shape. However, the trap that was used in the experiments at Rice university was actually highly elongated, so that the superfluid core was consequently deformed from the trap shape by the surface tension. At higher temperatures the deformation disappeared, although the core seemed to remain paired. The natural explanation of this behavior is that at higher temperatures the superfluid-normal transition in the trap is of second order, as in Fig. 3.1(b), so that there is no surface tension and deformation.

Since the higher-temperature results at Rice University resembled qualitatively the

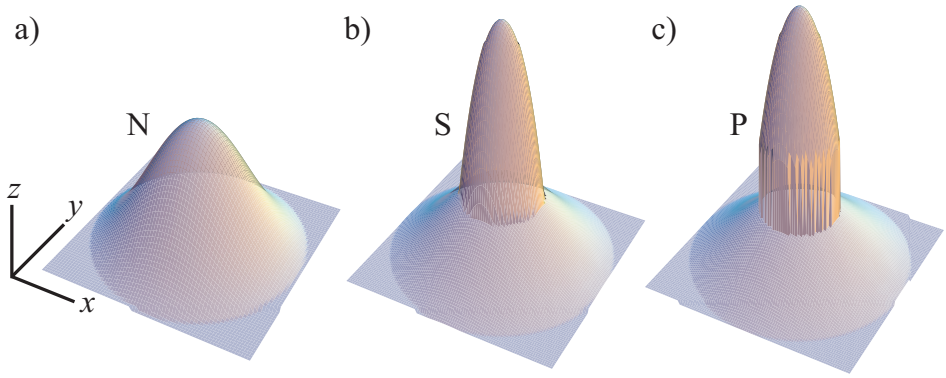

Figure 3.1: Sketch of three different phases that can be present for a strongly interacting Fermi mixture in the trap. The x and y coordinates correspond to positions in the trap, while the z coordinate represents the total density of atoms. Although there is a third spatial direction in the trap, it is not considered here, because then we would need a fourth direction for the density. a) At high temperatures, the gas is in the normal phase (N), leading to a thermal distribution of atoms in the trap. b)-c) At low temperatures, a condensate of Cooper pairs appears in the center of the trap, where the particle densities are highest. The condensate leads to a pronounced enhancement of the central densities. The superfluid core and the normal outer region in the trap can be separated by b) a continuous second-order transition (S) or c) a discontinuous first-order transition (P). In the latter case, the surface tension can deform the atomic cloud from the trap shape, if the trap shape is highly nonspherical [103].

behavior that was seen in the MIT experiments, it seemed that a difference in temperature would be the most natural way to explain both experiments in a single theoretical picture [60]. Moreover, in another experiment at MIT Shin *et al.* performed precise measurements as a function of position in the trap and temperature [87]. Because the local-density approximation applies for the MIT experiments, this actually means that Shin *et al.* were able to experimentally map out the homogeneous phase diagram of the spin-imbalanced Fermi mixture in the unitarity limit. They now observed both a second-order phase transition in the trap at higher temperatures as well as a first-order transition at their lowest temperatures. On a qualitative level, all experimental results then seem to fit in a phase diagram that is governed by a tricritical point [60, 99].

However, on the quantitative level there remain striking differences that have not been satisfactory explained so far. First of all, there is the difference in the critical imbalance P_c, at which the trapped gas becomes completely normal. Namely, Shin *et al.* find at their lowest temperatures $P_c < 0.8$ [87], while Partridge *et al.* find $P_c > 0.9$ [105]. Although the first result agrees with Monte-Carlo calculations in the local-density approximation (LDA) [106], the latter result is presently not understood. The second issue involves the normal region that surrounds the superfluid core. While the MIT experiments find that the normal state is partially polarized close to the superfluid interface, the Rice experiments only observe a fully polarized normal state. The absence

of the partially polarized region in the Rice experiment is also not understood.

The last difference is the observation of deformation by the Rice experiment, whereas the MIT experiment has not seen such deformations. The absence of a clearly observable deformation in the MIT experiment is in agreement with a recent calculation of the surface tension at nonzero temperature [107]. Although it is strongly dependent on temperature, the high value of the surface tension that is needed to explain the deformation observed at Rice University can at the moment not be microscopically accounted for. To be able to fully explain the experiments of Partridge *et al.*, it is probably necessary to explore physics beyond the local-density approximation [103, 105]. This extreme break-down of LDA could be caused by the smaller number of particles and the more extreme aspect ratio of the trap compared to the MIT experiments. Another possibility is that the Rice experiments are not at equilibrium [108]. Due to these difficulties, we compare our theoretical results in this thesis mostly with the experiments performed at MIT.

3.2 Mean-field theory

We start our theoretical discussion of the strongly interacting Fermi mixture at the mean-field level, which is useful for qualitatively explaining the relevant physics. The derivation of the thermodynamic potential density that follows from mean-field BCS theory can be found in many textbooks, see for example Ref. [30]. It yields for the population-imbalanced case at unitarity

$$\begin{aligned}\omega_{\mathrm{BCS}}[\Delta;T,\mu_\sigma] &= \frac{1}{\mathcal{V}}\sum_{\mathbf{k}}\left\{\epsilon_{\mathbf{k}}-\mu-\hbar\omega_{\mathbf{k}}+\frac{|\Delta|^2}{2\epsilon_{\mathbf{k}}}\right\}\\ &\quad -\frac{1}{\beta}\sum_{\mathbf{k},\sigma}\ln(1+e^{-\beta\hbar\omega_{\mathbf{k},\sigma}}),\end{aligned} \tag{3.1}$$

where the kinetic energy of the atoms is given by $\epsilon_{\mathbf{k}}=\hbar^2\mathbf{k}^2/2m$, m is the mass of the fermions, $\mathcal{V}$ is the volume of the mixture, T is the temperature and $\beta=1/k_{\mathrm{B}}T$. The physical meaning of the BCS order parameter Δ was explained in Section 1.2. The index $\sigma=\pm$ specifies the hyperfine state and is also called the (pseudo)spin of the fermions. There are two slight differences between Eq. (3.1) and the standard BCS expression for the thermodynamic potential [30]. First of all, the term $-|\Delta|^2/T^{2\mathrm{B}}$ is missing, where the two-body transition matrix is given by $T^{2\mathrm{B}}=4\pi\hbar^2a/m$ with a the s-wave scattering length. This is because the scattering length diverges in the unitarity limit, which is the regime where the experiments operate. Second, we allow the chemical potentials for the two hyperfine states μ_σ to be unequal, since this takes into account the population imbalance in the two spin species that is realized by the experiments. The average chemical potential μ is given by $\mu=(\mu_++\mu_-)/2$, while half the difference is denoted as $h=(\mu_+-\mu_-)/2$. In the case of nonzero h, the dispersions of the Bogoliubov quasiparticles $\hbar\omega_{\mathbf{k},\sigma}$ are spin-dependent. Namely, we

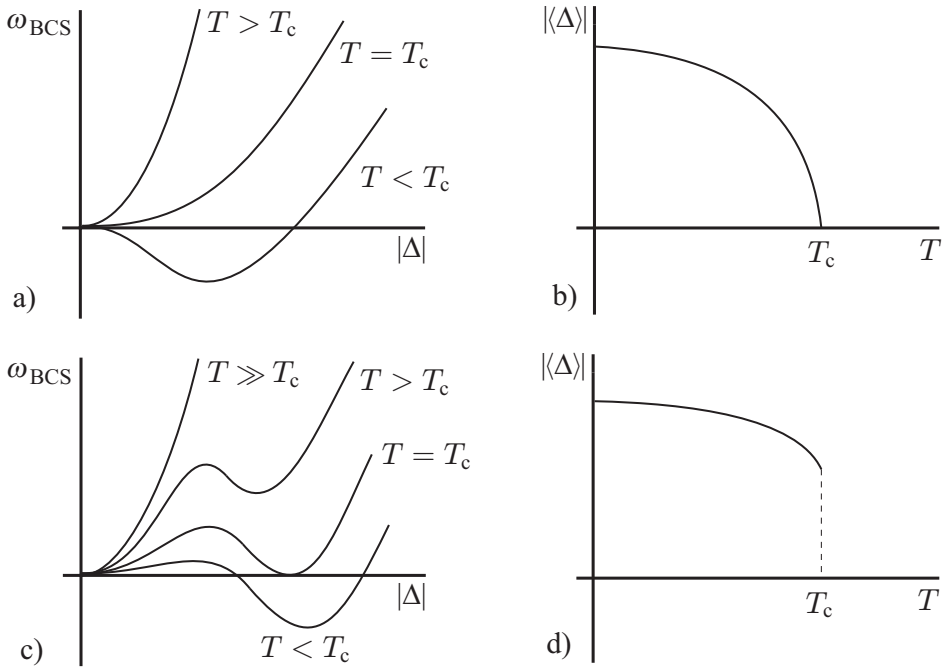

Figure 3.2: a) The behavior of the thermodynamic potential density $\omega_{\rm BCS}$ as a function of the BCS order parameter $|\Delta|$ for a second-order phase transition. For high temperatures T, the global minimum is at $|\langle\Delta\rangle| = 0$, i.e. the normal state. At the critical temperature $T_{\rm c}$ the minimum becomes a maximum. For $T < T_{\rm c}$ the system is in the superfluid state. b) Corresponding behavior of the expectation value of the order parameter $|\langle\Delta\rangle|$. At $T_{\rm c}$, $|\langle\Delta\rangle|$ goes continuously to zero. c) Same as a), but now for a first-order transition. At the critical temperature $T_{\rm c}$, the separated minima of the normal and the superfluid state have the same pressure, given by $-\omega_{\rm BCS}$, and $|\langle\Delta\rangle|$ makes a jump. This discontinuity is shown in panel d).

have that $\hbar\omega_{\mathbf{k},\sigma} = -\sigma h + \hbar\omega_{\mathbf{k}}$ with $\hbar\omega_{\mathbf{k}} = \sqrt{(\epsilon_{\mathbf{k}} - \mu)^2 + |\Delta|^2}$ [109]. This follows from the usual Bogoliubov diagonalization of the mean-field Hamiltonian. The logarithms in Eq. (3.1) describe an ideal gas of fermionic quasiparticles with dispersion $\hbar\omega_{\mathbf{k},\sigma}$, while the other terms describe the equal-density Cooper pair condensate.

To determine the atomic density n_σ in spin state σ, we use the relation $n_\sigma = -\partial\omega_{\rm BCS}[\langle\Delta\rangle; T, \mu_\sigma]/\partial\mu_\sigma$, which leads to

$$n_\sigma[\langle\Delta\rangle; T, \mu_\sigma] = \frac{1}{\mathcal{V}} \sum_{\mathbf{k}} \left\{ |u_{\mathbf{k}}|^2 f(\hbar\omega_{\mathbf{k},\sigma}) + |v_{\mathbf{k}}|^2 [1 - f(\hbar\omega_{\mathbf{k},-\sigma})] \right\} \ . \tag{3.2}$$

Here, $\langle\Delta\rangle$ denotes the global minimum of the thermodynamic potential and $f(x) = 1/(e^{\beta x} + 1)$ are the Fermi distributions. The BCS coherence factors $|u_{\mathbf{k}}|^2$ and $|v_{\mathbf{k}}|^2$ are determined by the relations $|u_{\mathbf{k}}|^2 = [1 + (\epsilon_{\mathbf{k}} - \mu)/\hbar\omega_{\mathbf{k}}]/2$ and $|u_{\mathbf{k}}|^2 + |v_{\mathbf{k}}|^2 = 1$ [2, 30, 109].

Depending on the temperature T and the chemical potentials μ_σ, the thermodynamic potential density $\omega_{\rm BCS}$ can give rise to either one, two or three extremal points.

At high temperatures there is only one extremum, namely a global minimum at $\Delta = 0$, so that the system is in the normal phase. For the well-studied balanced case, $h = 0$, BCS theory predicts that at a certain critical temperature T_c the extremum at $\Delta = 0$ becomes a local maximum. The global minimum then continuously shifts away to a nonzero value of Δ, and the system enters the superfluid phase. Since the transition evolves continuously as a function of temperature, it is called a continuous, or second-order, phase transition and it is shown in Figs. 3.2(a) and (b). For $h \neq 0$, the minimum at $\Delta = 0$ can also be a local minimum, so that there is both a local maximum and a global minimum at values of Δ unequal to zero. As is seen in Figs. 3.2(c) and (d), this can cause a discontinuous, or first-order, phase transition. The extrema of the thermodynamic potential density can be found by differentiating with respect to Δ^* and equating the result to zero. As the above discussion implies, there is always one solution given by $\Delta = 0$. The other solutions are found from the so-called BCS gap equation

$$\frac{1}{\mathcal{V}} \sum_{\mathbf{k}} \left[\frac{1 - f(\hbar\omega_{\mathbf{k},+}) - f(\hbar\omega_{\mathbf{k},-})}{2\hbar\omega_{\mathbf{k}}} - \frac{1}{2\epsilon_{\mathbf{k}}} \right] = 0 \ , \tag{3.3}$$

which thus has either one or two solutions. The study of the extrema of the thermodynamic potential allows for a determination of the phase diagram as a function of the chemical potentials and the temperature, which we perform in Paragraph 3.2.2.

3.2.1 Sarma phase

But first, let us briefly discuss in more detail the homogeneous superfluid phases that we expect to encounter in this phase diagram. Below the critical temperature T_c, we have that $|\Delta| \neq 0$, in which case we distinguish between two possibilities. Namely, we have either that $h < |\Delta|$, or that $h > |\Delta|$. The first case we call a BCS superfluid, because, as we see next, it corresponds to the fully-gapped situation known from ordinary BCS superconductivity in metals [2]. The second case leads to a so-called Sarma superfluid, which gives rise to a gapless quasiparticle dispersion for the majority spin species $\hbar\omega_{\mathbf{k},+}$, as was first discussed by Sarma [59]. The Sarma phase is sometimes also referred to as the interior-gap phase or the breached-pair phase [61, 63]. To see the difference between the two phases more clearly, we discuss the notion of a quasiparticle and the meaning of its dispersion in more detail. A spin-up (down) quasi-particle is a linear combination of a spin-up (down) particle and a spin-down (up) hole, see e.g. Ref. [30], namely

$$\hat{b}^\dagger_{\mathbf{k},+} = u_{\mathbf{k}} \hat{a}^\dagger_{\mathbf{k},+} - v_{\mathbf{k}} \hat{a}_{-\mathbf{k},-}, \tag{3.4}$$

$$\hat{b}^\dagger_{-\mathbf{k},-} = v_{\mathbf{k}} \hat{a}_{\mathbf{k},+} + u_{\mathbf{k}} \hat{a}^\dagger_{-\mathbf{k},-}, \tag{3.5}$$

where $\hat{a}^\dagger_{\mathbf{k},\sigma}$ creates a particle with wavevector $\mathbf{k}$ and spin σ, while $\hat{b}^\dagger_{\mathbf{k},\sigma}$ creates a quasiparticle. Note that we have chosen real coherence factors $u_{\mathbf{k}}$ and $v_{\mathbf{k}}$. Quasiparticles behave like ordinary particles in the sense that they can be assigned an energy, wavevector and spin.

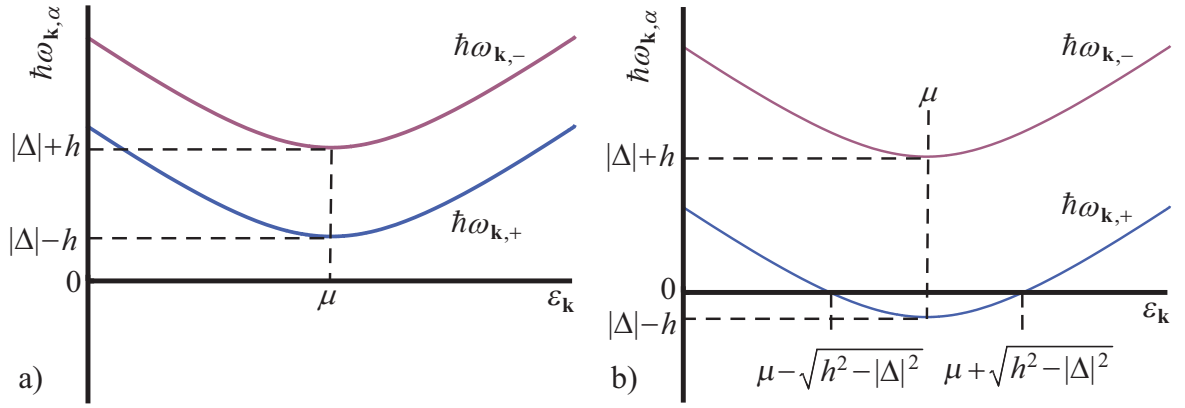

Figure 3.3: Quasiparticle dispersions for a) the BCS superfluid phase and b) the Sarma superfluid phase. The upper branch gives the dispersion for the spin-down quasiparticles, that consist of spin-down particles and spin-up holes. The lower branch gives the dispersion for the spin-up quasiparticles, that consist of spin-up particles and spin-down holes. These dispersions have their minima given by $|\Delta| \pm h$ at wavevectors for which $\epsilon_{\mathbf{k}} = \mu$. In the BCS case the quasiparticle spectra are gapped. In the Sarma case, a part of the spin-up quasiparticle branch is below zero, such that its filling lowers the ground-state energy. As a result, additional spin-down holes and spin-up particles enter the ground state leading to a polarized superfluid.

Physically, a quasiparticle excitation describes a single-particle excitation on top of the Cooper pair condensate. To make such an excitation, first a Cooper pair has to be separated into two uncorrelated atoms, after which one of the particles is taken out of the system, while the other remains. The remaining particle then determines the spin of the quasiparticle excitation. The energy difference between the excitations of different spin is thus $2h$, namely the difference in the chemical potentials between the two spin states. The quasiparticle dispersions are shown in Fig. 3.3, where panel (a) corresponds to the BCS case and panel (b) to the Sarma case. The upper curve in Fig. 3.3(a) shows the spin-down quasiparticle spectrum $\hbar\omega_{\mathbf{k},-}$ and the lower curve shows the spin-up quasiparticle spectrum $\hbar\omega_{\mathbf{k},+}$. It is seen that it cost a certain nonzero amount of energy to make an excitation in one of the two branches, which are therefore said to be fully gapped. At zero temperature, both branches are completely empty, such that only the equal-density BCS ground state, describing the condensate of Cooper pairs, remains. In Fig. 3.3(b), the same quasiparticle dispersions are drawn for the gapless Sarma phase, which arises when $h > |\Delta|$. The curves have the same interpretation as for the gapped BCS case, however, now the branch for the majority spin-up quasiparticles $\hbar\omega_{\mathbf{k},+}$ goes through zero at the wavevectors satisfying $\epsilon_{\mathbf{k}} = \mu \pm \sqrt{h^2 - |\Delta|^2}$. As a result, this additional part of the quasiparticle branch below zero is filled at zero temperature, because in this way the ground-state energy is lowered. The spin-up quasiparticles make the Cooper pairs vanish in the corresponding momentum range, so that here only spin-up particles remain and the superfluid becomes polarized.

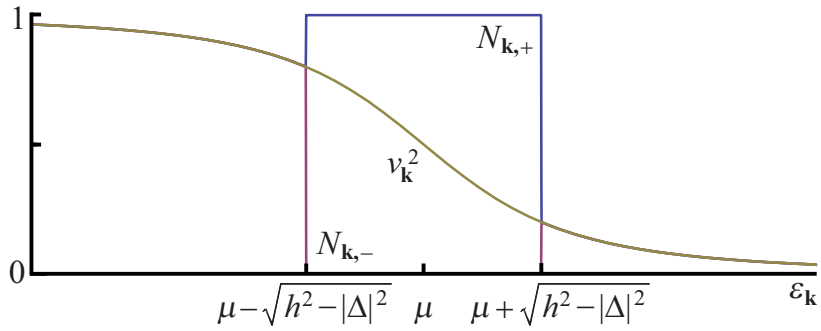

Figure 3.4: Average occupation number $N_{\mathbf{k},\sigma}$ of the single-particle quantum state with momentum $\mathbf{k}$ and spin σ for the Sarma phase. At wavevectors for which $\epsilon_{\mathbf{k}} < \mu - \sqrt{h^2 - |\Delta|^2}$ or $\epsilon_{\mathbf{k}} > \mu + \sqrt{h^2 - |\Delta|^2}$, $N_{\mathbf{k},\sigma}$ equals $v_{\mathbf{k}}^2$ corresponding to the occupation numbers of an equal-density BCS superfluid. For wavevectors in between, $N_{\mathbf{k},+} = 1$ and $N_{\mathbf{k},-} = 0$, such that the superfluid becomes polarized.

We see this more clearly if we explicitly calculate the average occupation number for a single-particle quantum state that is specified by the wavevector $\mathbf{k}$ and spin σ. We designate this occupation number with $N_{\mathbf{k},\sigma}$ and it is given by the expression that is summed over in Eq. (3.2), namely

$$N_{\mathbf{k},\sigma} = |u_{\mathbf{k}}|^2 f(\hbar\omega_{\mathbf{k},\sigma}) + |v_{\mathbf{k}}|^2[1 - f(\hbar\omega_{\mathbf{k},-\sigma})]. \tag{3.6}$$

Indeed, summation over all occupation numbers $N_{\mathbf{k},\sigma}$ yields the total number of particles in state σ. Due to the Pauli principle, $N_{\mathbf{k},\sigma}$ can be maximally unity. In Fig. 3.4, we show the result for $N_{\mathbf{k},\sigma}$ both in the case of a BCS superfluid and a Sarma superfluid at zero temperature. In the BCS case of Fig. 3.3(a), we obtain from Eq. (3.6) that the occupation for both spin states is given by $N_{\mathbf{k},\pm} = v_{\mathbf{k}}^2$ at zero temperature, so that the particle numbers are the same and the superfluid is fully balanced. However, in the Sarma case of Fig. 3.3(b), the additional spin-up quasiparticles, which create extra spin-down holes and spin-up particles, are seen to cause a full polarization near the average chemical potential μ. For the wavevectors leading to a positive quasiparticle dispersion $\hbar\omega_{\mathbf{k},+}$, the BCS behavior is recovered. The resulting configuration for the Sarma phase is sometimes also referred to as 'phase separation' in momentum space. At nonzero temperatures, the sudden rising and lowering of the occupation numbers in Fig. 3.4 becomes smoother, until at high temperatures it disappears.

If the Sarma phase were stable at zero temperature, it would be separated from the BCS phase by a true quantum phase transition, meaning that non-analytic behavior in thermodynamic quantities would be observed as the majority quasiparticle spectrum became gapless. However, as we find in the next section, this gapped-gapless transition is preempted by a first-order phase transition to the normal state, such that the situation $|\Delta| > h$ is seen to be never stable at unitarity. More precisely, we find at zero temperature that when $|\langle\Delta\rangle| = 0.70h$, the transition to the normal state takes

place, where the latter remains the global minimum for larger h. However, at nonzero temperatures, the situation is very different [109]. Namely, close to a second-order phase transition $\langle\Delta\rangle$ becomes arbitrarily small, and the condition for stable gapless superfluidity $|\langle\Delta\rangle| < h$ is readily satisfied. The evolution from the gapped to the gapless regime is at nonzero temperature no longer a phase transition, but rather a smooth crossover, meaning that there is no non-analytic behavior during the evolution. In more exotic situations, the Sarma phase is predicted to be stabilized even at zero temperature. Namely, this may occur when the Sarma phase is induced by confinement [107], or in the case of a very large mass imbalance between the fermionic species in the two-component mixture [63]. The case of a mass-imbalanced Fermi mixture is presented in Chapter 5.

3.2.2 Universal homogeneous phase diagram

Having studied the two homogeneous superfluid phases that are expected to occur in the system, we are now in the position to determine the phase diagram for the two-component Fermi mixture in the unitarity limit. In first instance, we calculate this diagram as a function of the temperature and the chemical potentials. This means that for any given combination of T and μ_σ, we specify whether the global minimum of ω_{BCS} is realized at a zero or a nonzero order parameter $\langle\Delta\rangle$. This determines whether we are in a superfluid or in a normal phase. For the superfluid phase we also specify whether h is larger than $|\langle\Delta\rangle|$ or not. The first case then leads to the gapless Sarma regime, while the second leads to the gapped BCS regime. To calculate the phase diagram we thus need conditions that specify the phase boundary between the superfluid and normal phases, for which there are two possibilities. Namely the transition can be either continuous or discontinuous. This was illustrated in Fig. 3.2.

For the continuous phase transition, the condition is given by the minimum at $\Delta = 0$ becoming a maximum, or equivalently, the second derivative of ω_{BCS} changing sign from positive to negative. The criterion thus becomes

$$\begin{aligned} \alpha_{\mathrm{L}}(T_{\mathrm{c}}) &= \left.\frac{\partial\omega_{\mathrm{BCS}}[\Delta;T_{\mathrm{c}},\mu_\sigma]}{\partial|\Delta|^2}\right|_{|\Delta|=0} \\ &= -\frac{1}{\mathcal{V}}\sum_{\mathbf{k}}\left[\frac{1-f_+(\mathbf{k})-f_-(\mathbf{k})}{2(\epsilon_{\mathbf{k}}-\mu)}-\frac{1}{2\epsilon_{\mathbf{k}}}\right]=0\ , \end{aligned} \tag{3.7}$$

where we introduced the shorthand notation $f_\sigma(\mathbf{k}) = 1/[e^{\beta(\epsilon_{\mathbf{k}}-\mu_\sigma)}+1]$. Note that this condition is only valid when the minimum of ω_{BCS} at $|\Delta| = 0$ is a global minimum before turning into a maximum, as in Fig. 3.2(a). This is something that we have to check. It is certainly the case if, at the critical temperature T_{c}, ω_{BCS} only has nonnegative and positive coefficients for its expansion in $|\Delta|^2$, which is true for the balanced case, $h = 0$. Following the line of second-order phase transitions for increasing h/μ, see the solid line in Fig. 3.5(a), then the first higher-order coefficient of ω_{BCS} that

turns negative is the fourth-order one, which is proportional to

$$\beta_{\mathrm{L}} = \left.\frac{\partial^2 \omega_{\mathrm{BCS}}[\Delta; T, \mu_\sigma]}{(\partial|\Delta|^2)^2}\right|_{|\Delta|=0} = \frac{1}{\mathcal{V}} \sum_{\mathbf{k}} \frac{\beta}{4(\epsilon_{\mathbf{k}} - \mu)^2} \times \left[\frac{1 - f_+(\mathbf{k}) - f_-(\mathbf{k})}{\beta(\epsilon_{\mathbf{k}} - \mu)} + f_+(\mathbf{k})(f_+(\mathbf{k}) - 1) + f_-(\mathbf{k})(f_-(\mathbf{k}) - 1)\right]. \tag{3.8}$$

When both $\alpha_{\mathrm{L}} = \beta_{\mathrm{L}} = 0$, then we are at a so-called tricritical point (TCP). Here, the continuous phase transition turns into a discontinuous one. Below the tricritical point, the condition for the first-order transition line is given by the disconnected normal and superfluid minima having an equal thermodynamic potential density, or $\omega_{\mathrm{BCS}}[0; T_{\mathrm{c}}, \mu_\sigma] = \omega_{\mathrm{BCS}}[\langle\Delta\rangle; T_{\mathrm{c}}, \mu_\sigma]$. This is illustrated in Fig. 3.2(c), where the corresponding behavior of the order parameter as a function of temperature is sketched in panel (d).

The conditions for the phase boundaries lead to the phase diagram of Fig. 3.5(a). Also drawn is the crossover between gapped BCS and gapless Sarma superfluidity, given by the condition $|\langle\Delta\rangle| = h$. A special feature of the phase diagram is that it has a certain kind of universality, due to the divergence of the scattering length [110]. Namely, because now the interaction strength does not provide a physical energy scale, the only energy scales left are associated with the temperature and the particle densities in the system. The latter scales can be characterized by the chemical potentials μ_σ or the Fermi energies $\epsilon_{\mathrm{F}\sigma} = \hbar^2(6\pi^2 n_\sigma)^{2/3}/2m$. By scaling all energies in Fig. 3.5(a) with the average chemical potential μ, the phase diagram becomes only dependent on T/μ and h/μ and not on the specific value of μ anymore. At zero temperature, the first-order superfluid-normal transition occurs when $h_{\mathrm{c}} = 0.81\mu$, at which the gap jumps from $|\langle\Delta\rangle| = 1.16\mu$ to zero. We thus have that $|\langle\Delta\rangle| > h_{\mathrm{c}}$, such that the transition is between an equal density superfluid and a polarized normal state. This means that according to mean-field theory, the Sarma phase does not occur at zero temperature.

In the normal region of the phase diagram, we could in principle make a further distinction between two different normal phases, namely a partially polarized normal phase, where the minority species is still present, and a fully polarized normal state, where only the majority species remains. At zero temperature, the transition between this partially polarized phase and the fully polarized phase happens when $h = \mu$ in mean-field theory. In the phase diagrams that follow we typically do not explicitly make the distinction between the two cases, such that we refer to both phases together simply as the normal phase.

The first-order transition line in Fig. 3.5(a) is characterized by a jump in the order parameter $\langle\Delta\rangle$. From Eq. (3.2), we find that this causes also a jump in the particle densities and in the polarization $p = (n_+ - n_-)/(n_+ + n_-)$. At zero temperature the discontinuity in polarization is largest and mean-field theory predicts a jump from an unpolarized superfluid, $p = 0$, to a normal state with a critical polarization of $p_{\mathrm{c}} = 0.93$. When we calculate for each point in the phase diagram of Fig. 3.5(a) the corresponding particle densities, we find the diagram of Fig. 3.5(b). The phase boundaries are given

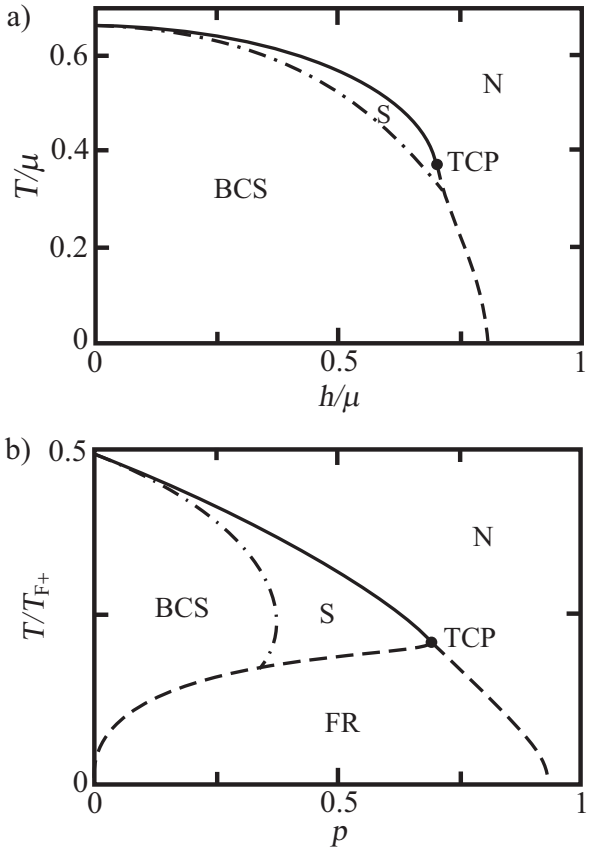

Figure 3.5: a) The phase diagram of the homogeneous two-component Fermi mixture in the unitarity limit, consisting of the gapless superfluid Sarma phase (S), the gapped superfluid BCS phase and the normal phase (N). The transition from superfluid to normal can be either continuous (full line) or discontinuous (dashed line). These two possibilities meet at the tricritical point (TCP). Between the BCS regime and the Sarma regime there is a crossover (dash-dotted line). Both the temperature T and half the chemical potential difference h are scaled with the average chemical potential μ. b) The same diagram but now as a function of the polarization $p = (n_+ - n_-)/(n_+ + n_-)$ with the temperature scaled by the Fermi temperature of the majority species $T_{\mathrm{F}+} = \epsilon_{\mathrm{F}+}/k_{\mathrm{B}}$. Because the transition is discontinuous below the tricritical point, there is a jump in the polarization. It causes a forbidden region (FR) in the phase diagram where the gas is unstable against phase separation.

as a function of p and $T/T_{\mathrm{F}+}$, where the Fermi temperature is defined by $k_{\mathrm{B}}T_{\mathrm{F}\sigma} = \epsilon_{\mathrm{F}\sigma}$. The phase diagram is again universal, such that the phases are uniquely determined by the polarization p and the ratio $T/T_{\mathrm{F}\sigma}$. The diagram in Fig. 3.5(b) is seen to have a forbidden region (FR), which means that the combinations of temperature and polarization inside that region are not stable. At zero temperature, we see for example that the whole region between $p = 0$ and $p = 0.93$ is forbidden. However, as mentioned in the introduction to this chapter, experimentally the polarization can be fixed at any

value. If the system is forced to be in the forbidden region at a certain polarization p_f, then phase separation occurs. It means that the system forms both superfluid regions with low polarization and normal regions with high polarization, such that in total $p = p_\mathrm{f}$ is satisfied.

3.3 Local-density approximation

All experimental set-ups for ultracold atomic quantum gases invoke an external trapping potential, which is needed to keep the atom cloud together for the duration of the experiment. The trapping potential is created by an external magnetic field, that acts on the magnetic dipole moment of the atoms, or by the strong electric field in a laser beam, which induce an electric dipole moment in the atoms. As a result, inhomogeneous magnetic or electric fields become potential energy landscapes for the atoms, with which the particles can be confined in space without using material walls. Since the cold atoms accumulate around the minimum of the potential energy, the trap can typically be well approximated by a harmonic potential. Thus, if we want to describe an actual quantum gas experiment, we inevitably must study the effect of the external potential. This is sometimes inconvenient, because inhomogeneous systems are typically tough to deal with theoretically. Fortunately, if the trapping potential is locally flat enough, then we may consider the gas to be homogeneous at that point in the trap. This is the physical essence of the local-density approximation (LDA). The flatness condition implies that the trapping potential has to vary slowly compared to the typical local de Broglie wavelength of the particles. In this sense, LDA can be seen as a WKB or a semiclassical approximation.

If we apply the condition for the validity of the WKB approximation [76] along a certain direction $r_i \in \{x, y, x\}$ in the trap, we obtain

$$\frac{\hbar m \partial V^\mathrm{ex}(\mathbf{r})/\partial r_i}{[2m\epsilon_{\mathrm{F}\sigma}(\mathbf{r})]^{3/2}} = \frac{r_i/l_i}{6\pi^2 n_\sigma(\mathbf{r}) l_i^3} \ll 1, \tag{3.9}$$

where the trapping potential is given by $V^\mathrm{ex}(x, y, z) = (m\omega_x^2 x^2 + m\omega_y^2 y^2 + m\omega_z^2 z^2)/2$, the harmonic oscillator length in the direction of r_i yields $l_i = (\hbar/m\omega_i)^{1/2}$, and where the Fermi energy $\epsilon_{\mathrm{F}\sigma}(\mathbf{r}) = \hbar^2(6\pi^2 n_\sigma(\mathbf{r}))^{2/3}/2m$ sets locally the typical kinetic energy scale for the atoms. For the MIT experiments, we have $\omega_x = \omega_y = 2\pi \times 115\ \mathrm{s}^{-1}$ in the radial direction, and $\omega_z = 2\pi \times 22.8\ \mathrm{s}^{-1}$ in the axial direction. Moreover, the total number of trapped atoms is about 10^7, leading to central densities on the order of $10^{18}\ \mathrm{m}^{-3}$ [102]. In Fig. 3.8, typical density profiles are shown for the MIT experiments at higher temperatures. There, the coordinates r_i have been rescaled by a factor ω/ω_i with $\omega = (\omega_x\omega_y\omega_z)^{1/3}$, so that the trapping potential conveniently becomes spherically symmetric. As a result, only the radial coordinate is needed to specify the position in the trap. From Eq. (3.9) and Fig. 3.8, we see that the MIT experiments indeed easily satisfy the condition for the local-density approximation in both the radial and the axial direction. Only near the edge of the cloud, where the atomic densities

become very small, the approximation breaks down. For the Rice experiment, we have that $\omega_x = \omega_y = 2\pi \times 350$ s^{-1} and $\omega_z = 2\pi \times 7.2$ s^{-1}, while their total number of particles is about a 10^5 [25]. As a result, a question mark arises over the validity of the local-density approximation for their experiment, especially in the case of large spin-imbalance. Namely, then the left-hand side of Eq. (3.9) is not much smaller than unity anymore for the minority atoms in the steep radial direction.

However, in the rest of this section we focus more on the MIT experiments and we assume that it is valid to use the LDA. The approximation then conveniently allows us to absorb the trapping potential in the chemical potentials and use locally the homogeneous theory that was developed in the previous section. As a result, we have for a spherically symmetric trap (or in rescaled units) that $\mu_\sigma(\mathbf{r}) = \mu_\sigma - V^{\mathrm{ex}}(\mathbf{r}) = \mu - m\omega^2 r^2/2$, which leads for the local average chemical potential to $\mu(\mathbf{r}) = \mu - V^{\mathrm{ex}}(\mathbf{r}) = \mu - m\omega^2 r^2/2$, while (half) the difference remains constant, i.e. $h(\mathbf{r}) = h$. Moreover, we can calculate the total particle number N_σ with spin σ in the trap by

$$N_\sigma = \int d\mathbf{r}\; n_\sigma[\langle\Delta\rangle; T, \mu_\sigma(\mathbf{r})], \tag{3.10}$$

where the local particle densities $n_\sigma[\langle\Delta\rangle; T, \mu_\sigma(\mathbf{r})]$ are given by Eq. (3.2). Since at position $\mathbf{r}$ in the trap the homogeneous phase is realized that corresponds to $T/\mu(\mathbf{r})$ and $h/\mu(\mathbf{r})$, we can already predict what the trapped configurations look like by considering only the homogeneous phase diagram of Fig. 3.5(a). Namely, we may draw an arrow in the homogeneous diagram that precisely follows those ratios $T/\mu(\mathbf{r})$ and $h/\mu(\mathbf{r})$ that are encountered in the trap [99]. We put the tail of the arrow at $T/\mu(\mathbf{0})$ and $h/\mu(\mathbf{0})$ corresponding to the center of the trap. For increasing r or decreasing $\mu(\mathbf{r})$, both ratios increase and the arrow consequently moves to the right and to the above in the diagram, so that we end up in the normal phase. Only when both $h = T = 0$, we stay in the origin of the diagram and superfluidity is encountered throughout the trap. For $h = 0$ and $T \neq 0$, the arrow moves upward along the vertical axis and we encounter a second-order superfluid-to-normal transition in the trap.

However, we are interested in the polarized case, such that we consider $h > 0$. Then, the arrows can follow six different types of paths, corresponding to six trapped phases, as shown in Fig 3.6. The first case is when the whole trap is in the normal phase as follows from arrow (a). The corresponding schematic representation of the trapped phase is depicted on the right in Fig. 3.6. In this representation, we schematically show which phases are encountered as a function of the radius r in the trap. The thick circle then represents the edge of the cloud. The second case is indicated by arrow (b), where the cloud has a BCS superfluid core. For increasing r, we now first encounter a crossover to the gapless Sarma regime, after which there is a second-order phase transition to the normal phase. The third case, arrow (c), leads to a gapless superfluid core, which is separated from the normal outer region by a second-order transition. The fourth case, arrow (d), has a fully gapped superfluid core, surrounded by a Sarma shell, which is separated from the normal state by a first-order transition. The fifth case, arrow (e), has a gapless superfluid core, and the transition to the normal state in

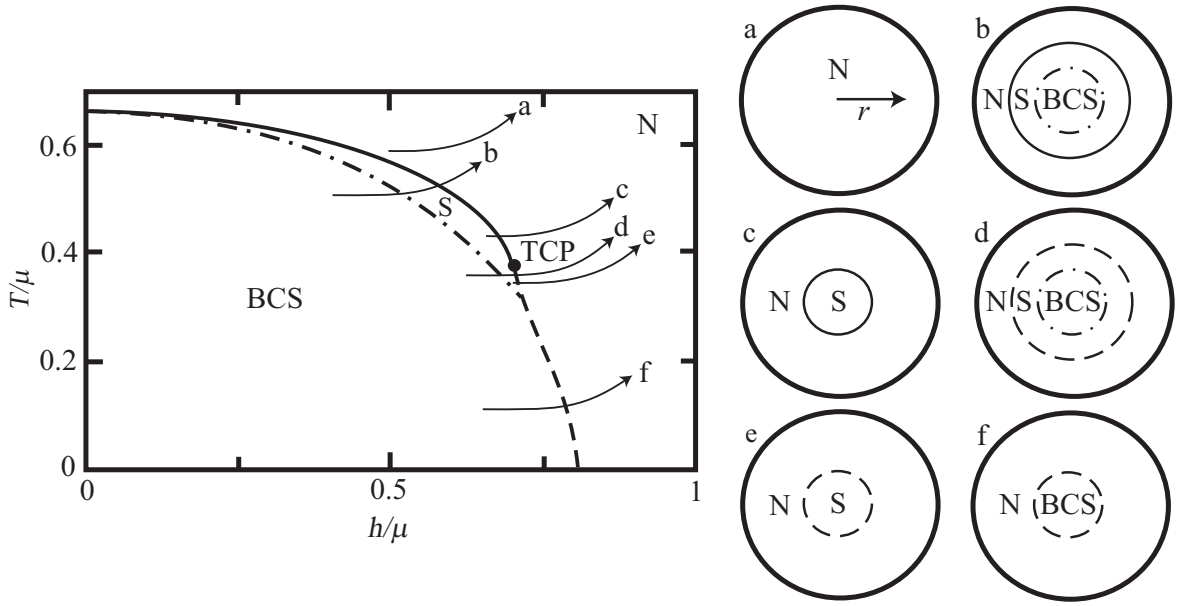

Figure 3.6: The homogeneous phase diagram of Fig. 3.5 with 6 arrows (a)-(f) that represent 6 polarized phases in a trap. The tail of the arrow corresponds to the center of the trap, while the decrease of $\mu(\mathbf{r})$ for increasing radius r causes the arrow to move up and to the right. For each arrow, we draw a schematic representation of the corresponding trapped phase. The center of the spheres correspond to the centers of the trap, while the thick full line denotes the edge of the cloud. The core of the cloud can be either in the normal phase (N), the gapped superfluid phase (BCS) or the gapless superfluid phase (S). These locally homogeneous phases are separated in the trap by either a second-order transition (thin full line), a first-order transition (dashed line) or a crossover (dash-dotted line).

the trap is of first order. The sixth case, arrow (f), is similar to the fifth case, only the core is now fully gapped.

In the next section, we present the universal phase diagram for the strongly interacting Fermi mixture in a trap. Although we have specified 6 trapped phases, some of them only differed by the presence of a crossover. Since a crossover connects different physical regimes in a smooth manner, these regimes are strictly speaking not different thermodynamic phases due to the absence of a true phase transition. In that sense the Sarma phase and the BCS phase are two different limits of the same polarized superfluid phase at nonzero temperatures. In the BCS limit, the polarization is caused by thermal excitation of the gapped quasiparticle branches, whereas in the Sarma limit the gapless branch in principle does not need temperature to be filled. If we choose to classify the trapped phases solely in terms of the true phase transition that occurs in the trap, only three different trapped phases remain. First of all there is the normal phase, given by arrow (a), for which there is no transition in the trap. The second phase has a second-order transition in the trap, such that it encompasses both arrows (b) and (c). Note that the phases (b) and (c) have in common that there is always a

region of Sarma superfluidity present. Therefore, we call the phase with a second-order transition in the trap also the Sarma phase. The third trapped phase has a first-order transition in the trap and thus encompasses arrows (d), (e) and (f). Due to the presence of a first-order interface, we also call it the phase-separated phase. The three different trapped phases are also illustrated in Fig. 3.1.

3.4 Universal phase diagram for the trap

The main results of our mean-field calculations in the trap are presented in Fig. 3.7. Here, we show the universal phase diagram of a trapped Fermi gas in the unitarity limit as a function of temperature and polarization.[1] This phase diagram is universal in the sense that it does not depend on the total number of fermions or the trap geometry. Note that in determining the phase diagram we have neglected fluctuations, which are known to be quantitatively important in the unitarity limit. However, fluctuations are not expected to alter the topology of the phase diagram, and we come back to their effects later this chapter and in the next chapter. Fig. 3.7 reveals that there is a tricritical point in the trapped Fermi mixture, which has been well studied for the homogeneous case [59, 99, 111], but not for the harmonically trapped situation. As explained in the previous section, the normal phase means that the gas is in its normal state throughout the trap. In the Sarma phase the Fermi gas has a shell structure, in which the core of the trapped gas is superfluid, whereas the outer region is normal. Furthermore, the normal-to-superfluid transition as a function of the position in the trap is of second order. Since the superfluid order parameter $\langle\Delta\rangle$ vanishes continuously at the transition, we have for nonzero polarizations always a region in the trap where $|\langle\Delta\rangle|$ is so small that it results in a gapless superfluid with negative quasiparticle excitation energies, as first studied by Sarma [59]. Since $|\langle\Delta\rangle|$ increases towards the center of the trap, it is also possible that the superfluid becomes gapped in the center of the trap. This leads to a gapped BCS superfluid core with a gapless Sarma superfluid and normal shell surrounding it [104]. Finally, in the phase-separated region of the phase diagram, the superfluid core and the normal shell of the gas are separated by a first-order transition as a function of position, which implies that $\langle\Delta\rangle$ goes discontinuously to zero at a certain equipotential surface in the trap.

Fig. 3.7 allows for a natural explanation of the qualitative differences in the early observations by the experimental groups at MIT [102] and Rice university [25]. More precisely, we argue next that the experiments of Zwierlein *et al.* have observed the transition from the normal phase to the Sarma phase at a large polarization [102], implying that these experiments have been performed above the temperature of the tricritical point. Moreover, we suggest that the experiments of Partridge *et al.* have been performed in the temperature regime below the tricritical point, since these experiments appear to see the transition between a non-phase-separated and a phase-separated su-

[1] This section and the next section are directly based on *Sarma Phase in Trapped Unbalanced Fermi Gases*, K. B. Gubbels, M. W. J. Romans, and H. T. C. Stoof, Phys. Rev. Lett. **97**, 210402 (2006).

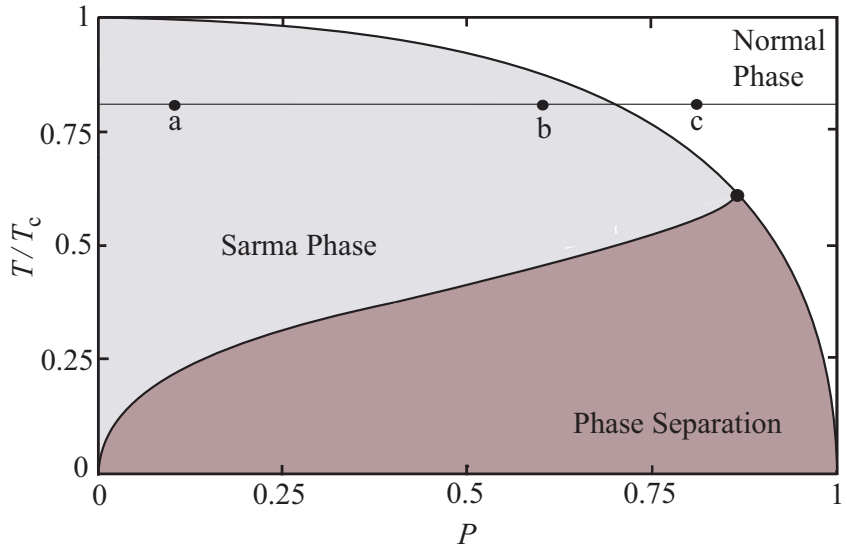

Figure 3.7: Universal phase diagram of a trapped imbalanced Fermi gas in the unitarity limit. The polarization P is given by $(N_+ - N_-)/(N_+ + N_-)$, where $N_\pm$ designates the number of fermions in each hyperfine state of the Fermi mixture. The temperature T is scaled with the critical temperature T_c of the balanced trapped Fermi gas. The solid horizontal line gives the temperature that is used for the comparison with the experiments of Zwierlein *et al.* presented in Figs. 3.8 and 3.9. The points a, b, and c correspond to the polarizations used in the density profiles of Figs. 2(a), 2(b), and 2(c).

perfluid phase at small polarization [25]. However, we would like to emphasize that the local-density approximation that was used to obtain the phase diagram in Fig. 3.7 is not sufficiently accurate to describe all aspects of the experiments of Partridge *et al.* [93, 94, 95, 103]. For this reason we consider here only the experiment of Zwierlein *et al.*, where a more detailed comparison with our theory turns out to be possible.

To obtain the phase diagram of Fig. 3.7, we use the mean-field theory for the Sarma phase in the local-density approximation as described by Houbiers *et al.* [109], where it was used to treat the case of weak interactions. Here, we incorporate the effects of strong interactions by using a generalization of the approach put forward by Fregoso and Baym [112]. Namely, we add selfenergy effects to the mean-field theory by introducing renormalized chemical potentials that are given by $\mu'_\sigma = \mu_\sigma - \hbar\Sigma_\sigma$ with $\hbar\Sigma_\sigma$ the fermionic selfenergies. We use these renormalized chemical potentials in the BCS thermodynamic potential density $\omega_{\rm BCS}[\langle\Delta\rangle; T, \mu'_\sigma]$ of Eq. (3.1), and in the corresponding expressions for the atomic densities $n_\sigma[\langle\Delta\rangle; T, \mu'_\sigma]$ of Eq. (3.2), and in the gap equation (3.3). Note that the resulting expression for the density n_σ does not satisfy the thermodynamic relation $-\partial\omega_{\rm BCS}/\partial\mu_\sigma$ anymore, because we use selfenergies that, as we see next, depend in a complex manner on μ_σ. In Paragraph 5.3, we discuss a simple way in which this problem can be overcome. At unitarity, we then approximate

the selfenergies by

$$\hbar\Sigma_\sigma = \frac{3\pi^2\hbar^2}{m}(\beta_{\rm MC} - \beta_{\rm BCS})\sqrt{\frac{\hbar^2}{m}\frac{1+\beta_{\rm BCS}}{2\mu'}}\; n_{-\sigma}\;, \tag{3.11}$$

which can be understood as follows. Since the average kinetic energy of the atoms involved in the interaction is given by $2\mu'$, the effective interaction strength between the atoms is expected to be proportional to $1/\sqrt{2\mu'}$ [112]. To understand also the proportionality constant we make use of the fact that in the balanced case at zero temperature, BCS theory leads to $\mu = \mu_\sigma = (1+\beta_{\rm BCS})\epsilon_{\rm F}$, where $\beta_{\rm BCS} \simeq -0.41$ [93] and where the Fermi energy is given by $\epsilon_{\rm F} = \hbar^2(3\pi^2 n)^{2/3}/2m$ with $n = n_+ + n_-$ the total atom density. Therefore, we now have that $\mu'_\sigma = (1+\beta_{\rm BCS})\epsilon_{\rm F}$. Using this result together with Eq. (3.11), we find for the balanced case that $\mu = \mu_\sigma = \mu'_\sigma + \hbar\Sigma_\sigma = (1+\beta_{\rm MC})\epsilon_{\rm F}$, which agrees with the exact result from Monte-Carlo calculations upon using $\beta_{\rm MC} \simeq -0.58$ [113, 114].

The above theory is constructed for a homogenous Fermi mixture in the unitarity limit. To account for the presence of an axially symmetric trapping potential $V^{\rm ex}(\mathbf{x}) = m(\omega_\perp^2\rho^2 + \omega_z^2 z^2)/2$ with $\rho = (x^2+y^2)^{1/2}$, we use the local-density approximation. As a result, the local renormalized chemical potential is given by $\mu'_\sigma(\mathbf{x}) = \mu_\sigma - V^{\rm ex}(\mathbf{x}) - \hbar\Sigma_\sigma(\mathbf{x})$. For a balanced Fermi gas at zero temperature, we then have $\mu_\sigma - V^{\rm ex}(\mathbf{x}) = (1+\beta_{\rm MC})\epsilon_{\rm F}(\mathbf{x})$ and therefore we retrieve, as desired, the exact density profile in this case. Note that in the outer region of the gas cloud the renormalized chemical potentials can become negative, so that $2\mu'(\mathbf{x})$ in Eq. (3.11) is no longer a good estimation for the local average kinetic energy of the interacting fermions. Therefore, we then take $3k_{\rm B}T$ instead of $2\mu'$ as an appropriate measure for the kinetic energy.

We are now in the position to explain how we obtain the phase diagram of Fig. 3.7. We first determine the line between the normal and the two superfluid phases. This is achieved by solving the BCS gap equation in the center of the trap and finding the temperature at which the BCS order parameter vanishes. Inspection of the thermodynamic potential reveals that the vanishing of the order parameter can occur continuously or discontinuously, i.e., by a second-order or a first-order phase transition. If the transition is of first/second order, we go from the normal to the phase-separated/Sarma phase. At the tricritical point these two different kinds of transitions merge. So far, we only looked at the center of the trap, but the tricritical condition can also be satisfied at a certain equipotential surface outside the center of the trap. This gives us a point on the Sarma-to-phase-separation line. To see this, consider a point on this line and raise the temperature slightly. This changes the tricritical transition outside the center of the trap into a second-order transition slightly closer to the center of the trap, which means that the gas is in the Sarma phase. In a similar way, a slightly lower temperature leads to a first-order transition as a function of position in the trap, i.e. to the phase-separated phase.

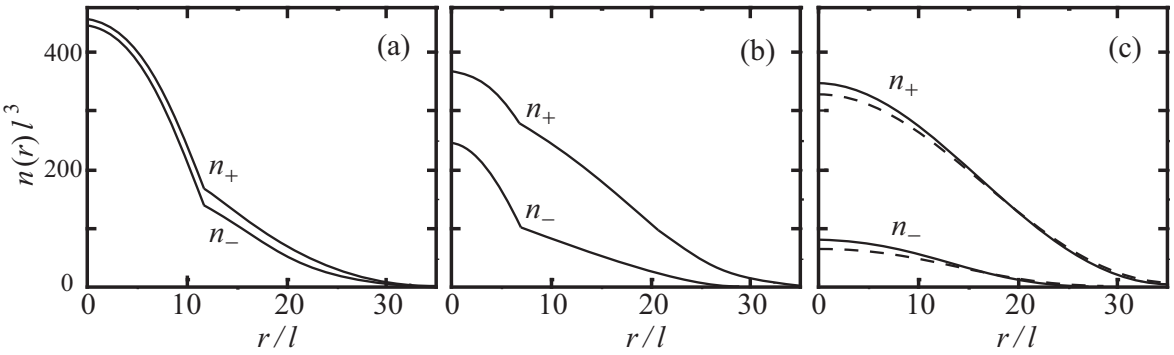

Figure 3.8: Typical density profiles for the trapped unbalanced Fermi gas above the tricritical point. The axial and radial directions of the trap are scaled in such a manner that the trap becomes effectively isotropic with a frequency $\omega = (\omega_\perp^2 \omega_z)^{1/3}$ and a trap length $l = (\hbar/m\omega)^{1/2}$. The temperature and the polarizations used for the three panels are indicated in Fig. 3.7. The total number of atoms is $N = 1.4 \cdot 10^7$. The dashed lines in panel (c) show the corresponding ideal gas results.

3.4.1 Comparison with experiment

We now compare our theory with the experiments of Zwierlein *et al.* [102]. First, we show in Fig. 3.8 three typical density profiles of the gas cloud: two in the superfluid Sarma phase and one in the normal phase. The most striking feature in the density profiles is the 'bulge' in the minority and majority profiles in the Sarma phase. This 'bulge' is a direct consequence of the presence of the condensate of Cooper pairs and was indeed one of the most important findings of the experiment [102]. It shows that for an imbalanced unitarity gas, in contrast to an imbalanced Fermi gas in the BCS limit [109], the condensate of Cooper pairs has a very strong effect on the atomic density profiles. In the normal phase the attractive effects of the selfenergies given in Eq. (3.11) also slightly increase the central densities of the two species. However, this occurs always in a smooth featureless manner whereas in the experiments of Zwierlein *et al.* [102] a distinct feature is seen in the majority density profile at the edge of the minority cloud. This is maybe due to the fact that our mean-field-like selfenergies are intended to exactly incorporate the $\beta_{\rm MC}$ parameter of the balanced unitarity gas, but only approximately account for the strong correlations in the normal phase of the imbalanced unitarity gas. We come back to this point in the next section. Another explanation could be that in the experiment the density profiles are determined after an expansion. This affects in particular the majority density profile, since the outside of the majority cloud expands ballistically, whereas its inner part inside the minority cloud expands hydrodynamically and thus faster than the outer part. The expansion is therefore not determined by a single scale factor and this may lead to a pile up of majority atoms in the transition region. Indeed, the later experiments that were performed in situ, rather than after expansion, did not show this feature in the majority profiles anymore [87].

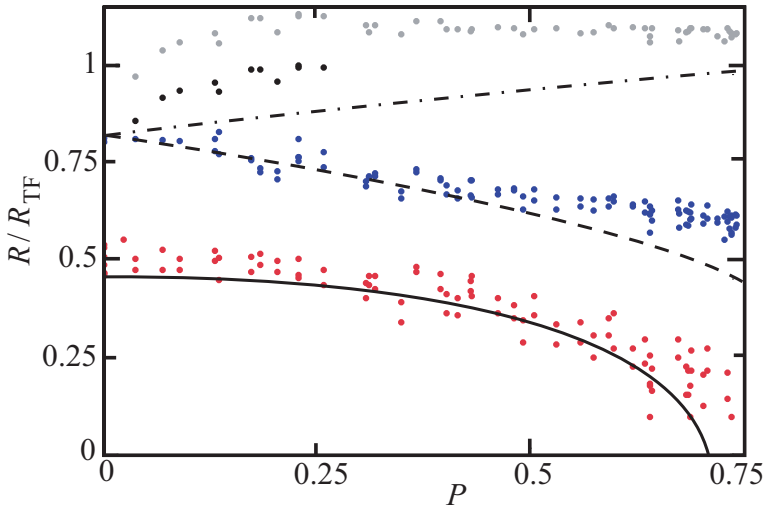

Figure 3.9: The radial size R of the Cooper-pair condensate (solid), and the minority (dashed) and majority (dot-dashed) gas clouds as a function of polarization for the temperature shown in Fig. 3.7. All radial sizes R are scaled with the radial Thomas-Fermi radius of the balanced Fermi gas R_{TF}. Also shown is the experimental data of Zwierlein *et al.* [102]. For the radial size of the majority cloud the black points assume a hydrodynamic expansion, whereas the grey points assume a ballistic expansion.

Besides the above qualitative comparison, we also try to make a quantitative comparison with the experiment of Zwierlein *et al.* by determining the radial size of the Cooper-pair condensate and the radial sizes of the minority and majority gas clouds. The radial size of the Cooper-pair condensate follows directly from the point where $\langle\Delta\rangle(\mathbf{x}) = 0$, but the determination of the minority and majority radii is somewhat more complicated because we are working at a nonzero temperature and the density profiles always have a gaussian tail. For simplicity we determine these radial sizes by the conditions $\mu'_\sigma(\mathbf{x}) = 0$, which give the correct results at $T = 0$, but underestimate the radial size of the density profiles at nonzero temperatures. The results of this procedure together with the experimental data are shown in Fig. 3.9. In general, the agreement with experiment is very good, which confirms our picture that the experiment is operating above the tricritical point. In particular, the fact that at zero polarization the size of the Cooper-pair condensate is significantly smaller than the thermal cloud signals a relatively high temperature. As expected, at small polarizations the radial size of the majority cloud agrees best with the experimental data obtained by assuming a hydrodynamic expansion, whereas for large polarizations our results approach the experimental data obtained by assuming a ballistic expansion.

One of the most important remaining problems of the mean-field theory is the high absolute value of the temperatures above the tricritical point. The calculated temperatures are typically about a factor of 5 higher than what is found in the experiments. An important consequence of the high temperatures is that at the Sarma-to-normal

transition the densities of the two spin states are not equal in the center of the trap in contrast to what is found in experiments. The high absolute value of the temperature is the result of neglecting fluctuations, that substantially shift down the tricritical temperature. Including fluctuations in the case of a balanced Fermi gas reduces the critical temperature in the unitarity limit by about a factor of 3 [115], and fluctuations are expected to be even more important in the imbalanced case. One reason for the latter is that the Sarma phase is a gapless superfluid, whereas the BCS phase at $P = 0$ has a gap. However, theoretically the study of fluctuation effects is rather challenging for an imbalanced Fermi mixture at unitarity, since the usual Nozières-Schmitt-Rink approach [116] has some unphysical features in this case [99]. Therefore, we will apply renormalization group techniques to include fluctuations. This is the topic of the next chapter, where we determine the location of the tricritical point more accurately. However, as mentioned previously, fluctuations are found not to alter the topology of the phase diagram.

3.5 Strongly interacting normal state

So far, we have applied mean-field theory to study the phase diagram of the spin-imbalanced Fermi mixture in the unitarity limit. Moreover, we showed how this theory can be improved to obtain the correct homogeneous equation of state for the balanced superfluid phase at zero temperature, given by $\mu = (1+\beta_{\mathrm{MC}})\epsilon_{\mathrm{F}}$. However, the question remains whether the selfenergy of Eq. (3.11) is also suited to describe interaction effects in the normal state. This question touches upon one of the main shortcomings of the BCS mean-field theory that we used. Namely this theory only takes the interaction of the quasiparticles with the condensate of Cooper pairs nonpertubatively into account and not the interaction between the quasiparticles themselves. To put it differently, once the condensate has vanished in the normal state, then the thermodynamic potential $\omega_{\mathrm{BCS}}[0; T, \mu_\sigma]$ reduces to that of a noninteracting Fermi gas. As a result, it can unfortunately not lead to an accurate description of the normal state, because the particles are actually very strongly interacting, as follows from the diverging scattering length.

The additional selfenergy effects from Eq. (3.11) improve the situation somewhat, since they also give rise to interaction effects in the normal state. However, these turn out to be too small. The reason for this underestimation is that the selfenergies of Eq. (3.11) were constructed for the superfluid state to make up for the relatively small difference between the total interaction energy and its dominant contribution due to the Cooper-pair condensate, which the BCS theory already takes into account. However, in the normal state this dominant contribution has vanished and the selfenergy should now actually describe the relatively big difference between the total interaction energy and no interaction energy at all. The first study of the strongly interacting normal state was a zero-temperature Monte-Carlo calculation by Lobo *et al.* [106]. Our goal is to achieve a description of the normal state which agrees with the Monte-Carlo equation

of state at zero temperature, but which is also extendable to low nonzero temperatures. We do this in two different ways, which are both numerically less involved than the Monte-Carlo simulations. The first way, which we describe next, is a generalization of the selfenergy approach that we used earlier in this chapter. The second approach applies the Wilsonian renormalization group scheme to the unitary Fermi mixture, and is discussed in the next chapter.

The results of the Monte-Carlo calculations at zero temperature are shown in Fig. 3.10. The circles present the data, while the full line is the best fit to this data. The dashed line represents the following ansatz for the total energy density ϵ of the interacting system [106],

$$\begin{aligned} \epsilon &= \frac{3}{5}n_+\epsilon_{\mathrm{F}+} + \frac{3}{5}\frac{m}{m^*}n_-\epsilon_{\mathrm{F}-} - \frac{3}{5}A\epsilon_{\mathrm{F}+}n_- \\ &= \frac{3}{5}n_+\epsilon_{\mathrm{F}+}\left(1 + \frac{m}{m^*}x^{5/3} - Ax\right), \end{aligned} \tag{3.12}$$

where $x = n_-/n_+$. This ansatz was constructed to treat the extremely polarized regime. It physically describes a few spin-down atoms in a spin-up Fermi sea, where the minority atoms have acquired an effective mass of $m^* = 1.04m$ and a selfenergy of $-3A\epsilon_{\mathrm{F}+}/5$ with $A = 0.97$. Both effects are the result of the strong attractive interactions with the large spin-up Fermi sea, which remains unaffected. To obtain the best fit, an extra term of $0.11x^3$ should be added between the brackets on the right-hand side of Eq. (3.12). The construction of Eq. (3.12) is not suitable to describe the balanced case, $x = 1$, where it causes for example the two chemical potentials μ_σ to be unequal, which is unphysical.

To have an ansatz that is valid for all polarizations, we should write the equation of state from the beginning in a form that is symmetric upon interchange of n_+ and n_-. This reflects the fact that it should not matter for the energy density which of the two spin states is the majority state. Similar to Eq. (3.11), we may try a selfenergy of the form

$$\hbar\Sigma_\sigma(n_+, n_-) = -\frac{3A(6\pi^2)^{2/3}\hbar^2}{10m}\frac{n_{-\sigma}}{(n_+^\alpha + n_-^\alpha)^{1/3\alpha}}, \tag{3.13}$$

where we should still specify the power α. In order to compare this selfenergy with the one from Section 3.4, we note that for the normal state we obtain at zero temperature $\mu'_\sigma = \epsilon_{\mathrm{F}\sigma} \propto n_\sigma^{2/3}$. To make a comparison between Eq. (3.13) and Eq. (3.11), we should thus use $\alpha = 2/3$. Then, we indeed find that the selfenergy of Eq. (3.11) only partly accounts for the strong interactions in the normal state, since its prefactor is about 3 times smaller than the one from Eq. (3.13). If we use the selfenergy of Eq. (3.13) to obtain a total energy density similar to Eq. (3.12), we find

$$\begin{aligned} \epsilon &= \frac{3}{5}n_+\epsilon_{\mathrm{F}+} + \frac{3}{5}n_-\epsilon_{\mathrm{F}-} - \frac{3A(6\pi^2)^{2/3}\hbar^2}{10m}\frac{n_+n_-}{(n_+^\alpha + n_-^\alpha)^{1/3\alpha}} \\ &= \frac{3}{5}n_+\epsilon_{\mathrm{F}+}\left(1 + x^{5/3} - A\frac{x}{(1+x^\alpha)^{1/3\alpha}}\right), \end{aligned} \tag{3.14}$$

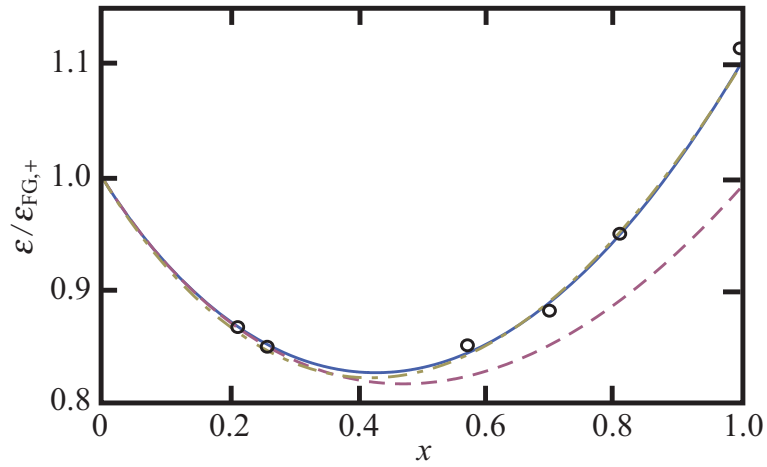

Figure 3.10: Equation of state for the zero-temperature normal phase of the spin-imbalanced Fermi mixture with unitary interactions. The Monte Carlo results by Lobo *et al.* [106] are shown by circles, while $x = n_-/n_+$. The full line represents the best fit to the data. The dashed line gives the result of Eq. (3.12). The dashed-dotted line, which is hard to discern from the best fit, is obtained from Eq. (3.14). The energy density ϵ is scaled with the ideal gas energy for the spin-up particles $\epsilon_{\mathrm{FG},+} = 3\epsilon_{\mathrm{F}+}n_+/5$ with $\epsilon_{\mathrm{F}\sigma} = \hbar^2(6\pi^2 n_\sigma)^{2/3}/2m$.

which agrees for small x with Eq. (3.12). If we wish to obtain agreement with the full Monte-Carlo equation of state, we can take $A = 1.01$ and $\alpha = 2$, which results in the dashed-dotted line shown in Fig. 3.10. It is hardly discernible from the full line that gives the best fit. The value of A is calculated in the next paragraph, while there does not seem to be a direct microscopic argument why α should be 2. It can thus be interpreted as a single fit parameter.

3.5.1 The extremely imbalanced case

We have just seen that the equation of state for the normal state at zero temperature is to a large extent determined by selfenergy effects of the minority (spin-down) atoms in the Fermi sea of majority (spin-up) atoms. In this paragraph, we calculate the selfenergy of a single spin-down atom analytically in the so-called ladder or many-body T matrix approximation [117], rather than using the numerically more involved Monte-Carlo techniques. After we have obtained this selfenergy $\hbar\Sigma_\sigma(\mu_\sigma)$, we again include its effect by renormalizing the corresponding chemical potential as $\mu'_\sigma(\mu_\sigma) = \mu_\sigma - \hbar\Sigma_\sigma(\mu_\sigma)$. The renormalized chemical potentials consequently enter the thermodynamic potential density of the normal gas at zero temperature ω_{N} in the following way

$$\omega_{\mathrm{N}}(\mu_\sigma) = \omega_{\mathrm{BCS}}[0; 0, \mu'_\sigma(\mu_\sigma)] = -\frac{(2m)^{3/2}}{15\pi^2\hbar^3}\left(\mu'_+(\mu_\sigma)^{5/2} + \mu'_-(\mu_\sigma)^{5/2}\right). \tag{3.15}$$

The single-particle limit for spin state σ is located right at the transition from a nonzero particle density to a zero particle density. The latter takes place when μ'_σ goes to zero,

i.e. when $\mu_\sigma = \hbar\Sigma_\sigma(\mu_\sigma)$ [117]. To be able to solve this latter equation, we need to calculate the selfenergy $\hbar\Sigma_\sigma(\mu_\sigma)$ in the extremely imbalanced limit.

We perform this calculation for a single spin-down atom in a Fermi sea of spin-up particles along the lines of Ref. [117]. For unitary interactions and at zero temperature, the many-body T matrix for the extremely imbalanced case is seen to have a particularly simple expression, because the Fermi distributions become step functions and there is no spin-down particle density, resulting in

$$T^{-1}(\mathbf{k}, \hbar\omega) = \int \frac{d\mathbf{k}'}{(2\pi)^3} \left\{ \frac{\theta(\epsilon_{\mathbf{k}'} - \mu_+)}{-\hbar\omega + \epsilon_{\mathbf{k}'} + \epsilon_{\mathbf{k}-\mathbf{k}'} - 2\mu} - \frac{1}{2\epsilon(\mathbf{k}')} \right\} \tag{3.16}$$

where $\theta(x)$ is the Heaviside step function given by $\theta(x) = 1$ for $x > 0$ and $\theta(x) = 0$ for $x < 0$. It gives rise to a selfenergy for the minority particle, which at zero momentum and frequency is given by [117]

$$\hbar\Sigma_-(\mu_\sigma) \;=\; \int \frac{d\mathbf{k}}{(2\pi)^3} T(\mathbf{k}, \epsilon_{\mathbf{k}} - \mu_+)\theta(\mu_+ - \epsilon_{\mathbf{k}}), \tag{3.17}$$

where the substitution $\hbar\omega \to \epsilon_{\mathbf{k}} - \mu_+$ in the T matrix comes from a contour integral over the frequency ω. Then, to fulfill our initial assumption of zero down particles, we still need to solve $\mu'_- = 0$, which leads to $\mu_- = -0.607\mu_+ = -3A\mu_+/5$ with $A = 1.01$. This result means that for a chemical potential lower than $\mu_- = -0.6\mu_+$ there are no spin-down particles, whereas for a higher chemical potential there is a nonzero density of spin-down particles. Of course, the results would be the same for a single spin-up particle in a spin-down sea. There have been several Monte-Carlo calculations for a single fermion with spin σ in a Fermi sea of particles with spin $-\sigma$. The results are $A = 0.97$ [106], $A = 0.99$ [118] and $A = 1.03$ [119], which all agree remarkably well with the simple ladder calculation.

We may try to generalize the fermionic selfenergies by using an ansatz that has the correct extremely imbalanced limits in it, but actually leads to excellent results with Monte-Carlo calculations for all polarizations. This is achieved by introducing the following renormalized chemical potentials

$$\mu'_\sigma = \mu_\sigma + \frac{3}{5} A \frac{\mu'^2_{-\sigma}}{\mu'_+ + \mu'_-}, \tag{3.18}$$

which has a similar structure as Eq. (3.11) but does not directly depend on the particle densities anymore. This is an advantage, since we can now determine analytically the renormalized chemical potentials μ'_σ as a function of the microscopic ones μ_σ, and consequently use $n_\sigma = -\partial\omega_{\mathrm{N}}/\partial\mu_\sigma$ to determine the densities. The two extremely imbalanced solutions to Eq. (3.18) are such that the chemical potential of the majority species $(-\sigma)$ is not renormalized, $\mu'_{-\sigma} = \mu_{-\sigma}$, while the renormalized chemical potential of the minority species σ is zero, $\mu'_\sigma = \mu_\sigma + 3A\mu_{-\sigma}/5 = 0$. It is easy to invert the quadratic relations in Eq. (3.18) to obtain $\mu'_\sigma(\mu_\sigma)$, which motivates the choice for a quadratic ansatz. However, a better validation of the approach is obtained by

comparing with the Monte-Carlo equation of state. We determine the energy density using $\epsilon = \omega_{\rm N} + \mu_+ n_+ + \mu_- n_-$, for which the result is shown in Fig. 5.2. Here, both the result of our procedure (dashed line) and the data of Lobo *et al.* [106] (squares) are shown, giving very good agreement.

Moreover, our approach can also be used at small nonzero temperatures, since the coefficient A is not expected to be strongly temperature dependent. This is because the Fermi sea of majority particles remains unaffected for $T \ll T_{\rm F}$, where the Fermi temperature typically represents a large energy scale in the system. It is given by $k_{\rm B}T_{\rm F} = \epsilon_{\rm F} = \hbar^2(3\pi^2 n)^{2/3}/2m$ with $n = n_+ + n_-$ the total atomic density. We can check our assumption by comparing with a Monte-Carlo calculation at nonzero temperature [120]. In this calculation, the nonuniversal critical properties for the superfluid transition in the balanced Fermi mixture were determined, leading for the critical temperature at unitarity to $T_{\rm c} = 0.15T_{\rm F}$, while the corresponding chemical potential was given by $\mu(0.15T_{\rm F}) = 0.49\epsilon_{\rm F}$ [120]. We can compare the last result with the direct extension of our approach to nonzero temperature, which follows from using $\omega_{\rm N}(T, \mu_\sigma) = \omega_{\rm BCS}[0; T, \mu'_\sigma]$. By applying $n_\sigma = \partial\omega_{\rm N}(0.15T_{\rm F}, \mu_\sigma)/\partial\mu_\sigma$, we obtain $\mu(0.15T_{\rm F}) = 0.53\epsilon_{\rm F}$ in quite close agreement with the Monte-Carlo calculation.

3.5.2 Comparison with experiment

Having obtained the thermodynamic potential density for a homogeneous Fermi mixture in the strongly interacting normal state, we can now use it to also study the normal trapped mixture by means of the local-density approximation [121]. Namely, since we have that the local chemical potential for spin state σ is given by $\mu_\sigma(\mathbf{r}) = \mu_\sigma - V^{\rm ex}(\mathbf{r})$, where μ_σ is the chemical potential in the trap center, we immediately obtain the particle density at each point in the trap by using $n_\sigma(\mathbf{r}) = -\partial\omega_{\rm N}(T, \mu_\sigma(\mathbf{r}))/\partial\mu_\sigma(\mathbf{r})$. In the case that the gas cloud does not have a superfluid core, this procedure gives rise to the complete density profile for the trapped normal phase in the unitarity limit.

However, if the spin imbalance is not too large, then the core of the trapped unitary Fermi mixture is superfluid. In Section 3.4, we mentioned that at zero temperature the Monte-Carlo equation of state for the equal-density superfluid phase is given by $\mu = (1 + \beta_{\rm MC})\epsilon_{\rm F}$ [113, 114]. From this equation of state, we can immediately calculate the energy density of the superfluid. Namely, from the relation $\mu = \partial\epsilon_{\rm SF}/\partial n$, we then obtain upon integration that $\epsilon_{\rm SF} = 3(1 + \beta_{\rm MC})\epsilon_{\rm F} n/5$. As a result, we find for the thermodynamic potential density in the superfluid phase

$$\begin{aligned} \omega_{\rm SF}(\mu_\sigma) &= \epsilon_{\rm SF} - \mu n = -\frac{2}{5}(1 + \beta_{\rm MC})\epsilon_{\rm F} n \\ &= -(1 + \beta_{\rm MC})\frac{2(2m)^{3/2}}{15\pi^2\hbar^3}\left(\frac{\mu}{1 + \beta_{\rm MC}}\right)^{5/2}. \end{aligned} \tag{3.19}$$

When we have that $\omega_{\rm SF}(\mu_\sigma) = \omega_{\rm N}(0, \mu_\sigma)$, then a first-order phase transition between the equal density superfluid and the polarized normal phase occurs. From Eqs. (3.15),

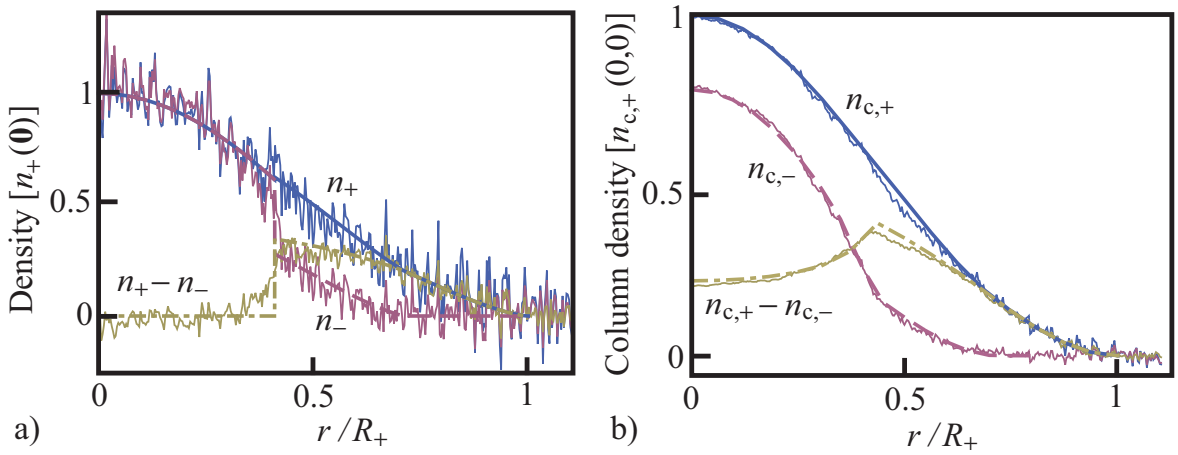

Figure 3.11: Observation of phase separation in a trapped Fermi mixture by Shin *et al.* [87]. The measurement was performed at their lowest temperature of about $T = 0.02T_{F+}(\mathbf{0})$ and a total polarization of $P = 0.44$. Their data are shown by the noisy curves. a) Calculated density profile for the spin-up particles n_+ (full line), the spin-down particles n_- (dashed line), and their difference (dashed-dotted line). The densities are scaled by the central density of the spin-up particles. b) Exactly the same, but now for the column densities, which means that an additional integration along the y axis is performed. Even though the calculations are performed at zero temperature, the agreement is very good.

(3.18) and (3.19), it follows that the critical difference in the chemical potentials is given by $h_c = 0.92\mu$. At this critical value, the (local) polarization jumps from zero in the superfluid phase to $p = (n_+ - n_-)/(n_+ + n_-) = 0.38$ in the normal phase. Note that this result is very different from the mean-field result of Paragraph 3.2.2, where we obtained $p = 0.93$ for the critical polarization. The difference shows the crucial quantitative effect of the strong interactions in the normal state.

By comparing ω_{SF} with ω_N everywhere in the trap, we can determine which of the two phases is locally most favorable and calculate the particle densities from the corresponding equation of state. For the superfluid phase, the local particle densities are obtained from $\mu(\mathbf{r}) = (1+\beta_{MC})\epsilon_F(\mathbf{r})$. We are now thus in the position to determine the density profiles for the trapped phase-separated state, which has a superfluid core and a first-order transition to the normal state as a function of position in the trap. This discontinuous transition has been observed in the density profiles measured by Shin *et al.* [87], as shown in Fig. 3.11. In panel (a), the density profiles are shown for the spin-up particles, the spin-down particles and their difference. The noisy curves are the data, which compare well with the calculated lines. The experimental profiles were obtained at a temperature of about $T = 0.02T_{F+}(\mathbf{0})$, where $T_{F+}(\mathbf{0})$ is the local Fermi temperature of the spin-up particles in the center of the trap. The total polarization was about $P = 0.44$ and the total number of spin-up particles yielded $N_+ = 6 \cdot 10^6$. Moreover, we already specified the trapping potential $V^{ex}(\rho, z) = m(\omega_\perp^2(x^2 + y^2) + \omega_z^2 z^2)/2$ for the

MIT experiments in Section 3.4. From Fig. 3.11(a), we see that the measured densities are equal in the superfluid core, but upon going outwards from the center of the trap there is a sudden rise in the density difference, indicating a first-order transition. In the figure, we used the radial coordinate r given by $\omega^2 r^2 = \omega_\perp^2(x^2+y^2) + \omega_z^2 z^2$ with $\omega = (\omega_\perp^2 \omega_z)^{1/3}$. The calculated profiles are shown by the full line for $n_+(r)$, by the dashed line for $n_-(r)$, and by the dashed-dotted line for their difference. The densities are all scaled by the central density of the spin-up particles $n_+(\mathbf{0})$. The radial distances are scaled in the figure by the radial cloud size of the spin-up atoms, given by $R_+ = (2\mu_+/m\omega^2)^{1/2}$.

In Fig. 3.11(b), also the column densities $n_{\mathrm{c},\sigma}$ are shown, which follow from

$$n_{\mathrm{c},\sigma}(x,z) = \int_{-\infty}^{\infty} dy\; n_\sigma(x,y,z). \tag{3.20}$$

The column densities are less noisy, because they are directly probed by the in-situ imaging that is performed in the experiment, while the densities have to be reconstructed. The radial coordinate for the column density is now given by $\omega^2 r^2 = \omega_\perp^2 x^2 + \omega_z^2 z^2$, while the plotted column densities are all scaled by the central column density of the spin-up particles $n_{\mathrm{c},+}(0,0)$. In general, the agreement between the experimental curves and the theoretical curves is very good. The small differences could be due to the fact that the calculation was performed at zero temperature, while the experiment is at very small nonzero temperature. Moreover, the local-density approximation is expected to fail close to the interface, because a true jump in the order parameter would cost an infinite amount of gradient energy. Actually, if gradient terms are taken into account, then a smooth order-parameter profile is calculated near the interface, as performed by Diederix *et al.* [107]. Since the order parameter now becomes arbitrarily small in a continuous manner, the zero-temperature Sarma phase is inevitably realized in a small range near the interface for nonzero polarizations. It is a confinement-induced Sarma phase [107], because in the absence of the interface it would be unstable. Moreover, close to the interface the incorporation of gradient effects improves the agreement with experiments, where especially in Fig. 3.11(a) the difference profile does not give a perfect match between theory and experiment yet.

Note that throughout the calculation in this paragraph, we have assumed that more exotic superfluid phases, like the FF and LO phases mentioned in Chapter 1, do not play a role at zero temperature in the unitarity limit. To put it differently, we have assumed that the mean-field phase diagrams of Figs. 3.5 and 3.7 are topologically correct. Seen the very good agreement with experiments that we obtained, this assumption thus seems justified. In hindsight, this observation also validates the approach that we have used throughout the chapter. Namely, we invoked mean-field theory to qualitatively discuss the relevant physics at play in the strongly-interacting Fermi mixture with a spin imbalance, although there was no formal reason why this would work. In order to achieve also more quantitative agreement with Monte-Carlo calculations and experiments, the mean-field theory had to be improved by considering selfenergy effects, i.e. by renormalizing the chemical potentials. In the next chapter,

we discuss the renormalization group technique for strongly-interacting fermions, which puts the use of renormalized chemical potentials on a more microscopic and structural ground. We will see that the technique also allows for a quantitative description of the MIT experiments at nonzero temperatures and polarizations, where Monte-Carlo calculations have not been carried out so far. Finally, in Chapter 5 we extend all of our knowledge from the mass-balanced case to the mass-imbalanced ^{6}Li-^{40}K mixture, for which the experiments are just starting.

Chapter 4

Renormalization group theory for fermions

We formulate a Wilsonian renormalization group theory for the imbalanced Fermi gas.[1] The theory is able to recover quantitatively well-established results in both the weak-coupling and the strong-coupling (unitarity) limit. We determine for the latter case the line of second-order phase transitions of the imbalanced Fermi gas and in particular the location of the tricritical point. We obtain good agreement with the experiments of Y. Shin *et al.* [Nature **451**, 689 (2008)].

4.1 Introduction

As we discussed in Chapter 1, the amazing experimental control in the manipulation of degenerate Fermi mixtures has led for the balanced mixture to an accurate study of the crossover between a Bardeen-Cooper-Schrieffer (BCS) superfluid and a Bose-Einstein condensate (BEC) of diatomic molecules. Particularly interesting is the strongly interacting regime, where the scattering length of the interaction becomes much larger than the average interatomic distance. In this so-called unitarity limit, experiments have revealed that the superfluid state is remarkably stable and has a record-high critical temperature of about one tenth of the Fermi energy [9]. Theoretically, the unitarity limit is extremely challenging, because there is no rigorous basis for perturbation theory due to the lack of a small parameter. As a result, mean-field theory is only useful for understanding the relevant physics qualitatively, but cannot be trusted quantitatively. In order to get accurate results, more sophisticated theoretical methods have to be invoked.

An important example is using quantum Monte-Carlo techniques, which can provide exact results about the strongly interacting regime [106, 113, 120, 122], but offer

[1] This chapter is directly based on K. B. Gubbels and H. T. C. Stoof, *Renormalization Group Theory for the Imbalanced Fermi Gas*, Phys. Rev. Lett. **100**, 140407 (2008).

less physical insight than analytic methods. Therefore, several other approaches have been developed to improve on mean-field theory. Examples are theories incorporating Gaussian fluctuations [99, 115, 123, 124, 125], ϵ expansion [126], $1/N$ expansion [127, 128], and the functional renormalization group (RG) [129, 130]. In this chapter, we formulate a Wilsonian RG to study the strongly interacting atomic Fermi mixture with a population imbalance. The intuitively appealing Wilsonian approach, which has been extremely successful in the study of critical phenomena [131, 132], is based on systematically integrating out short-wavelength degrees of freedom, which then renormalize the coupling constants in the effective action for the long-wavelength degrees of freedom. For fermions, the excitations of lowest energy lie near the Fermi level, which is therefore the natural end point for a renormalization group flow [133]. A notorious problem for interacting fermions is that under renormalization the Fermi level also flows to an *a priori* unknown value, making the Wilsonian RG difficult to perform in practice [134, 135]. We show, however, how to obtain RG equations that automatically flow to the final value of the renormalized Fermi level.

The unitary, two-component Fermi mixture with an unequal number of particles in each spin state is a topic of great interest in atomic physics, condensed matter, nuclear matter, and astroparticle physics. It was extensively discussed in the previous chapter, where it was mentioned that the landmark atomic-physics experiments exploring this system, performed at MIT by Zwierlein *et al.* [24] and at Rice University by Partridge *et al.* [25], induced a large amount of activity, caused by an intriguing mix of mutual consistent and contradictory results. In summary, both experiments observed no oscillating order parameter, so that the Fulde-Ferrell and Larkin-Ovchinnikov phases do not seem to play a role in the unitarity limit. Therefore, the experiments are consistent with a phase diagram including both second-order and first-order phase transitions between the superfluid (BCS or Sarma) phase and the normal phase, that are connected by a tricritical point [60, 99]. However, as a function of population imbalance Zwierlein *et al.* obtain a critical imbalance at which the trapped Fermi gas becomes fully normal, whereas Partridge *et al.* observe a superfluid core up to their highest imbalances. Although this contradictory result is still not understood, more recent work implies that the data of Zwierlein *et al.* is consistent with the local-density approximation, whereas the experiments of Partridge *et al.* explore physics beyond this approximation, possibly due to the smaller number of particles and the more extreme aspect ratio of the trap [103, 105].

Since the validity of the local-density approximation implies that the Fermi mixture can be seen as being locally homogeneous, the MIT group is in the unique position to experimentally map out the homogeneous phase diagram by performing local measurements in the trap. Most recently, this important experiment was performed by Shin *et al.* [87], obtaining for the homogeneous tricritical point in the unitarity limit $p_{c3} = 0.20(5)$ and $T_{c3} = 0.07(2)\ T_{F+}$, with p the local polarization given by $p = (n_+ - n_-)/(n_+ + n_-)$, n_σ the density of atoms in spin state $|\sigma\rangle$, T the temperature, and $\epsilon_{F\sigma} = k_B T_{F\sigma} = (6\pi^2 n_\sigma)^{2/3}\hbar^2/2m$ the Fermi energies with m the atomic mass. In this chapter, we use RG to determine its location, and by using two different methods

for calculating the particle densities, we obtain either $p_{c3} = 0.24$ and $T_{c3} = 0.06\ T_{F+}$, or $p_{c3} = 0.14$ and $T_{c3} = 0.06\ T_{F+}$. Both results match the experiment by Shin *et al.* [87].

4.2 Wilsonian renormalization

The central idea of Wilsonian renormalization is to subsequently integrate out degrees of freedom in shells at high momenta $\hbar\Lambda$ of infinitesimal width $d\hbar\Lambda$ and absorb the result of the integrations into various coupling constants, which are therefore said to flow. The first step is then to calculate the Feynman diagrams renormalizing the coupling constants of interest, while keeping the integration over the internal momenta restricted to the considered high-momentum shell [131, 132]. Only one-loop diagrams contribute to the flow, because the thickness of the momentum shell is infinitesimal and each loop introduces a factor $d\Lambda$. In order to obtain exact results, it is needed to consider an infinite number of coupling constants. Although this is not possible in practice, the RG is still able to distinguish between the relevance of the various coupling constants, such that a selected set of them may already lead to accurate results. If we wish to treat critical phenomena by looking at so-called RG fixed points, it is necessary to also perform a second step, namely a rescaling of the momenta, frequencies, and fields [131]. In this chapter, however, we use the renormalization group to calculate nonuniversal quantities, such as the critical temperature, for which rescaling is not particularly useful. The renormalization group then serves as a nonperturbative method to iteratively solve a many-body problem, rather than as a mapping between actions from which critical scaling relations can be derived.

We start with considering the action of a two-component interacting Fermi mixture [30]

$$\begin{aligned} S[\phi^*,\phi] &= \sum_{\mathbf{k},n,\sigma} \phi^*_{\mathbf{k},n,\sigma}(-i\hbar\omega_n + \epsilon_{\mathbf{k}} - \mu_\sigma)\phi_{\mathbf{k},n,\sigma} \\ &+ \frac{1}{\hbar\beta\mathcal{V}} \sum_{\substack{\mathbf{k},\mathbf{k}',\mathbf{q}\\ n,n',p}} V_{\mathbf{q},p}\ \phi^*_{\mathbf{q}-\mathbf{k}',p-n',+}\phi^*_{\mathbf{k}',n',-}\phi_{\mathbf{q}-\mathbf{k},p-n,-}\phi_{\mathbf{k},n,+}\ , \end{aligned} \tag{4.1}$$

where n and n' are odd, p is even, $\epsilon_{\mathbf{k}} = \hbar^2k^2/2m$ is the kinetic energy, μ_σ is the chemical potential for spin state $\sigma = \pm$, $\mathcal{V}$ is the volume, and $\beta = 1/k_BT$. Moreover, $\phi_{\mathbf{k},n,\sigma}$ is the fermionic field corresponding to annihilation of a particle with spin σ, momentum $\hbar\mathbf{k}$ and Matsubara frequency ω_n. We consider an interaction $V_{\mathbf{q},p}$ that in general depends on the center-of-mass frequency $i\omega_p$ and the center-of-mass momentum $\mathbf{q}$, for which the reason becomes clear soon. In Fig. 4.1, we have drawn the one-loop Feynman diagrams that renormalize μ_σ and $V_{\mathbf{q},p}$. To start out relatively simple, we make the approximation that the interaction vertex remains frequency and momentum independent during the RG flow. If we then consider only the three coupling constants

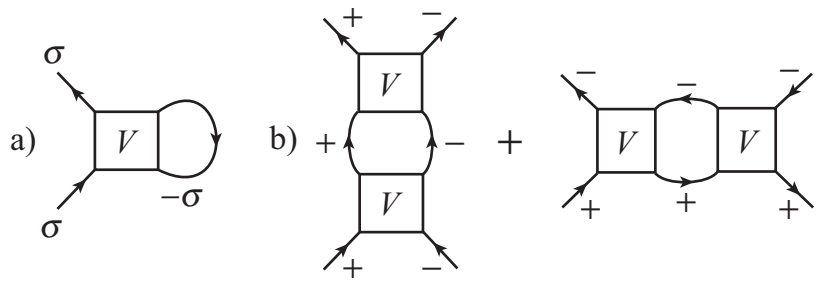

Figure 4.1: One-loop Feynman diagrams renormalizing a) the chemical potentials and b) the interatomic interaction. The right diagram is also called the bubble diagram, while the middle diagram is called the ladder diagram.

μ_σ and $V_{\mathbf{0},0}$, we obtain the following set of coupled RG equations, where the derivation goes along the lines of Refs. [30, 136, 133], namely

$$\frac{dV_{\mathbf{0},0}^{-1}}{d\Lambda} = \frac{\Lambda^2}{2\pi^2}\left[\frac{1-f_+(\Lambda)-f_-(\Lambda)}{2(\epsilon_\Lambda-\mu)} - \frac{f_+(\Lambda)-f_-(\Lambda)}{2h}\right], \tag{4.2}$$

$$\frac{d\mu_\sigma}{d\Lambda} = -\frac{\Lambda^2}{2\pi^2}\frac{f_{-\sigma}(\Lambda)}{V_{\mathbf{0},0}^{-1}}\,. \tag{4.3}$$

Here, we have as before that $\mu = (\mu_+ + \mu_-)/2$, $h = (\mu_+ - \mu_-)/2$ and the Fermi distribution $f_\sigma(\Lambda) = 1/\{\exp[\beta(\epsilon_\Lambda - \mu_\sigma)] + 1\}$. Eqs. (4.2) and (4.3) are readily obtained from the diagrams in Fig. 4.1 by setting all external frequencies and momenta equal to zero and by performing in each loop the full Matsubara sum over internal frequencies, while integrating the internal momenta over the shell at momentum $\hbar\Lambda$ of infinitesimal width $d\hbar\Lambda$. The first term in Eq. (4.2) corresponds to the ladder diagram and describes the scattering of particles in a medium [30]. The second term corresponds to the bubble diagram and describes screening of the interaction by particle-hole excitations [30]. Also note that due to the coupling of the differential equations for μ_σ and $V_{\mathbf{0},0}^{-1}$, we automatically generate an infinite number of Feynman diagrams, showing the nonperturbative nature of the RG.

When the Fermi mixture becomes critical, the inverse many-body interaction vertex $V_{\mathbf{0},0}^{-1}$ flows to zero, which corresponds to the so-called Thouless criterion. This criterion states that the superfluid transition happens for a diverging many-body T matrix at zero external momentum and frequency, which physically implies that a new bound state is entering the system, namely the Cooper-paired state. Note that the combination of Eq. (4.2) with the Thouless criterion generalizes the mean-field result for the critical condition in Eq. (3.7). Namely in the absence of particle-hole fluctuations and without coupling to Eq. (4.3), we have that Eq. (4.2) corresponds to the differential form of Eq. (3.7). To establish their equivalence, we still have to specify the appropriate initial conditions for the differential equations, which we do in the next section. We note that the terms that makes our simple RG approach different

from the BCS mean-field theory, already solves two of the most important problems with the latter. These are the absence of selfenergy effects in the normal state and the absence of screening effects on the interaction. The importance of selfenergy effects, as described by Eq. (4.3), were already noticed in Section 3.5, while particle-hole screening is known to reduce the critical temperatures by more than a factor of two in the weakly interacting regime [137, 138]. These observations reveal the power of the RG approach, because with a rather straightforward derivation [30] of a simple set of coupled differential equations, we already go far beyond mean-field theory.

However, before we can apply Eqs. (4.2) and (4.3) to the critical Fermi mixture, we have to solve one remaining problem. Namely, as the inverse interaction vertex flows to zero, the chemical potentials in Eq. (4.3) are seen to diverge. To address this issue, we need to go beyond our initial approximation in deriving the RG equations, which can be achieved by taking also the frequency and momentum dependence of the interaction vertex into account. Although the two-body interaction in ultracold atomic gases is to a very good approximation constant in Fourier space, the renormalization group transformation still generates momentum and frequency dependence of the interaction vertex due to many-body effects. More specifically, both the ladder and the bubble diagram that renormalize the two-body interaction are momentum and frequency dependent. The ladder diagram depends on the external center-of-mass coordinates $\mathbf{q}$ and ω_p and its contribution to the renormalization of $V^{-1}_{\mathbf{q},p}$ is given by

$$d\hbar\Xi(q^2, i\omega_p) = \int_{d\Lambda} \frac{d\mathbf{k}}{(2\pi)^3} \frac{1 - f_+(\mathbf{k}) - f_-(\mathbf{q}-\mathbf{k})}{i\hbar\omega_p - \epsilon_{\mathbf{k}} - \epsilon_{\mathbf{q}-\mathbf{k}} + 2\mu} \,, \tag{4.4}$$

where during integration both $\mathbf{k}$ and $\mathbf{q}-\mathbf{k}$ have to remain in the shell at wavevector Λ of infinitesimal width $d\Lambda$. Since the ladder diagram is already present in the two-body limit, it is most important for two-body scattering properties. For this reason, the interaction vertex is mainly dependent on the center-of-mass coordinates, so in first instance we neglect the dependence of the vertex on other frequencies and momenta. We will return to the validity of this approximation later. The way to treat the external frequency and momentum dependence in the Wilsonian approach is to introduce new couplings by expanding the (inverse) interaction in the following way: $V^{-1}_{\mathbf{q},m} = V^{-1}_{\mathbf{0},0} - Z_q^{-1} q^2 + Z_\omega^{-1} i\hbar\omega_p$. The flow equations for the additional coupling constants Z_q^{-1} and Z_ω^{-1} are then approximated by

$$dZ_q^{-1} = \left. \frac{\partial d\hbar\Xi(q^2,\omega)}{\partial q^2} \right|_{q=\omega=0} \tag{4.5}$$

and

$$dZ_\omega^{-1} = - \left. \frac{\partial d\hbar\Xi(q^2,\omega)}{\partial \hbar\omega} \right|_{q=\omega=0} . \tag{4.6}$$

4.3 Extreme imbalance

First, we apply the RG to one spin-down particle in a Fermi sea of spin-up particles at zero temperature in the unitarity limit. The full equation of state for the normal state of a strongly interacting Fermi mixture was obtained at zero temperature using Monte-Carlo techniques [106]. It was discussed in Section 3.5. For large imbalances, the dominant feature in this equation of state is the selfenergy of the spin-down atoms in the sea of spin-up particles [106, 117]. We can also calculate this selfenergy with our renormalization group approach, where we consider the extremely imbalanced limit, which means that we only have one spin-down particle. The equations are now simplified, because $f_-(\Lambda)$ can be set to zero and thus μ_+ is not renormalized. Next, we have to incorporate the momentum and frequency dependence of the interaction in the one-loop Feynman diagram for the renormalization of μ_-. In this particular case, the external frequency dependence of the ladder diagram can be conveniently taken into account up to all orders. It is namely possible to show with the use of contour integration that the one-loop Matsubara sum in the diagram of Fig. 4.1(a), simply leads to the substitution $i\hbar\omega_p \to \epsilon_{\mathbf{q}} - \mu_+$ in Eq. (4.4) [117]. This substitution was also already encountered in Eq. (3.17). If we then account for the external momentum dependence through the coupling Z_q^{-1}, we obtain

$$\frac{dV_{\mathbf{0},0}^{-1}}{d\Lambda} = \frac{\Lambda^2}{2\pi^2}\left(\frac{1-f_+(\Lambda)}{2\epsilon_\Lambda - \mu_-} - \frac{f_+(\Lambda)}{2h}\right) , \tag{4.7}$$

$$\frac{d\mu_-}{d\Lambda} = \frac{\Lambda^2}{2\pi^2}\frac{f_+(\Lambda)}{-V_{\mathbf{0},0}^{-1} + Z_q^{-1}\Lambda^2} , \tag{4.8}$$

$$\frac{dZ_q^{-1}}{d\Lambda} = -\frac{\hbar^4\Lambda^4}{6\pi^2 m^2}\frac{1-f_+(\Lambda)}{(2\epsilon_\Lambda - \mu_-)^3} . \tag{4.9}$$

Note that these equations only have poles for positive values of μ_-. Since this will not occur, we can integrate out all momentum shells by substituting $\Lambda(l) = \Lambda_0 e^{-l}$ and $d\Lambda = \Lambda_0 e^{-l} dl$. The differential $d\Lambda$ has acquired an additional minus sign here, because Eqs. (4.7), (4.8) and (4.9) require a positive value for $d\Lambda$.

We then obtain a system of three coupled ordinary differential equations in l which are easily solved numerically. As an initial condition, we use $V_{\mathbf{0},0}^{-1}(0) = m(\pi - 2a\Lambda_0)/4\pi^2 a\hbar^2$ with a the s-wave scattering length. We encountered this expression already before in Eq. (1.2). There, it was seen to follow from Eq. (1.1) for the two-body transition matrix and the use of a high-momentum cut-off $\hbar\Lambda_0$. Our initial condition makes sure that we automatically incorporate the correct two-body transition matrix into our theory, namely, we obtain in the two-body limit that $V_{\mathbf{0},0}(\infty) = 4\pi a\hbar^2/m$ [136]. Moreover, the choice also ensures that at the end of the RG calculation no dependence on the arbitrary high-momentum cut-off $\hbar\Lambda_0$ remains. The unitarity limit is then given by $V_{\mathbf{0},0}^{-1}(0) = -m\Lambda_0/2\pi^2\hbar^2$. The other initial conditions are $\mu_-(0) = \mu_-$ and $Z_q^{-1}(0) = 0$, since the interaction starts out as being momentum independent. Note that in this calculation $\mu_-(0) = \mu_-$ is initially negative and increases during the flow

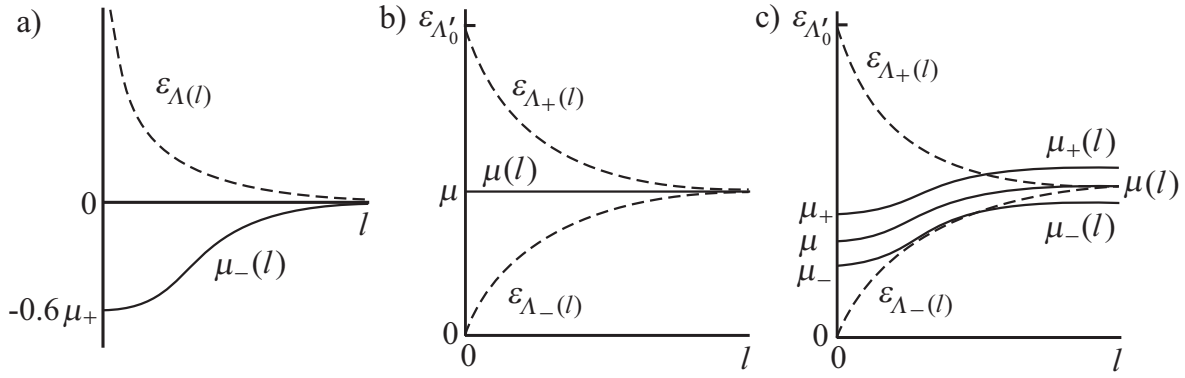

Figure 4.2: a) Position of the momentum shells (dashed lines) and flow of the chemical potentials (solid lines) for a) the strongly interacting extremely imbalanced case, b) the weakly interacting balanced case, and c) the strongly interacting imbalanced case.

due to the strong attractive interactions. The flow of the spin-down chemical potential $\mu_-(l)$ is depicted in Fig. 4.2(a). The quantum phase transition from a zero density to a nonzero density of spin-down particles occurs for the initial value μ_- that at the end of the flow precisely leads to $\mu_-(\infty) = 0$. This happens when $\mu_- = -0.52\mu_+$, which is therefore the selfenergy of a strongly interacting spin-down particle in a sea of spin-up particles [117]. Our value for the selfenergy is slightly less than the Monte-Carlo value of Lobo *et al.* [106], who find $\mu_- = -0.57\mu_+$. This is mainly because we somewhat overestimate the screening of the interaction. We come back to this point in the next section.

4.4 Phase diagram

Next, we determine the nonuniversal critical properties of the strongly interacting Fermi mixture at nonzero temperatures, and in particular the location of the tricritical point in the homogeneous phase diagram. Since it is only correct in the extremely imbalanced limit at zero temperature to make the substitution $\hbar\omega \to \epsilon_{\mathbf{q}} - \mu_{-\sigma}$ in Eq. (4.4), we now take the frequency dependence of the ladder diagram into account through the renormalization of the coupling Z_ω^{-1}. We still use Eq. (4.2) for the flow of $V_{\mathbf{0},0}^{-1}$, but the expressions for the flow of μ_σ and Z_ω^{-1} become

$$\frac{d\mu_\sigma}{d\Lambda} = \frac{\Lambda^2}{2\pi^2} \frac{f_{-\sigma}(\Lambda) + f_{\mathrm{B}}(\Lambda)}{-V_{\mathbf{0},0}^{-1} + Z_q^{-1}\Lambda^2 - Z_\omega^{-1}(\epsilon_\Lambda - \mu_{-\sigma})} , \tag{4.10}$$

$$\frac{dZ_\omega^{-1}}{d\Lambda} = \frac{\Lambda^2}{2\pi^2} \frac{1 - f_+(\Lambda) - f_-(\Lambda)}{4(\epsilon_\Lambda - \mu)^2} , \tag{4.11}$$

with $f_{\mathrm{B}}(\Lambda) = 1/\{\exp[\beta Z_\omega(-V_{\mathbf{0},0}^{-1} + Z_q^{-1}\Lambda^2)] - 1\}$ coming from the bosonic frequency dependence of the interaction. The flow equation for Z_q^{-1} can be obtained analytically

from Eq. (4.5), but is too cumbersome to write down explicitly. The initial conditions are the same as for the extremely imbalanced case with in addition $\mu_\uparrow(0) = \mu_\uparrow$ and $Z_\omega^{-1}(0) = 0$. As explained before, the critical condition is the Thouless criterion that the fully renormalized vertex $V_{\mathbf{0},0}^{-1}(\infty)$ goes to zero. From Eq. (4.10), we see that incorporating the coupling constants Z_q^{-1} and Z_ω^{-1}, and thereby taking the dependence of the interaction on the center-of-mass momentum and frequency into account, is crucial to solve the previously mentioned problem of the diverging chemical potential.

The only pole left in our set of RG equations is the average Fermi level $\mu = (\mu_+ + \mu_-)/2$, which is therefore the natural end point of our RG. However, this Fermi level is shifting due to the renormalization of the individual chemical potentials. The resulting problem is conveniently solved by integrating out all momentum shells with the following procedure. First, we start at a high momentum cutoff $\hbar\Lambda_0$ and flow to a momentum $\hbar\Lambda_0'$ at roughly two times the average Fermi momentum, where the individual Fermi momenta are given by $\hbar k_{\mathrm{F}\sigma} = \sqrt{2m\epsilon_{\mathrm{F}\sigma}}$. This integrates out the high-energy two-body physics, but hardly affects the chemical potentials. Then, we start integrating out the rest of the momentum shells symmetrically with respect to the flowing average Fermi level. This is achieved by using

$$\Lambda_+(l) = \left(\Lambda_0' - \sqrt{\frac{2m\mu}{\hbar^2}}\right) e^{-l} + \sqrt{\frac{2m\mu(l)}{\hbar^2}} \tag{4.12}$$

and by

$$\Lambda_-(l) = -\sqrt{\frac{2m\mu}{\hbar^2}} e^{-l} + \sqrt{\frac{2m\mu(l)}{\hbar^2}}. \tag{4.13}$$

Note that, as desired, we have that $\Lambda_+(l)$ starts at Λ_0' and automatically flows from above to $\sqrt{2m\mu(\infty)}/\hbar$, whereas $\Lambda_-(l)$ starts at 0 and automatically flows from below to $\sqrt{2m\mu(\infty)}/\hbar$. By substituting $\Lambda_+(l)$, $\Lambda_-(l)$ and their derivatives in Eqs. (4.2), (4.5), (4.10) and (4.11) we obtain a set of coupled differential equations in l that can be solved numerically. There is one remaining issue with this procedure, namely that $\Lambda_\pm(l)$ are in general not exactly symmetric with respect to the shifting average Fermi level. This unfortunately leads to a numerical problem with Eq. (4.11), which contains a true pole. We may solve this issue by explicitly symmetrizing the right-hand side of Eq. (4.11) with respect to the average Fermi level. As a result, the divergent part in Eq. (4.11) is by construction cancelled close to the pole. This procedure can be seen as a generalization of the determination of a principal value to the case of a shifting pole.

We first apply the above procedure to study the equal density case, i.e. $h \to 0$, as a function of the negative scattering length a. The scattering length enters the calculation through the initial condition of $V_{\mathbf{0},0}^{-1}$. To be able to express our results in terms of the Fermi energy $\epsilon_{\mathrm{F}} = \epsilon_{\mathrm{F}\sigma}$, we calculate the densities of the atoms in two different ways. The first way is with a direct flow equation for the density, namely

$dn_\sigma/d\Lambda = \Lambda^2 f_\sigma(\Lambda)/2\pi^2$ [136], while in the second way we use

$$n_\sigma = \int \frac{d\mathbf{k}}{(2\pi)^3} \frac{1}{e^{\beta(\epsilon_\mathbf{k} - \mu_\sigma(\infty))} + 1}. \tag{4.14}$$

The two procedures are not exactly the same, because the chemical potential is flowing. The first approach has the disadvantage that formally speaking the density is not a so-called one-particle irreducible quantity and therefore is less suitable to determine with a RG flow. On a more practical level, the two approaches are rather similar, so that we will apply and compare them both. In the weak-coupling limit, $a \to 0^-$, the chemical potentials hardly renormalize, so that only Eq. (4.2) is relevant. The critical temperature becomes exponentially small, which allows us to integrate Eq. (4.2) exactly with the result $k_\mathrm{B} T_\mathrm{c} = 8\epsilon_\mathrm{F} e^{\gamma - 3} \exp\{-\pi/2k_\mathrm{F}|a|\}/\pi$ and γ Euler's constant. Compared to the standard BCS-result we have an extra factor of $1/e$, coming from the screening effect of the bubble diagram that is not present in BCS theory. It is to be compared with the so-called Gor'kov correction [137], which is known to reduce the critical temperature by a factor of 2.2 in the weak-coupling BCS-limit [138]. The difference with our present result is that we have only allowed for a nonzero center-of-mass momentum, whereas to get precisely the Gor'kov correction we would also need to include the relative momentum. We see that due to our approximation of neglecting the relative momenta in the bubble diagram, we overestimate the screening effect on the critical temperature by 20%. Note that in the previous section, we also already concluded that screening effects are slightly overestimated by our RG.

At larger values of $|a|$, the flow of the chemical potential becomes important and we obtain higher critical temperatures. In the unitarity limit, when a diverges, we obtain with the direct flow equation for the density that $T_\mathrm{c} = 0.13 T_\mathrm{F}$ and $\mu(T_\mathrm{c}) = 0.55\epsilon_\mathrm{F}$, while the use of Eq. (4.14) leads to $T_\mathrm{c} = 0.12 T_\mathrm{F}$ and $\mu(T_\mathrm{c}) = 0.51\epsilon_\mathrm{F}$. Both results compare rather well with the Monte-Carlo results $T_\mathrm{c} = 0.152(7) T_\mathrm{F}$ and $\mu(T_\mathrm{c}) = 0.493(14)\epsilon_\mathrm{F}$ [120]. This is certainly true if we note that we also expect to obtain a critical temperature that is about 20% too low. Upon performing more elaborate RG calculations, i.e. taking more flowing couplings into account, we also obtained that $T_\mathrm{c} = 0.15 T_\mathrm{F}$. However, to some extent this latter agreement with the Monte-Carlo result is accidental, because the error bars on the RG procedure are not zero. Namely, each additional coupling that we consider slightly changes our results, while also different choices for $\Lambda_\pm(l)$ have a quantitative effect. Therefore, we considered various additional couplings and also looked at reasonable variations of Eqs. (4.12) and (4.13). However, our results always remained within about 30% of the result by Burovski *et al.* [120].

Keeping this in mind, we are in the unique position with our renormalization group approach to calculate the critical temperature as a function of polarization p and compare with the recent experiment of Shin *et al.* [87]. The result is shown in Fig. 4.3, where the particle densities were determined using their direct flow equations. The inset of this figure shows the one-loop diagram determining the position of the tricritical point. If it changes sign, then the fourth-order coefficient in the Landau theory for

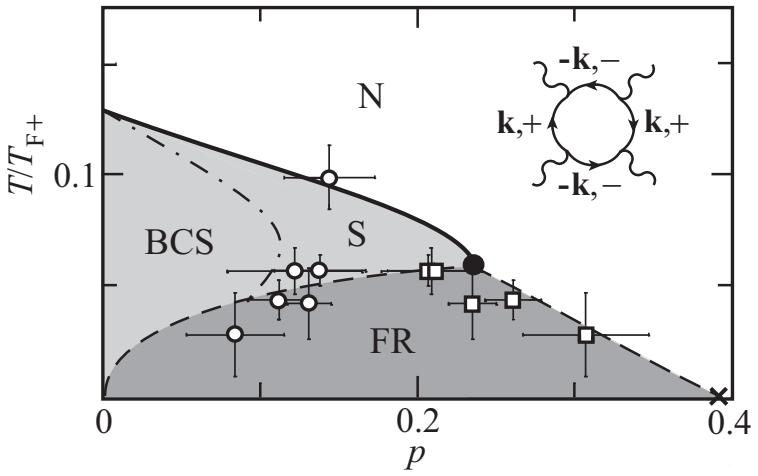

Figure 4.3: The phase diagram of the homogeneous two-component Fermi mixture in the unitarity limit, containing the superfluid Sarma (S) and BCS phases, the normal phase (N) and a forbidden region (FR). The solid black line is the result of our RG calculations, where particle densities have been obtained from their flow equation. The Monte-Carlo result of Lobo *et al.* [106] at zero temperature is indicated by a cross. The open circles and squares are data along the phase boundaries from the experiment of Shin *et al.* [87]. The dashed and dashed-dotted lines are only guides to the eye. Also shown is the one-loop Feynman diagram for the flowing Landau coefficient that determines the tricritical point.

the superfluid phase transition changes sign and the nature of the phase transition changes from second order to first order. This was explained more elaborately in Paragraph 3.2.2, where the right-hand side of Eq. (3.8) is actually the mathematical expression for the Feynman diagram in Fig. 4.3. In the RG calculation, we then keep the integration over internal momenta confined to the infinitesimal shell that is integrated out. Moreover, we have that during the RG flow the chemical potentials are renormalizing, so that selfenergy corrections to the Feynman diagram are also automatically taken into account. Ultimately, we then obtain $P_{c3} = 0.24$ and $T_{c3} = 0.06$ T_{F+} for the tricritical point. If we would have used Eq. (4.14) for the densities, we would have obtained $P_{c3} = 0.14$ and $T_{c3} = 0.06$ T_{F+}. Both match the experimental data, whose error bars are still quite large. For an even more precise comparison between theory and experiment, a larger amount of experimental data and results from Monte-Carlo calculations would be welcome. Also shown in the phase diagram is the prediction that the quantum phase transition from the equal-density superfluid to the polarized normal phase takes place at a critical imbalance of $p = 0.38$, as was discussed in Paragraph 3.5.2 [106, 118].

Near the second-order phase boundary, the BCS order parameter $|\langle\Delta\rangle|$ becomes arbitrarily small. Since at nonzero polarization we have that $h(\infty) > 0$, it immediately follows that $h(\infty) > |\langle\Delta\rangle|$. This means that the normal gas is unstable towards the so-called Sarma phase [60]. However, the present RG is not suitable to calculate the full

extent of the Sarma phase in the phase diagram or the precise shape of the forbidden region, because this requires a RG for the superfluid phase. Such a calculation could in principle be performed by first applying a Hubbard-Stratonovich transformation to the microscopic fermionic action in order to bring the superfluid pairing field and its pair fluctuations exactly into the theory [30]. By integrating out the fermions exactly, we would get a bosonic action that contains an infinite series of terms in the pair fluctuations [30]. The resulting quadratic term can be treated exactly, and for the spin-balanced mixture in the normal phase it leads to the so-called Nozières-Schmitt-Rink (NSR) approximation [116]. This approximation has a nice physical interpretation, since it can be seen as taking into account the ideal gas of noncondensed Cooper pairs. The exact treatment of quadratic pair fluctuations can also be achieved in the superfluid phase, where it gives good agreement with experiments [79, 125]. The fourth-order term of the obtained bosonic action, which describes the interaction between the noncondensed pairs in the normal state, is not so large and repulsive, as is required for the formation of a stable BEC. Effectively, we have thus mapped the strongly interacting fermionic problem onto a rather weakly interacting bosonic problem. We found that taking the pair interaction effects into account with an RG approach results in a decrease of the NSR critical temperature, which brings it closer to the Monte-Carlo value. It would be nice to extend this procedure to the superfluid phase, but here the calculation gets very cumbersome. Already the Gaussian-fluctuation calculation in itself is numerically tedious for the superfluid phase, and it would be just the starting point for the RG. Especially the determination of the higher-order terms for the fluctuations in the superfluid bosonic action is a very cumbersome task.

To conclude the discussion, we would like to emphasize that the power of the Wilsonian RG presented in this chapter is rather impressive when we realize that so far no analytical theory has been able to yield a value for the tricritical point that fits on the scale of Fig. 4.3. Moreover, Monte-Carlo calculations, which are numerically very involved, have up to now been restricted to zero temperature or to the balanced case. However, our present calculations also find good agreement with the experiments of Shin *et al.* at nonzero temperatures and polarizations.

Chapter 5

The strongly interacting ^{6}Li-^{40}K mixture

We consider a strongly interacting ^{6}Li-^{40}K mixture, which is imbalanced both in the masses and the densities of the two fermionic species.[1] At present, it is the experimentalist's favorite for reaching the superfluid regime in a mass-imbalanced mixture. We construct an effective thermodynamic potential that leads to excellent agreement with Monte-Carlo results for the normal state. We use it to determine the universal phase diagram of the mixture in the unitarity limit, where we find, in contrast to the mass-balanced case, the presence of a Lifshitz point. This point is characterized by the effective mass of the Cooper pairs becoming negative, which signals an instability towards a supersolid phase.

5.1 Introduction

Ultracold atomic Fermi mixtures are presently at the center of attention of both experimental and theoretical physicists. In Chapter 1 we discussed how the amazing experimental control over this system has led to many fundamental discoveries, while many more are likely to follow soon. These discoveries started with reaching the so-called BEC regime where the balanced two-component Fermi mixture turns superfluid due to the Bose-Einstein condensation (BEC) of molecules [139, 140]. By using a Feshbach resonance to vary the interaction strength between the atoms in the two different spin states, the smooth BEC-BCS crossover between a BEC of molecules and a BCS superfluid of Cooper pairs could be directly observed [28]. Since pairing is optimal for an equal amount of particles in each spin state and is absent for the noninteracting fully polarized system, a phase transition occurs as a function of spin imbalance [24, 25]. In Chapter 3 we found that the phase diagram in the unitarity limit is governed by a

[1] This chapter is directly based on K. B. Gubbels, J. E. Baarsma, and H. T. C. Stoof, *Lifshitz Point in the Phase Diagram of Resonantly Interacting ^{6}Li-^{40}K Mixtures*, Phys. Rev. Lett. **103**, 195301 (2009).

tricritical point. This resulted in the observation of phase separation [25, 87]. The presence of gapless Sarma superfluidity is also likely to be present in this system [60, 107], but has not been unambiguously identified yet.

Most recently, experiments have indicated that the physical consequences of yet another parameter can be explored, namely that of the mass imbalance between the two fermionic components. A very promising mixture in this respect consists of ^{6}Li and ^{40}K, which has a mass ratio of 6.7. Several accessible Feshbach resonances are identified in the mixture [64, 66], while both species have also been simultaneously cooled into the degenerate regime [65]. So far, experimental interest has focused on the BEC side of the Feshbach resonance, where molecules are formed. Although the mass imbalance itself does not lead to fundamental new physics here, this situation changes when the heteronuclear molecules are optically pumped to their ground state [51]. Then the molecules acquire a large electric dipole moment, which gives rise to anisotropic long-ranged interactions. In an optical lattice, this can lead to supersolid phases [52].

In this chapter we focus on a different regime, namely the unitarity limit, where the s-wave scattering length of the interspecies interaction diverges. Here, the size of the Cooper pairs is comparable to the average interparticle distance and the pairing is a many-body effect. The mass imbalance has a profound effect on the pairing now, because it affects the fermionic single-particle energies and the corresponding Fermi energies. We show that for the sufficiently large mass ratio of the ^{6}Li-^{40}K mixture, the phase diagram not only encompasses all the exciting physics known from the mass-balanced case, but is even much richer. Similar to the solely spin-imbalanced case is the presence of phase separation [63], which can occur due to the mismatch of the Fermi surfaces. Also similar is that gapless Sarma superfluidity is unstable at zero temperature [63], while there is a predicted crossover to the Sarma phase at nonzero temperatures [60]. However, the most exciting difference that we find is the presence of a Lifshitz point in the phase diagram.

At a Lifshitz point the transition to the superfluid phase undergoes a dramatic change of character. Rather than preferring a homogeneous order parameter, the system now becomes an inhomogeneous superfluid. This exotic possibility was early investigated for the weakly interacting mass-balanced case by Larkin and Ovchinnikov (LO), who considered a superfluid with a single standing-wave order parameter [67]. As mentioned in Chapter 1, this is energetically more favorable than the plane-wave case studied by Fulde and Ferrell (FF) [70]. Since the LO phase results in periodic modulations of the particle densities, it is a supersolid [69]. The FF and LO phases have intrigued the physics community for many decades, but so far remained elusive in experiments with atomic Fermi mixtures. Typically, Lifshitz points are predicted at weak interactions where the critical temperatures are very low. However, in this chapter we show that the very special phase diagram of the ^{6}Li-^{40}K mixture contains both a Lifshitz and a tricritical point in the unitarity limit, as shown in Fig. 5.1. This is in sharp contrast to the mass-balanced case, where at unitarity a large body of theory only finds a tricritical point, in agreement with experiments [87].

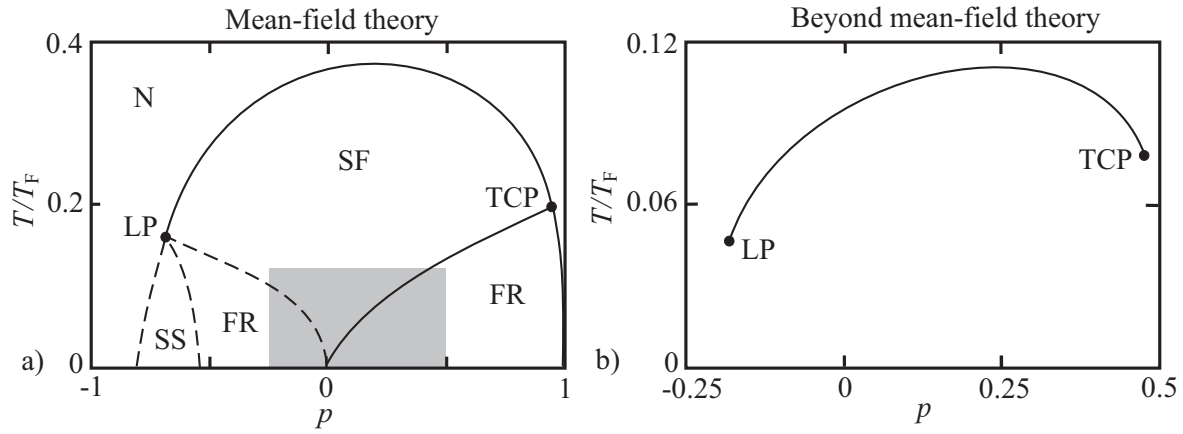

Figure 5.1: Universal phase diagram for the homogeneous ^{6}Li-^{40}K mixture in the unitarity limit as a function of temperature T and polarization p. The temperature is scaled with the reduced Fermi temperature $k_B T_F = \epsilon_F = \hbar^2(3\pi^2 n)^{2/3}/2m$, where m is twice the reduced mass and n is the total particle density. The result of mean-field theory is shown in panel (a). For a majority of light ^{6}Li atoms there is a tricritical point (TCP), at which the normal state (N), the homogeneous superfluid state (SF), and the forbidden region (FR) meet each other. For a majority of heavy ^{40}K atoms there is a Lifshitz point (LP), where there is an instability towards supersolidity (SS). The size of the supersolid stability region is not calculated within our theory and the dashed lines are therefore only guides to the eye. The grey area sets the scale for panel (b), where fluctuation effects are taken into account to calculate the location of the Lifshitz and the tricritical point more accurately.

In first instance, all these expectations follow from mean-field theory, which is useful for a qualitative description of the physics. However, it cannot be trusted quantitatively in the unitary regime, since it vastly overestimates critical temperatures in that case. It is thus important to understand how much these are lowered by fluctuation effects. In the mass-balanced case two effects are dominant, namely the fermionic selfenergies and the screening of the interaction due to particle-hole fluctuations [141]. Taking these into account gives in an intuitive manner results that compare well with Monte Carlo calculations [120] and experiment [87]. We find that an extension of this procedure to the ^{6}Li-^{40}K mixture leads to a reduction of the mean-field critical temperatures by an experimentally relevant factor of 3. This makes it more difficult, but not impossible, to reach the superfluid regime. Moreover, the presence of the Lifshitz point in the phase diagram is unaffected by the fluctuations, allowing for an experimental study of supersolidity in the ^{6}Li-^{40}K mixture.

5.2 Phase diagram

The critical properties of the superfluid transition in a fermionic mixture are determined by the effective Landau theory for the superfluid order parameter $\Delta(\mathbf{x})$, also called the BCS gap parameter. Although we consider no external potential, the order parameter

may still vary in space due to a spontaneous breaking of translational symmetry. Close to the superfluid transition, where the gap is small, we may expand the exact effective thermodynamic potential as

$$\Omega[\Delta] = \int d\mathbf{x} \left\{ \gamma_{\mathrm{L}} |\nabla\Delta|^2 + \alpha_{\mathrm{L}} |\Delta|^2 + \frac{\beta_{\mathrm{L}}}{2} |\Delta|^4 + ... \right\}, \tag{5.1}$$

where the challenge is to express the expansion parameters in terms of the temperature T and the atomic chemical potentials $\mu_\pm$. The upper (lower) sign refers to the light ^{6}Li (heavy ^{40}K) atoms. A phase transition has occurred when the global minimum of Ω is located at a nonzero order parameter $\langle\Delta(\mathbf{x})\rangle$, which describes a condensate of pairs. When $\gamma_{\mathrm{L}}(T)$ is positive, the pairs have a positive effective mass and their center-of-mass state of lowest energy is at zero momentum. Then, we can consider a homogeneous pairing field Δ, for which a second-order transition occurs at a critical temperature T_{c} when $\alpha_{\mathrm{L}}(T_{\mathrm{c}}) = 0$. The latter was explained in Section 3.2.

The critical condition of zero α_{L} assumes that the minimum for small values of $\langle\Delta\rangle$ is global, which is not necessarily the case. The expansion of Ω may contain higher powers of $|\Delta|^2$ that have negative coefficients, leading to a first-order transition with a jump in the order parameter when $\Omega[0] = \Omega[\langle\Delta\rangle]$. As explained in Paragraph 3.2.2, second-order behavior turns into first-order behavior when $\beta_{\mathrm{L}}(T)$ becomes negative, so that the temperature T_{c3} at the tricritical point (TCP) is determined by $\alpha_{\mathrm{L}}(T_{\mathrm{c3}}) = 0$ and $\beta_{\mathrm{L}}(T_{\mathrm{c3}}) = 0$. Another intriguing possibility is that not $\beta_{\mathrm{L}}(T)$, but rather $\gamma_{\mathrm{L}}(T)$ goes to zero. This leads to a Lifshitz point (LP), which is thus determined by $\alpha_{\mathrm{L}}(T_{\mathrm{L}}) = 0$ and $\gamma_{\mathrm{L}}(T_{\mathrm{L}}) = 0$. Since the effective mass of the Cooper pairs becomes negative below the Lifshitz point, it is energetically favorable for them to have kinetic energy and form a superfluid at nonzero momentum. This can be established in many ways, namely through a standing wave [67] or a more complicated superposition of plane waves [142, 143]. Due to the variety of possibilities it is hard to predict which lattice structure is most favorable. However, the fact that they all emerge from the Lifhitz point facilitates the experimental search for supersolidity in the ^{6}Li-^{40}K mixture. Moreover, a nonzero gap parameter gives rise to a sizeable superfluid fraction, showing that the LO-like incommensurate supersolid is very different from the commensurate supersolid studied in ^{4}He.

We continue our discussion at the mean-field level, which is useful for further explaining the relevant physics. Starting point is the BCS thermodynamic potential density for the ^{6}Li-^{40}K mixture with masses m_σ, where $\sigma = \pm$ denotes the fermionic species. From a direct generalization of Eq. (3.1) to the mass-imbalanced case, we find [63]

$$\begin{aligned} \omega_{\mathrm{BCS}}[\Delta; T, \mu_\sigma] = \int \frac{d\mathbf{k}}{(2\pi)^3} \Big\{ & \epsilon_{\mathbf{k}} - \mu - \hbar\omega_{\mathbf{k}} + \frac{|\Delta|^2}{2\epsilon_{\mathbf{k}}} \\ & - k_{\mathrm{B}} T \sum_{\sigma=\pm} \ln\left(1 + e^{-\hbar\omega_{\mathbf{k},\sigma}/k_{\mathrm{B}}T}\right) \Big\}, \end{aligned} \tag{5.2}$$

where we introduced the average chemical potential $\mu = (\mu_+ + \mu_-)/2$, half the difference $h = (\mu_+ - \mu_-)/2$, and the reduced kinetic energy $\epsilon_{\mathbf{k}} = \hbar^2\mathbf{k}^2/2m$ with $m = 2m_+m_-/(m_+ + m_-)$. The Bogoliubov quasiparticle dispersions become $\hbar\omega_{\mathbf{k},\sigma} = \hbar\omega_{\mathbf{k}} - \sigma(2h - \epsilon_{\mathbf{k},+} + \epsilon_{\mathbf{k},-})/2$ with $\hbar\omega_{\mathbf{k}} = \sqrt{(\epsilon_{\mathbf{k}} - \mu)^2 + |\Delta|^2}$ and $\epsilon_{\mathbf{k},\sigma} = \hbar^2\mathbf{k}^2/2m_\sigma$. We can now apply the exact critical conditions to ω_{BCS} and obtain the mean-field phase diagram. Although the BCS potential neglects fluctuations in the order parameter, it is expected that fluctuation effects only result in quantitative corrections. This expectation stems from the strongly interacting experiments for the mass-balanced case, for which the mean-field diagram is topologically correct [87]. The coefficients determining the second-order phase transition and the tricritical point are readily calculated as $\alpha_{\mathrm{L}} = \partial\omega_{\mathrm{BCS}}[0; T, \mu_\sigma]/\partial|\Delta|^2$ and $\beta_{\mathrm{L}} = \partial^2\omega_{\mathrm{BCS}}[0; T, \mu_\sigma]/(\partial|\Delta|^2)^2$. The results are shown in the phase diagram of Fig. 5.1(a). The polarization is defined as $p = (n_+ - n_-)/(n_+ + n_-)$, while the particle densities are determined by $n_\sigma = -\partial\omega_{\mathrm{BCS}}[\langle\Delta\rangle; T, \mu_\sigma]/\partial\mu_\sigma$. Therefore, the polarization is discontinuous simultaneously with the order parameter, which gives rise to a forbidden region (FR) below the tricritical point.

From Fig. 5.1(a), we see that the mean-field phase diagram also contains a Lifshitz point. It is calculated from the noninteracting Green's function for the Cooper pairs $G_\Delta(\mathbf{k}, i\omega_n)$, which is derived from the fermionic microscopic action by performing a Hubbard-Stratonovich transformation to the pairing field and integrating out the fermions exactly [30]. In the normal state, this propagator is given by $\hbar G_\Delta^{-1}(\mathbf{k}, i\omega_n) = 1/T^{2B} - \hbar\Xi(\mathbf{k}, i\omega_n)$, where $T^{2\mathrm{B}} = 4\pi a\hbar^2/m$ with a the diverging scattering length, while $\hbar\Xi$ represents the so-called ladder diagram. We encountered the differential form of the ladder diagram already in Eq. (4.4), while for the mass-imbalanced case it becomes

$$\hbar\Xi(\mathbf{k}, i\omega_n) = \int \frac{d\mathbf{k}'}{(2\pi)^3} \left\{ \frac{1}{2\epsilon_{\mathbf{k}'}} + \frac{1 - f_+(\mathbf{k}') - f_-(\mathbf{k} - \mathbf{k}')}{i\hbar\omega_n - \epsilon_{\mathbf{k}',+} - \epsilon_{\mathbf{k}-\mathbf{k}',-} + 2\mu} \right\} \tag{5.3}$$

with $f_\sigma(\mathbf{k}) = 1/(e^{(\epsilon_{\mathbf{k},\sigma} - \mu_\sigma)/k_{\mathrm{B}}T} + 1)$ the Fermi distributions. Note that the mean-field expression for α_{L} is equal to $-\hbar G_\Delta^{-1}(\mathbf{0}, 0)$, while we have that $\gamma_{\mathrm{L}} = -\partial\hbar G_\Delta^{-1}(\mathbf{0}, 0)/\partial\mathbf{k}^2 = 0$ at the Lifshitz point. What precisely happens below the Lifshitz point is an intriguing question for further research. In Fig. 5.1(a), we have sketched a simple scenario, where there is a second-order transition from the normal to the supersolid phase, for which the condition is $G_\Delta^{-1}(\mathbf{k}_{\mathrm{SS}}, 0) = 0$ with $\mathbf{k}_{\mathrm{SS}}$ the wavevector of the supersolid. However, this transition can in principle be of first order, where the realized supersolid periodicity can also contain more than one wavevector [143]. Moreover, the transition from supersolidity to the homogeneous superfluid phase is also expected to be of first order. The calculation for the stability regions of all possible supersolid lattices is beyond the scope of this thesis, so that the dashed lines in Fig. 5.1(a) are merely guides to the eye.

5.3 Strong interactions

Having established that within mean-field theory a tricritical point dominates the phase diagram when there is an abundance of light ^{6}Li atoms, while a Lifshitz points is present

when there is an abundance of heavy ^{40}K atoms, the question arises whether this interesting physics remains when we take fluctuation effects into account. Answering this question also leads to more quantitative predictions for future experiments. The normal equation of state at unitarity is known to be strongly affected by fluctuations [115]. Since this equation of state exactly follows from the fermionic selfenergies, we first try to take these accurately into account. We achieve this through a simple construction that gives excellent agreement with Monte Carlo results, and for which we only need to know the selfenergy $\hbar\Sigma_\sigma$ of a single σ atom in a sea of $-\sigma$ atoms. We found in Section 3.5 that at zero temperature, the latter is given by $\hbar\Sigma_\sigma = -c_\sigma\mu_{-\sigma}$. The coefficients can be calculated within the ladder approximation of Paragraph 5.3 [117], giving $c_+ = 2.2$ and $c_- = 0.44$, or with the renormalization-group approach of Section 4.3 [141], giving $c_+ = 2.0$ and $c_- = 0.34$, while Monte Carlo calculations lead to $c_+ = 2.3$ and $c_- = 0.36$ [144]. Noting that these approaches agree rather well, we use the Monte Carlo results for the rest of the calculation, since they effectively incorporate all Feynman diagrams. Moreover, $\hbar\Sigma_{-\sigma} = 0$ because the majority atoms are unaffected by the single minority atom. The chemical potential of the minority particle is then given by $\mu_\sigma = \hbar\Sigma_\sigma$.

Next, we define renormalized chemical potentials as in Paragraph , namely

$$\mu'_\sigma = \mu_\sigma + \frac{c_\sigma \mu'^2_{-\sigma}}{\mu'_\sigma + \mu'_{-\sigma}}. \tag{5.4}$$

Two important solutions to these equations are such that the chemical potential of one species $(-\sigma)$ is not renormalized, $\mu'_{-\sigma} = \mu_{-\sigma}$, while the renormalized chemical potential of the other species is zero, i.e., $\mu'_\sigma = \mu_\sigma + c_\sigma\mu_{-\sigma} = 0$. These two solutions correspond precisely to the two extremely imbalanced limits. By using the renormalized chemical potentials in the mean-field thermodynamic potential, we can calculate the full normal equation of state by using the equation for the densities $n_\sigma = -\partial\omega_{\mathrm{BCS}}[0; T, \mu'_\sigma]/\partial\mu_\sigma$. The comparison with the Monte Carlo equation of state is shown in Fig. 5.2 and the agreement is excellent. We also show the comparison for the mass-balanced case, where the ladder calculation gives $c_\pm = 0.61$ in good agreement with the result from Monte-Carlo calculations. The agreement in Fig. 5.2 shows that our construction captures the full thermodynamics of the strongly interacting normal state without any free parameters. Since we do not expect the coefficients $c_\pm$ to depend strongly on temperature, we can also use our method at low temperatures. Moreover, it is easily extended to other mass ratios and to the superfluid state [107].

The above discussion shows that we effectively account for all fluctuations in the normal state. However, there is a second effect of particle-hole fluctuations which affects the superfluid state. Namely, the change in the coefficient α due to screening of the interspecies interaction, also known as the Gor'kov correction [137]. We account for this screening by replacing the two-body transition matrix T^{2B} with an effective transition matrix that includes the so-called bubble sum. We thus have that $1/T^{\mathrm{eff}} =$

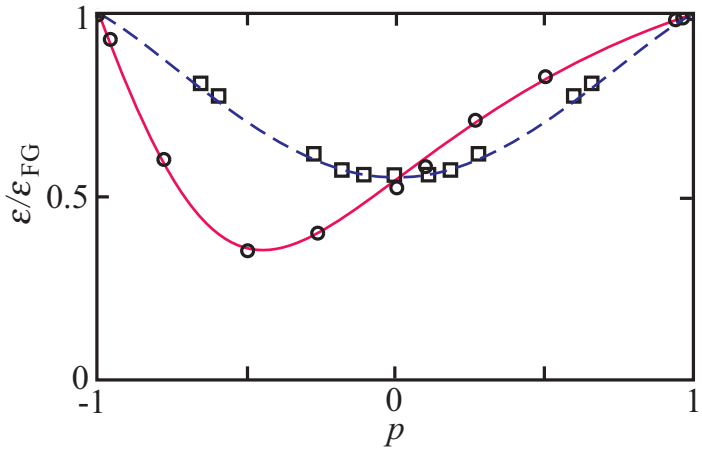

Figure 5.2: Equations of state for the zero-temperature normal state of the ^{6}Li-^{40}K mixture (full line) and the mass-balanced mixture (dashed line) in the unitarity limit. The Monte Carlo results for the ^{6}Li-^{40}K mixture by Gezerlis *et al.* [144] are shown by circles, while the Monte Carlo results for the mass-balanced mixture by Lobo *et al.* [106] are shown by squares. The energy density ϵ is scaled with the ideal gas result $\epsilon_{\rm FG} = 3(\epsilon_{\rm F+}n_+ + \epsilon_{\rm F-}n_-)/5$ with $\epsilon_{{\rm F}\sigma} = \hbar^2(6\pi^2 n_\sigma)^{2/3}/2m_\sigma$. The deviations from one thus show the strong interaction effects.

$1/T^{\rm 2B} - \hbar\Pi(\mathbf{0},0)$, where the bubble diagram is given by [30]

$$\hbar\Pi(\mathbf{0},0) \;=\; \int \frac{d\mathbf{k}'}{(2\pi)^3}\frac{f_+(\mathbf{k}') - f_-(\mathbf{k}')}{2h' - \epsilon_{\mathbf{k}',+} + \epsilon_{\mathbf{k}',-}}. \tag{5.5}$$

The bubble diagram is graphically represented on the right in Fig. 4.1. Since now $\alpha_{\rm L} = -\hbar G_\Delta^{-1}(\mathbf{0},0) = -1/T^{\rm eff} + \hbar\Xi(\mathbf{0},0)$, the equation for the critical temperature, $\alpha_{\rm L} = 0$, becomes $-\hbar\Xi(\mathbf{0},0) = \hbar\Pi(\mathbf{0},0)$, where we use renormalized chemical potentials to include the selfenergy effects. If we apply this procedure to the mass and population-balanced case we find $T_{\rm c} = 0.18T_{\rm F}$ and $\mu(T_{\rm c}) = 0.52\epsilon_{\rm F}$, which is to be compared with the Monte Carlo results $T_{\rm c} = 0.15T_{\rm F}$ and $\mu(T_c) = 0.49\epsilon_{\rm F}$ [120]. Moreover, we find for the mass-balanced tricritical point that $k_{\rm B}T_{\rm c3} = 0.09\epsilon_{\rm F+}$ and $P_{\rm c3} = 0.25$, which agrees with the experimental data [87]. Returning to the ^{6}Li-^{40}K mixture and using the same conditions for the tricritical point and the Lifshitz point as before, we find the result in Fig. 5.1(b). Note that the critical temperatures are lowered by about a factor of three due to the screening and the selfenergy effects. Also the locations of the Lifshitz point and the tricritical point have drastically changed, since now we find $T_{\rm c3} = 0.08T_{\rm F}$ and $P_{\rm c3} = 0.47$, while $T_{\rm L} = 0.05T_{\rm F}$ and $P_{\rm L} = -0.18$.

To conclude, in this chapter we have considered the experimentally available ^{6}Li-^{40}K mixture at unitarity, where we incorporated selfenergy effects to reproduce the normal equation of state from Monte-Carlo calculations. By also including the effect of screening on the critical temperature, we believe to have achieved quantitative predictions for the phase diagram, which is exciting since it contains both a Lifshitz

and a tricritical point. At weaker attractive interactions the Lifshitz point remains present, although its temperature gets exponentially suppressed. Below the Lifshitz point, various supersolid phases are competitive [142, 143] and a rich phase structure is expected.

Chapter 6

Josephson oscillations near a p-wave resonance

Molecules near a p-wave resonance have a large probability Z to be in the closed channel or bare molecular state responsible for the Feshbach resonance.[1] In the superfluid state this allows for observation of Rabi or Josephson oscillations between the molecular and atomic components of the Bose-Einstein condensed pairs, which contains a characteristic signature of the quantum phase transition that occurs as a function of applied magnetic field.

6.1 Introduction

The continuous excitement in the field of ultracold atoms is to a large extent caused by the ever increasing experimental control over the creation and manipulation of degenerate quantum gases. Arguably the most important example of such control is the use of Feshbach resonances with which the interaction between the atoms can be manipulated by simply varying the magnetic field. The s-wave Feshbach resonance occurs when atoms collide with zero orbital angular momentum ($\ell = 0$) and is experimentally most easily accessible. As mentioned in Chapter 1, it has been widely used in the study of degenerate Fermi gases, especially for the crossover between a Bardeen-Cooper-Schrieffer (BCS) superfluid and a Bose-Einstein condensate (BEC) of diatomic molecules [9, 14, 15, 16, 17, 18]. A novel challenge is to obtain superfluidity also with pairs in nonzero orbital angular momentum states by using p-wave ($\ell = 1$), or maybe even d-wave ($\ell = 2$) Feshbach resonances. The observation of p-wave resonances has been achieved in Fermi gases of ^{40}K [145], ^{6}Li atoms [146] and ^{6}Li-^{40}K mixtures

[1] This chapter is directly based on K. B. Gubbels and H. T. C. Stoof, *Theory for p-Wave Feshbach Molecules*, Phys. Rev. Lett. **99**, 190406 (2007).

[64]. In particular, Gaebler *et al.* have been able to create and detect p-wave Feshbach molecules in a gas of ^{40}K with lifetimes on the order of milliseconds on both the BEC and the BCS side of the resonance [46]. The lifetime on the BEC side, where the energy of the Feshbach molecule lies below the open-channel continuum, is presumably limited by collisional losses, whereas the lifetime on the BCS side is determined by the decay of the molecular state into the open-channel continuum. However, upon entering the superfluid regime on the BCS side, the Bose-Einstein condensed pairs are stabilized by the presence of a Fermi sea [79]. Now that their dominant decay mechanism is absent, the lifetime of the pairs on the BCS side is expected to be enhanced, giving some hope that stable p-wave superfluidity might be within reach.

There are many exciting aspects about p-wave superfluidity. First of all, a p-wave superfluid has a more complex order parameter than a s-wave superfluid, due to the various possible projections of its angular momentum (m_ℓ=0,±1), which can give rise to anisotropic superfluids. Second, a p-wave superfluid undergoes various classical and quantum phase transitions as a function of temperature and magnetic field [49, 84, 147, 148, 149, 150]. As an example, the evolution from the BEC to the BCS side of the Feshbach resonance at zero temperature contains a topological quantum phase transition [48], rather than the crossover known from the s-wave case. Third, the p-wave resonances are intrinsically narrow. As a result, the two-channel nature of the Feshbach resonance becomes very prominent. This can be quantified as follows. The superfluid phase near a Feshbach resonance arises from the Bose-Einstein condensation of pairs or so-called dressed molecules [57], which are characterized by the linear superposition $|\psi_{\rm dr}\rangle = \sqrt{Z}|\psi_{\rm m}\rangle + \sqrt{1-Z}|\psi_{\rm aa}\rangle$, where $|\psi_{\rm m}\rangle$ is the wave function of the bare molecular state in the closed channel, and $|\psi_{\rm aa}\rangle$ describes the atom pairs in the open channel. In the case of a s-wave resonance, the magnitude of the probability Z can be estimated at resonance (unitarity) by $Z \simeq 2\sqrt{2\Delta}/\pi\eta$ [79], where Δ is the universal BCS gap parameter at unitarity and η^2 is a measure for the energy width of the resonance. The latter was introduced in Section 2.2. For the extremely broad s-wave resonance of ^{6}Li at 834 G, this leads at a Fermi energy of $\epsilon_{\rm F} = 380$ nK to $Z \simeq 4 \cdot 10^{-5}$. For the s-wave resonance of ^{40}K at 202 G, we obtain at the same Fermi energy $Z \simeq 5 \cdot 10^{-3}$, which is much larger but still a rather small number. However, we have shown in Section 2.3 that for a p-wave resonance the value of Z at unitarity can become as large as 0.7. Next, we show that the two-channel nature of the p-wave dressed molecules allows for a study of coherent Rabi or Josephson oscillations that occur between the closed and open channel components of the Bose-Einstein condensed pairs.

6.2 Phase fluctuations

Having obtained the analytic solution to the two-body p-wave Feshbach problem in Section 2.3, we now incorporate this two-body physics into the many-body physics. To this end, we use the following effective grand-canonical Hamiltonian with chemical

potential $\mu_{\rm a}$ for the atoms and $\mu_{\rm m}$ for the molecules,

$$\begin{aligned}\hat{H} &= \sum_{\mathbf{k}}(\epsilon_{\mathbf{k}}-\mu_{\rm a})\hat{a}^\dagger_{\mathbf{k}}\hat{a}_{\mathbf{k}}+\sum_{\mathbf{k}}\left(\frac{\epsilon_{\mathbf{k}}}{2}+\delta^{\rm B}_{m_\ell}-\mu_{\rm m}\right)\hat{b}^\dagger_{m_\ell,\mathbf{k}}\hat{b}_{m_\ell,\mathbf{k}}\\ &\quad+\frac{1}{\sqrt{\mathcal{V}}}\sum_{\mathbf{p},\mathbf{k}}\left(g_{m_\ell}(\mathbf{k})\hat{b}^\dagger_{m_\ell,\mathbf{p}}\hat{a}_{\mathbf{p}/2+\mathbf{k}}\hat{a}_{\mathbf{p}/2-\mathbf{k}}+\text{h.c.}\right),\end{aligned} \tag{6.1}$$

where $\hat{a}^\dagger_{\mathbf{k}}$ creates an atom with momentum $\mathbf{k}$, $\hat{b}^\dagger_{m_\ell,\mathbf{k}}$ creates a bare p-wave molecule with angular momentum projection m_ℓ and momentum $\mathbf{k}$, and $\mathcal{V}$ is the volume of the gas. The rest of the notation was introduced in Section 2.3. This Hamiltonian is valid when different values of m_ℓ lead to resonances at well-separated magnetic fields B_{m_ℓ}, as is experimentally the case for the $m_\ell=0$ resonance of ^{40}K [46]. If this is not true, then on the right-hand side of Eq. (6.1) we also have to perform a sum over m_ℓ. Furthermore, in equilibrium we have that $\mu_{\rm m}=2\mu_{\rm a}$, but for reasons that become clear shortly, we enforce this relation only at the end of the calculations. For p-wave resonances the total scattering length satisfies $a^3=a^{\rm bg\,3}_{m_\ell}-mg_{m_\ell}(\mathbf{0})^2/6\pi\hbar^2\delta_{m_\ell}$. If we parametrize this in analogy with the s-wave case as $a^3=a^{\rm bg\,3}_{m_\ell}[1-\Delta B_{m_\ell}/(B-B_{m_\ell})]$, we see that the atom-molecule coupling obeys $g_{m_\ell}(\mathbf{0})=\hbar(6\pi\Delta\mu\Delta B_{m_\ell}a^{\rm bg\,3}_{m_\ell}/m)^{1/2}$, with ΔB_{m_ℓ} the magnetic-field width of the Feshbach resonance. Near resonance the background interaction may be safely neglected in the Hamiltonian, except for its effect on the atom-molecule coupling $g_{m_\ell}(\mathbf{k})$. As we have seen in Section 2.3, the background interaction induces a momentum dependence in the atom-molecule coupling $g_{m_\ell}(\mathbf{k})$, which is crucial in obtaining accurate answers for the molecular selfenergy of Eq. (2.26), the wavefunction renormalization Z, and the bound-state energy of the dressed molecules. The use of this dressed coupling is then also the reason why we call the Hamiltonian of Eq. (6.1) effective.

In order to discuss internal Josephson oscillations [47, 151], we turn to the functional-integral formalism [57] in which the creation and annihilation operators become complex fields that not only depend on momentum, but also on time t. First, we derive an effective action $S_{\rm eff}$ for the atomic and molecular phase fluctuations $\theta_{\rm a}(t)$ and $\theta_{\rm m}(t)$, which is given by

$$\int d[\theta_{\rm a}]d[\theta_{\rm m}]e^{iS_{\rm eff}[\theta_{\rm a},\theta_{\rm m}]/\hbar}=\int d[a^*]d[a]d[b^*]d[b]e^{iS[a^*,a,b^*_{m_\ell},b_{m_\ell}]/\hbar} \tag{6.2}$$

with the action S in real time given by

$$\begin{aligned}&S[a^*,a,b^*_{m_\ell},b_{m_\ell}]=\\ &\int dt\left\{\sum_{\mathbf{k}}i\hbar\left[a^*_{\mathbf{k}}(t)\frac{\partial}{\partial t}a_{\mathbf{k}}(t)+b^*_{m_\ell,\mathbf{k}}(t)\frac{\partial}{\partial t}b_{m_\ell,\mathbf{k}}(t)\right]-H[a^*,a,b^*_{m_\ell},b_{m_\ell}]\right\}.\end{aligned} \tag{6.3}$$

A sketch of the derivation then goes as follows. We start by rewriting the atomic and molecular fields as $a_{\mathbf{k}}(t)\to a_{\mathbf{k}}(t)e^{i\theta_{\rm a}(t)}$, $b_{m_\ell,\mathbf{k}}(t)\to b_{m_\ell,\mathbf{k}}(t)e^{i\theta_{\rm m}(t)}$ to explicitly consider

the atomic and molecular phase fluctuations $\theta_{\rm a}(t)$ and $\theta_{\rm m}(t)$. By substituting these expressions in the action S, it changes in the following way: $g_{m_\ell}(\mathbf{k}) \to g_{m_\ell}(\mathbf{k}) e^{i[2\theta_{\rm a}(t)-\theta_{\rm m}(t)]}$ and $\mu_j \to \mu_j - \hbar\dot{\theta}_j(t)$, where the last substitution is due to the time-derivatives in the action and the index j runs over two possible subscripts, namely atomic and molecular. After expanding the resulting expression in the phase fluctuations, we separate the action into the part $S_{\rm ph}$ containing the fluctuations, and the part S that does not contain them. The latter has exactly the same form as the action we started from. Now we are in the position to do perturbation theory in the phase fluctuations by expanding the part of the exponential in Eq. (6.2) that contains $S_{\rm ph}$. Expanding in the fluctuations up to second order, we see that the coefficients in front of the phase fluctuations get averaged over the original action S. For example, the term linear in $\dot{\theta}_{\rm m}(t)$ becomes ultimately $\int dt\, \dot{\theta}_{\rm m}(t) \sum_{\mathbf{k}} \langle b^*_{m_\ell,\mathbf{k}}(t) b_{m_\ell,\mathbf{k}}(t)\rangle$, where the average $\sum_{\mathbf{k}} \langle b^*_{m_\ell,\mathbf{k}}(t) b_{m_\ell,\mathbf{k}}(t)\rangle$ equals the total number of bare molecules and is conveniently expressed as $-\partial\Omega(\mu_{\rm a},\mu_{\rm m})/\partial\mu_{\rm m}$ with $\Omega(\mu_{\rm a},\mu_{\rm m})$ the thermodynamic potential of the gas. By re-exponentiating all terms up to quadratic order, we obtain finally the effective action for the phase fluctuations,

$$\begin{aligned} S^{\rm eff}[\theta_j] \;=\; & \int dt \Bigg\{ \sum_j \hbar\dot{\theta}_j \frac{\partial\Omega}{\partial\mu_j} - \sum_{j,j'} \frac{\hbar^2}{2} \dot{\theta}_j \dot{\theta}_{j'} \frac{\partial^2\Omega}{\partial\mu_j \partial\mu_{j'}} \\ & + J\cos(2\theta_{\rm a} - \theta_{\rm m}) \Bigg\}. \end{aligned} \tag{6.4}$$

We only have a nonzero Josephson coupling in the presence of a molecular condensate, in which case it is given by

$$J = \frac{2}{\sqrt{\mathcal{V}}} \sum_{\mathbf{k}} g_{m_\ell}(\mathbf{k}) \langle b^*_{m_\ell,\mathbf{0}}(t) a_{\mathbf{k}}(t) a_{-\mathbf{k}}(t)\rangle. \tag{6.5}$$

6.3 Internal Josephson oscillations

In deriving the quadratic action for the phase fluctuations we made one approximation, namely a gradient expansion of the fluctuations that takes into account static number correlations. To calculate the coefficients in Eq. (6.4) we make another approximation, namely mean-field theory. The mean-field thermodynamic potential for a superfluid Fermi gas near a two-channel p-wave resonance at zero temperature can be directly derived from the Hamiltonian in Eq. (6.1). To this end, we apply the Bogoliubov substitution to the molecular operator at zero momentum, namely $\hat{b}^\dagger_{m_\ell,\mathbf{0}} \to \sqrt{n_{\rm mc}\mathcal{V}}$, where $n_{\rm mc} = |\langle \hat{b}_{m_\ell,\mathbf{0}}\rangle|^2/\mathcal{V}$ is the bare molecular condensate density. The effect of molecules in nonzero momentum states is not considered. After diagonalization of the resulting quadratic expression for the fermions, we obtain for the thermodynamic

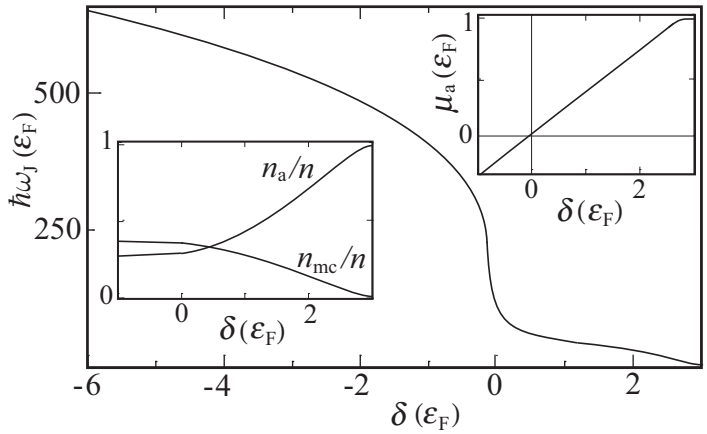

Figure 6.1: Josephson frequency ω_J as a function of the detuning δ. Energies are expressed in terms of the Fermi energy $\epsilon_F = \hbar^2(6\pi^2 n)^{2/3}/2m$, with $n = 2n_{mc} + n_a$ the total density of atoms, which is kept fixed during the calculation at $n = 3 \times 10^{18}$ m^{-3}, so that $\epsilon_F/\hbar \simeq 2\pi \times 4$ kHz. In the left inset, the number of bare molecules n_{mc} and open-channel atoms n_a are given as a function of the detuning. In the right inset we have the atomic chemical potential vs. detuning.

potential at zero temperature

$$\begin{aligned}\Omega &= \frac{1}{2}\sum_{\mathbf{k}}\left\{\epsilon_{\mathbf{k}} - \mu_a - \hbar\omega_{\mathbf{k}} + \frac{2|g_{m_\ell}(\mathbf{k})|^2 n_{mc}}{\epsilon_{\mathbf{k}}}\right\} \\ &\quad + (\delta_{m_\ell} - \mu_m) n_{mc}\mathcal{V}, \end{aligned} \tag{6.6}$$

with $\hbar\omega_{\mathbf{k}} = \sqrt{(\epsilon_{\mathbf{k}} - \mu_a)^2 + 4|g_{m_\ell}(\mathbf{k})|^2 n_{mc}}$. Note that in Eq. (6.6) we have eliminated the bare detuning in favor of the renormalized detuning with the procedure explained in Section 2.3. The generalized gap equation then follows from differentiation with respect to n_{mc}, yielding

$$\delta_{m_\ell} - \mu_m = \frac{1}{\mathcal{V}}\sum_{\mathbf{k}} |g_{m_\ell}(\mathbf{k})|^2 \left(\frac{1}{\hbar\omega_{\mathbf{k}}} - \frac{1}{\epsilon_{\mathbf{k}}}\right), \tag{6.7}$$

which can also be seen as the many-body generalization of the two-body bound state equation $E - \delta_{m_\ell} = \hbar\Sigma'_{m_\ell}(E)$ from Section 2.3 with $E = \mu_m$. Within mean-field theory, the coefficients in Eq. (6.4) are readily determined. For example, $-\partial\Omega/\partial\mu_m = n_{mc}\mathcal{V}$, where n_{mc} is obtained from the gap equation. Also, we have that $-\partial\Omega/\partial\mu_a = n_a\mathcal{V} = \sum_{\mathbf{k}}[1 - (\epsilon_{\mathbf{k}} - \mu_a)/\hbar\omega_{\mathbf{k}}]/2$, with n_a the atomic density. Even the second derivatives are given by simple analytic expressions in terms of momentum integrals. Finally, the Josephson coupling is given by $J = 2n_{mc}\sum_{\mathbf{k}} |g_{m_\ell}(\mathbf{k})|^2/\hbar\omega_{\mathbf{k}}$. These expressions all depend quantitatively on $a^{bg}_{m_\ell}$, showing that the background interaction is important.

From the effective action we can then derive the equations of motion by writing down the Euler-Lagrange equations. The remaining second-order differential equations

can be solved analytically, and give rise to two types of modes. One has frequency zero and is recognized as the Goldstone mode due to the spontaneous broken $U(1)$ symmetry associated with the conservation of the total number of atoms in the gas. The other mode has a nonzero frequency ω_{J} and is recognized as the collective mode corresponding to internal Josephson or Rabi oscillations between the molecular and the atomic components of the Bose-Einstein condensed pairs. In Fig. 6.1, we show the Josephson oscillation frequency, the atomic chemical potential, the atomic density and the bare molecular density as a function of the detuning with the parameters for the $m_\ell = 0$ Feshbach resonance of ^{40}K. These parameters were obtained in Section 2.3.

Far below resonance, not visible on the scale of the figure, we find that $\hbar\omega_{\mathrm{J}} \simeq \delta$. However, near resonance, where the detuning is no longer the dominant energy scale, we observe completely different behavior. In particular, on approach of the quantum critical point at $\mu_{\mathrm{a}} = 0$ [48], we find that the slope of the Josephson frequency develops a logarithmic divergency. Since internal Josephson oscillations can be accessed experimentally by performing a Ramsey-type experiment [73], this characteristic feature in the Josephson frequency is an observable signature for the occurrence of the quantum phase transition. Although the Josephson oscillations are damped by pair breaking, we expect this effect to be suppressed since the single-atom continuum is Pauli-blocked by the Fermi sea and the Bose-Einstein condensed pairs are protected by the (mostly) gapped atomic spectrum. Finally we note that the collective mode of Josephson oscillations is intrinsically connected to the two-channel nature of p-wave resonances and is absent in a single-channel treatment of the interactions.

Bibliography

[1] H. Kamerlingh Onnes, Akad. van Wetenschappen **14**, 113 (1911)
[2] J. Bardeen, L.N. Cooper, J.R. Schrieffer, Phys. Rev. **108**, 1175 (1957)
[3] A. Einstein, Sitzber. Kgl. Preuss. Akad. Wiss., 3 (1925)
[4] P. Kapitza, Nature **141**, 74 (1938)
[5] J.F. Allen, A.D. Misener, Nature **141**, 75 (1938)
[6] F. London, Nature **141**, 643 (1938)
[7] L.N. Cooper, Phys. Rev. **104**, 1189 (1956)
[8] H.T.C. Stoof *et al.*, Phys. Rev. Lett. **76**, 10 (1996)
[9] C.A. Regal, M. Greiner, D.S. Jin, Phys. Rev. Lett. **92**, 040403 (2004)
[10] D. Bailin, A. Love, Phys. Rept. **107**, 325 (1984)
[11] R. Casalbuoni, G. Nardulli, Rev. Mod. Phys. **76**, 263 (2004)
[12] D.M. Eagles, Phys. Rev. **186**, 456 (1969)
[13] A.J. Leggett, *Modern Trends in the Theory of Condensed Matter* (Springer, Berlin, 1980)
[14] M.W. Zwierlein *et al.*, Phys. Rev. Lett. **92**, 120403 (2004)
[15] J. Kinast *et al.*, Phys. Rev. Lett. **92**, 150402 (2004)
[16] M. Bartenstein *et al.*, Phys. Rev. Lett. **92**, 203201 (2004)
[17] T. Bourdel *et al.*, Phys. Rev. Lett. **93**, 050401 (2004)
[18] G.B. Partridge *et al.*, Phys. Rev. Lett. **95**, 020404 (2005)
[19] H. Feshbach, Ann. Phys. **5**, 357 (1958)
[20] W.C. Stwalley, Phys. Rev. Lett. **37**, 1628 (1976)
[21] E. Tiesinga, B.J. Verhaar, H.T.C. Stoof, Phys. Rev. A **47**, 4114 (1993)
[22] S. Inouye *et al.*, Nature **392**, 151 (1998)
[23] M.H. Anderson *et al.*, Science **269**, 198 (1995)
[24] M.W. Zwierlein *et al.*, Science **311**, 492 (2006)
[25] G.B. Partridge *et al.*, Science **311**, 503 (2006)
[26] P.F. Bedaque, H. Caldas, G. Rupak, Phys. Rev. Lett. **91**, 247002 (2003)
[27] J.G. Bednorz, K.A. Müller, Z. Phys. B **64**, 189 (1986)

[28] M. Inguscio, W. Ketterle, C. Salomon (eds.). *Ultra-cold Fermi Gases* (IOS Press, Amsterdam, 2008)
[29] I. Bloch, J. Dalibard, W. Zwerger, Rev. Mod. Phys. **80**, 885 (2008)
[30] H.T.C. Stoof, K.B. Gubbels, D.B.M. Dickerscheid, *Ultracold Quantum Fields* (Springer, Dordrecht, 2009)
[31] C.C. Bradley *et al.*, Phys. Rev. Lett. **75**, 1687 (1995)
[32] K.B. Davis *et al.*, Phys. Rev. Lett. **75**, 3969 (1995)
[33] J. Prodan *et al.*, Phys. Rev. Lett. **54**, 992 (1985)
[34] A.L. Migdall *et al.*, Phys. Rev. Lett. **54**, 2596 (1985)
[35] N. Masuhara *et al.*, Phys. Rev. Lett. **61**, 935 (1988)
[36] J. Billy *et al.*, Nature **453**, 891 (2008)
[37] P.S. Jessen *et al.*, Phys. Rev. Lett. **69**, 49 (1992)
[38] W.S. Bakr *et al.*, Nature **462**, 74 (2009)
[39] J. Hubbard, Proc. Roy. Soc. A **276**, 238 (1963)
[40] D. Jaksch *et al.*, Phys. Rev. Lett. **81**, 3108 (1998)
[41] M.P.A. Fisher *et al.*, Phys. Rev. B **40**, 546 (1989)
[42] M. Greiner *et al.*, Nature **415**, 39 (2002)
[43] A.O. Koetsier *et al.*, Phys. Rev. A **77**, 023623 (2008)
[44] Z. Hadzibabic *et al.*, Nature **441**, 1118 (2006)
[45] A.H. van Amerongen *et al.*, Phys. Rev. Lett. **100**, 090402 (2008)
[46] J.P. Gaebler *et al.*, Phys. Rev. Lett. **98**, 200403 (2007)
[47] A.J. Leggett, Rev. Mod. Phys. **47**, 331 (1975)
[48] N. Read, D. Green, Phys. Rev. B **61**, 10267 (2000)
[49] V. Gurarie, L. Radzihovsky, Ann. Phys. (N.Y.) **322**, 2 (2007)
[50] T. Lahaye *et al.*, Nature **448**, 672 (2007)
[51] K.K. Ni *et al.*, Science **322**, 231 (2008)
[52] K. Góral, L. Santos, M. Lewenstein, Phys. Rev. Lett. **88**, 170406 (2002)
[53] D. DeMille, Phys. Rev. Lett. **88**, 067901 (2002)
[54] R.A. Duine, A.H. MacDonald, Phys. Rev. Lett. **95**, 230403 (2005)
[55] G.B. Jo *et al.*, Science **325**, 1521 (2009)
[56] T. Busch *et al.*, Found. Phys. **28**, 549 (1998)
[57] R.A. Duine, H.T.C. Stoof, Phys. Rep. **396**, 115 (2004)
[58] T. Alm *et al.*, Nucl. Phys. A **551**, 45 (2003)
[59] G. Sarma, J. Phys. Chem. Solids **24**, 1029 (1963)
[60] K.B. Gubbels, M.W.J. Romans, H.T.C. Stoof, Phys. Rev. Lett. **97**, 210402 (2006)
[61] W.V. Liu, F. Wilczek, Phys. Rev. Lett. **90**, 047002 (2003)
[62] M.M. Forbes *et al.*, Phys. Rev. Lett. **94**, 017001 (2005)
[63] M.M. Parish *et al.*, Phys. Rev. Lett. **98**, 160402 (2007)
[64] E. Wille *et al.*, Phys. Rev. Lett. **100**, 053201 (2008)
[65] A.C. Voigt *et al.*, Phys. Rev. Lett. **102**, 020405 (2009)
[66] T.G. Tiecke *et al.*, arXiv:0908.2071
[67] A.I. Larkin, Y.N. Ovchinnikov, Sov. Phys. JETP **20**, 762 (1965)
[68] G.V. Chester, Phys. Rev. A **2**, 256 (1970)

[69] A. Bulgac, M.M. Forbes, Phys. Rev. Lett. **101**, 215301 (2008)
[70] P. Fulde, R.A. Ferrell, Phys. Rev. **135**, A550 (1964)
[71] E. Kim, M.H.W. Chan, Nature **427**, 225 (2004)
[72] S. Knoop *et al.*, Phys. Rev. Lett. **100**, 083002 (2008)
[73] E.A. Donley *et al.*, Nature **412**, 295 (2001)
[74] L.D. Landau, E.M. Lifshitz, *Quantum Mechanics, vol. 3* (Butterworth-Heinemann, Oxford, 1981)
[75] J.J. Sakurai, *Modern Quantum Mechanics* (Addison-Wesley, New York, 1994)
[76] B.H. Bransden, C.J. Joachain, *Quantum Mechanics* (Prentice Hall, New York, 2000)
[77] C. Chin *et al.*, arXiv:0812.1496
[78] G.M. Falco, H.T.C. Stoof, Phys. Rev. A **75**, 023612 (2007)
[79] M.W.J. Romans, H.T.C. Stoof, Phys. Rev. A **74**, 053618 (2006)
[80] G.M. Falco, H.T.C. Stoof, Phys. Rev. A **71**, 063614 (2005)
[81] M.W.J. Romans, H.T.C. Stoof, Phys. Rev. Lett. **95**, 260407 (2005)
[82] C. Ticknor *et al.*, Phys. Rev. A **69**, 042712 (2004)
[83] F. Chevy *et al.*, Phys. Rev. A **71**, 062710 (2005)
[84] C.H. Cheng, S.K. Yip, Phys. Rev. Lett. **95**, 070404 (2005)
[85] D.B.M. Dickerscheid *et al.*, Phys. Rev. A **71**, 043604 (2005)
[86] I.S. Gradshteyn, I.M. Ryzhik, *Table of Integrals, Series and Products* (Academic Press, London, 1963)
[87] Y. Shin *et al.*, Nature **451**, 689 (2008)
[88] D.E. Sheehy, L. Radzihovsky, Phys. Rev. Lett. **96**, 060401 (2006)
[89] J.Kinnunen, L.M. Jensen, P. Törmä, Phys. Rev. Lett. **96**, 110403 (2006)
[90] F. Chevy, Phys. Rev. Lett. **96**, 130401 (2006)
[91] P. Pieri, G.C. Strinati, Phys. Rev. Lett. **96**, 150404 (2006)
[92] W. Yi, L.M. Duan, Phys. Rev. A **73**, 031604(R) (2006)
[93] M. Haque, H.T.C. Stoof, Phys. Rev. A **74**, 011602 (2006)
[94] T.N. De Silva, E.J. Mueller, Phys. Rev. Lett. **97**, 070402 (2006)
[95] A. Imambekov *et al.*, Phys. Rev. A **74**, 053626 (2006)
[96] K. Machida, T. Mizushima, M. Ichioka, Phys. Rev. Lett. **97**, 120407 (2006)
[97] J.P. Martikainen, Phys. Rev. A **74**, 013602 (2006)
[98] C.C. Chien *et al.*, Phys. Rev. Lett. **97**, 090402 (2006)
[99] M.M. Parish *et al.*, Nat. Phys. **3**, 124 (2007)
[100] A. Bulgac, M.M. Forbes, Phys. Rev. A **75**, 031605 (2007)
[101] B. Van Schaeybroeck, A. Lazarides, Phys. Rev. Lett. **98**, 170402 (2007)
[102] M.W. Zwierlein *et al.*, Nature **442**, 54 (2006)
[103] M. Haque, H.T.C. Stoof, Phys. Rev. Lett. **98**, 260406 (2007)
[104] Y. Shin *et al.*, Phys. Rev. Lett. **97**, 030401 (2006)
[105] G.B. Partridge *et al.*, Phys. Rev. Lett. **97**, 190407 (2006)
[106] C. Lobo *et al.*, Phys. Rev. Lett. **97**, 200403 (2006)
[107] J.M. Diederix, K.B. Gubbels, H.T.C. Stoof, arXiv:0907.0127
[108] M.M. Parish, D.A. Huse, arXiv:0903.5324

[109] M. Houbiers *et al.*, Phys. Rev. A **56**, 4864 (1997)
[110] T.L. Ho, Phys. Rev. Lett. **92**, 090402 (2004)
[111] R. Combescot, C. Mora, Europhys. Lett. **68**, 79 (2004)
[112] B.M. Fregoso, G. Baym, Phys. Rev. A **73**, 043616 (2006)
[113] G.E. Astrakharchik *et al.*, Phys. Rev. Lett. **93**, 200404 (2004)
[114] J. Carlson, S. Reddy, Phys. Rev. Lett. **95**, 060401 (2005)
[115] C.A.R. Sá de Melo *et al.*, Phys. Rev. Lett. **71**, 3202 (1993)
[116] P. Nozières, S. Schmitt-Rink, J. Low Temp. Phys. **59**, 195 (1985)
[117] R. Combescot *et al.*, Phys. Rev. Lett. **98**, 180402 (2007)
[118] S. Pilati, S. Giorgini, Phys. Rev. Lett. **100**, 030401 (2008)
[119] N.V. Prokof'ev, B.V. Svistunov, Phys. Rev. B **77**, 125101 (2008)
[120] E. Burovski *et al.*, Phys. Rev. Lett. **96**, 160402 (2006)
[121] A. Recati, C. Lobo, S. Stringari, Phys. Rev. A **78**, 023633 (2008)
[122] J. Carlson *et al.*, Phys. Rev. Lett. **91**, 050401 (2003)
[123] R. Haussmann, Phys. Rev. B **49**, 12975 (1994)
[124] A. Perali *et al.*, Phys. Rev. Lett. **92**, 220404 (2004)
[125] H. Hu, P.D. Drummond, X.J. Liu, Nat. Phys. **3**, 469 (2007)
[126] Y. Nishida, D.T. Son, Phys. Rev. Lett. **97**, 050403 (2006)
[127] M.Y. Veillette, D.E. Sheehy, L. Radzihovsky, Phys. Rev. A **75**, 043614 (2007)
[128] P. Nikolić, S. Sachdev, Phys. Rev. A **75**, 033608 (2007)
[129] M.C. Birse *et al.*, Phys. Lett. B **605**, 287 (2005)
[130] S. Diehl *et al.*, Phys. Rev. A **76**, 021602(R) (2007)
[131] K.G. Wilson, J. Kogut, Phys. Rep. **12**, 75 (1974)
[132] K.G. Wilson, Phys. Rev. B **4**, 3174 (1971)
[133] R. Shankar, Rev. Mod. Phys. **66**, 129 (1994)
[134] C. Honerkamp, Phys. Rev. B **63**, 035109 (2001)
[135] P. Kopietz, T. Busche, Phys. Rev. B **64**, 155101 (2001)
[136] M. Bijlsma, H.T.C. Stoof, Phys. Rev. A **54**, 5085 (1996)
[137] L.P. Gor'kov, T.K. Melik-Barkhudarov, Sov. Phys. JETP **13**, 1018 (1961)
[138] H. Heiselberg *et al.*, Phys. Rev. Lett. **85**, 2418 (2000)
[139] M. Greiner, C.A. Regal, D.S. Jin, Nature **426**, 537 (2003)
[140] S. Jochim *et al.*, Science **302**, 2101 (2003)
[141] K.B. Gubbels, H.T.C. Stoof, Phys. Rev. Lett. **100**, 140407 (2008)
[142] N. Yoshida, S.K. Yip, Phys. Rev. A **75**, 063601 (2007)
[143] C. Mora, R. Combescot, Phys. Rev. B **71**, 214504 (2005)
[144] A. Gezerlis *et al.*, Phys. Rev. Lett. **103**, 060403 (2009)
[145] C.A. Regal *et al.*, Phys. Rev. Lett. **90**, 053201 (2003)
[146] J. Zhang *et al.*, Phys. Rev. A **70**, 030702(R) (2004)
[147] T.L. Ho, R.B. Diener, Phys. Rev. Lett. **94**, 090402 (2005)
[148] Y. Ohashi, Phys. Rev. Lett. **94**, 050403 (2005)
[149] V. Gurarie, L. Radzihovsky, A.V. Andreev, Phys. Rev. Lett. **94**, 230403 (2005)
[150] M. Iskin, C.A.R. Sá de Melo, Phys. Rev. Lett. **96**, 040402 (2006)
[151] V.M. Galitski, Phys. Rev. A **72**, 013612 (2005)

Samenvatting

Koud?!

'Koud?! Een atoomgas gekoeld met lasers, dat is pas koud!'. Door een ijle gaswolk van alkaliatomen te beschieten met een laser is het mogelijk om atomen vrijwel stil te zetten. Op deze manier koelt het gas af tot de micro-Kelvin-schaal: ultrakoud dus. Om te voorkomen dat de atomen wegvliegen gedurende het experiment, worden ze opgesloten in een val. Deze kan gemaakt worden met een inhomogeen magneetveld, wat door een atoom met een magnetisch dipoolmoment als een potentiaalput wordt ervaren. Door de diepte van de val te verminderen kunnen de heetste atomen wegvliegen, zodat het gas nog verder afkoelt. Hiermee zijn zelfs temperaturen op de nano-Kelvin-schaal gehaald, wat ultrakoude atoomgassen de koudste objecten in het waarneembare universum maakt.

Bose-Einstein-condensatie

Omdat koude atomen langzaam voortbewegen, is hun kwantummechanische golfgedrag prominent aanwezig. De gemiddelde De Broglie-golflengte van de atomen wordt gegeven door $\lambda = h/(mv)$ met h de constante van Planck, m de atoommassa en v hun gemiddelde snelheid. Deze snelheid schaalt in eerste instantie met de temperatuur als $T^{1/2}$. Als de temperatuur laag genoeg is, dan kan in het geval van bosonische atomen de golflengte zelfs groter worden dan de gemiddelde deeltjesafstand, zodat er een grote materiegolf ontstaat. In deze coherente golf zitten alle deeltjes in dezelfde kwantumtoestand en hebben ze dezelfde fase, zodat de golf gezien kan worden als het atomaire equivalent van een laser. De coherente materiegolf wordt een Bose-Einstein-condensaat (BEC) genoemd. In 1995 nam de groep van Cornell en Wieman voor het eerst een BEC waar in een ultrakoud gas van ^{87}Rb-atomen, terwijl de groep van Ketterle onder andere interferentie van gecondenseerde atoomwolken aantoonde. Hiermee verdienden de drie experimentatoren niet alleen een bloemetje, maar ook de Nobelprijs in 2001.

Na de successen met bosonische kwantumgassen ontstond al snel een hevige interesse in Fermi-gassen, bestaande uit atomen met halftallige spin. Fermionen gedragen zich heel anders dan bosonen: daar waar een boson graag zijn kwantumtoestand deelt met een mede-boson, is dit voor een fermion absoluut uitgesloten. Hierdoor kunnen

fermionen in eerste instantie geen BEC vormen. Echter, in 1956 liet Cooper al zien dat bij lage temperaturen de fermionen maar een klein beetje aantrekkende interactie nodig hebben om bosonische Cooper-paren te vormen. In het jaar daarop toonden Bardeen, Cooper en Schrieffer aan dat de zwak gebonden Cooper-paren ook kunnen Bose-Einstein-condenseren, wat BCS-theorie genoemd wordt. Deze gecondenseerde paren kunnen vervolgens getransporteerd worden zonder energieverlies.

Supervloeibaarheid

Bose-Einstein-condensaten leiden in vrijwel alle gevallen tot een wrijvingsloze toestand, die supervloeibaar wordt genoemd. In het geval van geladen deeltjes spreken we van supergeleiding. De afwezigheid van wrijving wordt begrepen door naar de laag-energetische excitaties van het gecondenseerde gas te kijken. Landau liet zien dat langzame objecten het condensaat niet kunnen exciteren, waardoor deze ook geen energie of impuls over kunnen dragen. Het Bose-Einstein-condensaat stroomt vervolgens wrijvingsloos langs deze objecten, alsof ze er niet waren. Supervloeibaarheid en supergeleiding zijn niet alleen zeer interessante macroscopische kwantumeffecten, ze zijn ook nog eens van groot praktisch belang. Zo wordt supervloeibaarheid gebruikt voor hoge-precisiemetingen, en supergeleiding om sterke magneetvelden op te wekken voor de LHC, MRI of Japanse zweeftreinen. Supergeleiding kan ook een belangrijke rol gaan spelen in toekomstige oplossingen voor ons energieprobleem. Het is dus erg belangrijk om deze toestand beter te begrijpen.

Feshbach resonanties

Hiervoor zijn experimenten met atoomgassen ideaal. Deze zijn namelijk een stuk eenvoudiger dan metalen, waar de fermionen door een roosterstructuur bewegen. De atoomgassen bevatten geen verontreinigingen en de fermionen kunnen als puntdeeltjes met puntinteracties worden beschouwd. Atoomgassen zijn ook extreem goed te manipuleren. Niet alleen hun temperatuur, maar ook de effectieve interactiesterkte tussen de fermionen kan met precisie gecontroleerd worden. Om dit te bewerkstelligen wordt een zogenoemde Feshbach-resonantie gebruikt. In een Feshbach-resonante botsing vormen twee atomen tijdelijk een molecuul met een andere spinconfiguratie dan de botsende atomen. De verschillende spinconfiguraties leiden tot een verschil in magnetische momenten, waardoor de energie van de gebonden moleculaire toestand veranderd kan worden ten opzichte van de atomen door middel van een aangelegd magneetveld. Aangezien de botsingseigenschappen van de atomen zeer gevoelig zijn voor de energie van de gebonden toestand, ontstaat nu een precieze controle over de effectieve interactiesterkte.

Bij ultralage temperaturen vinden voornamelijk laag-energetische botsingen zonder draai-impuls ($\ell = 0$) plaats. De bijbehorende golffunctie is symmetrisch in de plaatsruimte, waardoor deze interacties niet kunnen plaatsvinden tussen identieke fermionen in dezelfde spintoestand. Immers, als twee identieke fermionen omgewisseld worden, moet de totale golffunctie anti-symmetrisch zijn. Is de golffunctie symmetrisch in de

plaats, dan moet hij antisymmetrisch in de spinruimte zijn, waarvoor we minimaal twee spintoestanden nodig hebben. Cooper-paren ontstaan daarom meestal tussen deeltjes van verschillende spin.

Gepolariseerde Fermi-mengsels

In ultrakoude atoomgassen is het experimenteel mogelijk gebleken om de supervloeibare toestand nauwkeurig te onderzoeken als functie van de polarisatie, die gedefinieerd is als $P = (N_+ - N_-)/(N_+ + N_-)$ met N_σ het aantal atomen in hyperfijne spintoestand σ. Het ultrakoude ongepolariseerde mengsel ($P = 0$) is supervloeibaar voor aantrekkende interacties, terwijl in het volledig gepolariseerde gas ($P = 1$) geen Cooper-paarvorming plaatsvindt. De tussenliggende faseovergang is experimenteel bestudeerd met een gas van ^{6}Li-atomen. De atomen bevonden zich in de laagste twee hyperfijnniveaus van hun grondtoestand, waarbij het aantal deeltjes in deze twee toestanden gecontroleerd kon worden met nucleaire-spinomzettingen door microgolven. De experimenten werden gedaan bij resonante interacties tussen de deeltjes. Zulke gepolariseerde Fermi-mengsels met sterke wisselwerking zijn van fundamenteel belang. Ze komen bijvoorbeeld ook voor in de kernen van zware atomen (mengsel van protonen en neutronen), en in de kernen van neutronensterren (mengsel van quarks).

Kokend koud

We hebben het fasediagram uitgerekend voor het sterk-interagerende Fermi mengsel met een polarisatie. In zo'n diagram wordt gespecificeerd welke fase stabiel is als functie van de thermodynamische variabelen, zoals de temperatuur en de deeltjesaantallen. Het blijkt dat de faseovergang tussen de normale toestand en de supervloeibare toestand zowel op continue wijze als op discontinue wijze kan plaatsvinden. We hebben het fasediagram bepaald met behulp van BCS-theorie, en met renormalisatietechnieken. De eerste methode is alleen kwalitatief correct, terwijl de tweede methode ook tot kwantitatieve overeenstemming met experimenten leidt. Het blijkt bovendien dat er een bijzondere supervloeibare toestand op kan treden, die de Sarma toestand wordt genoemd. Deze fase is speciaal, omdat in de impulsruimte een deel van het systeem zich supervloeibaar gedraagt en een deel normaal. Dit wordt ook wel faseseparatie in de impulsruimte genoemd. De Sarma fase wordt instabiel voor hele lage temperaturen.

Op het zogenoemde trikritische punt verandert de overgang tussen de normale en de supervloeibare fase van continu naar discontinu. Beneden het trikritische punt zorgt de discontinue faseovergang voor sprongen in de ordeparameter, de dichtheden en de polarisatie. De polarisatie is laag in de supervloeibare fase en hoog in de normale fase. Als de polarisatie tussen deze twee extremen in ligt, vindt faseseparatie in de coördinaatruimte plaats. Dit betekent dat het systeem zich ruimtelijk zal scheiden in supervloeibare regionen en normale regionen. De eerste hebben een lagere polarisatie en een hogere dichtheid dan de tweede. Deze vorm van faseseparatie is een welbekend dagelijks fenomeen dat voorkomt bij de discontinue overgang van een vloeistof (zoals water) naar de gasfase. Echter, fasegesepareerde supervloeistoffen zijn veel zeldzamer.

We hebben berekend dat de atomaire supervloeistoffen gaan 'koken' bij temperaturen op de nano-Kelvin-schaal, een miljard keer lager dan kamertemperatuur. Deze supervloeistoffen zijn dus niet kokend heet, maar kokend ultrakoud.

Mengsels in de val

In de bovenstaande discussie hebben we stilzwijgend aangenomen dat het atoomgas opgesloten is in een homogene doos. Echter, dit is niet de experimentele realiteit. De experimentele vallen voor de atomen zijn namelijk harmonisch, zodat $V^{\mathrm{val}}(r) = m\omega^2 r^2/2$ met ω de frequentie van de val en r de afstand tot het centrum van de val. Als de potentiaal niet te steil is, dan mogen we het gas lokaal als homogeen beschouwen. We kunnen dan simpelweg de besproken homogene theorie gebruiken, maar met plaatsafhankelijke chemische potentialen, namelijk $\mu_\sigma(r) = \mu_\sigma - V^{\mathrm{val}}(r)$. Dit wordt de lokale-dichtsheidsbenadering genoemd. We vinden hiermee drie mogelijke configuraties van de gaswolk in de val. Als de kern van de gaswolk zich in de normale fase bevindt, dan zal het gas overal in de val normaal zijn. Daarnaast kan het gas supervloeibaar zijn in het centrum, wat twee verdere mogelijkheden oplevert. Ofwel het gas wordt normaal door een continue overgang als functie van positie in de val, of door een discontinue overgang. De drie verschillende configuraties van de atoomwolk zijn waargenomen in de experimenten met ^{6}Li.

Superkristal

Recentelijk zijn er ook ultrakoude Fermi-mengsels van ^{6}Li- en ^{40}K-atomen experimenteel beschikbaar gekomen, hoewel supervloeibaarheid nog niet is bereikt. Als beide atoomsoorten toegang hebben tot één enkele hyperfijntoestand, dan hebben we wederom een mengsel van twee fermionische componenten, die nu een verschillende massa hebben. We hebben het fasediagram van het ultrakoude ^{6}Li-^{40}K-gas bestudeerd voor resonante interacties. Als er een meerderheid van lichte lithiumatomen is, dan is er een trikritisch punt in het fasediagram. Maar als er een meerderheid van zware kaliumatomen is, dan blijkt dat de effectieve massa van de Cooper-paren negatief kan worden. Dit gebeurt op het zogenoemde Lifshitz-punt. Beneden het Lifshitz-punt wordt het energetisch gunstig voor de Cooper-paren om kinetische energie te hebben. Dit leidt tot ruimtelijke variaties in de ordeparameter, wat spontane breking van translatiesymmetrie oplevert. Als het Cooper-paarcondensaat periodiek gaat variëren in de ruimte, dan gaan de atomaire dichtheden ook variëren, waardoor er een kristalstructuur ontstaat. De combinatie van supervloeibaarheid met een kristalstructuur in de dichtheden leidt tot een zogenoemd superkristal. Er is veel interesse geweest in superkristallen (Engels: supersolids) de laatste jaren, maar het blijkt experimenteel erg lastig te zijn om deze nieuwe materietoestand onomstotelijk te bewijzen. Hopelijk gaan de experimenten met ultrakoude Fermi-mengsels daar verandering in brengen.

Josephson-oscillaties

Naast Feshbach-resonanties in botsingen zonder draai-impuls ($\ell = 0$), zijn er ook reso-

nanties waargenomen met $\ell = 1$ tot en met $\ell = 8$. In een volledig gepolariseerd Fermi gas komen botsingen met $\ell = 0$ niet voor, zodat de interacties met $\ell = 1$ dominant zijn. De bijbehorende Feshbach-moleculen zijn voor dit systeem experimenteel waargenomen in de normale fase. Onze theorie voor Feshbach-resonanties is in zeer goede overeenstemming met de metingen aan deze Feshbach-moleculen. Helaas is de levensduur van de moleculen vooralsnog te kort om experimenteel supervloeibaarheid te bereiken. Supervloeistoffen met draai-impuls zijn interessant, omdat ze een rijkere structuur hebben dan supervloeistoffen zonder draai-impuls, wat leidt tot allerlei nieuwe exotische kwantumeffecten. Aangezien Feshbach-moleculen bestaan uit een lineaire superpositie van kwantumtoestanden in twee kanalen met een verschillende spinconfiguratie, kunnen er Rabi-oscillaties tussen deze twee gekoppelde kanalen plaatsvinden. In het geval van een supervloeistof van Feshbach-moleculen worden dit coherente oscillaties tussen de gecondenseerde componenten in de twee kanalen, wat ook Josephson-oscillaties worden genoemd. Voor Feshbach-moleculen met $\ell = 1$ zien we opmerkelijk gedrag in de frequentie van de oscillaties, wat een experimenteel waarneembaar signaal oplevert voor een kwantumfaseovergang die optreedt in het systeem als functie van een aangelegd magneetveld.

Conclusie

Met ultrakoude atoomgassen kunnen fundamentele vragen over het gedrag van kwantummechanische veeldeeltjessystemen in groot detail bestudeerd worden. Dit komt vooral doordat atoomgassen ideale 'kwantumsimulatoren' zijn, wat betekent dat met deze gassen experimentele studies van een groot aantal verschillende Hamiltonianen uitgevoerd kunnen worden, variërend van zwak interagerend tot sterk interagerend, van eendimensionaal tot driedimensionaal, van homogene systemen tot periodieke systemen, waarbij de microscopische parameters van het atoomgas nauwkeurig bekend zijn en ook nog eens over een groot bereik aangepast kunnen worden. In dit proefschrift hebben we zowel een kwalitatief als een kwantitatief begrip verkregen van experimenten aan een sterk wisselwerkend fermionisch atoomgas als functie van de temperatuur en de polarisatie. Dit begrip is niet alleen van belang voor de atoomfysica, maar ook voor de fysica van de gecondenseerde materie, de kernfysica en de (astro)deeltjesfysica, waar ook gepolariseerde Fermi-mengsels met een sterke wisselwerking voorkomen. Daarnaast hebben we de verkregen kennis gegeneraliseerd naar een fermionisch atoommengsel van deeltjes met een verschillende massa, waarvoor een nieuwe generatie experimenten in opkomst is. Bovendien hebben we een volledig gepolariseerd Fermi-gas onderzocht, waarin de resonante wisselwerking aanleiding geeft tot botsingen met draai-impuls. In alle onderzochte gevallen hebben we exotische vormen van supervloeibaarheid gevonden, die afwijken van het conventionele gedrag van supergeleidende metalen. Hierdoor ontstaat een breder begrip van de wrijvingsloze toestand. Hopelijk draagt dit proefschrift bij aan nieuwe experimenten met ultrakoude atoomgassen, waarmee de exotische vormen van supervloeibare materie nader kunnen worden onderzocht.

Dankwoord

Opeens heb je het, je wordt promovendus. Vier jaar lang onderzoek doen naar datgene waarover de mensheid altijd al meer heeft willen weten: het kwantummechanische gedrag van fermionische atoommengsels bij ultralage temperaturen. Promoveren is leuk, heel leuk zelfs, vooral als het goed gaat. Je hebt veel creatieve vrijheid en de intellectuele uitdaging is altijd aanwezig. Natuurlijk zit het ook wel eens tegen. Er zijn van die dagen dat je sterk de neiging hebt om de titel van je proefschrift te wijzigen in: "Wetenschappelijk Onderzoek als Vorm van Zelfkastijding: een Persoonlijk Relaas". Gelukkig kwamen deze dagen gedurende mijn promotie maar weinig voor.

Hoofdverantwoordelijke voor mijn toptijd als promovendus is mijn begeleider, Henk Stoof. Henk, vrijwel alles wat ik weet over koude atomen en de rest van de theoretische natuurkunde heb ik van jou geleerd. Voor mijn gevoel liep onze samenwerking vanaf dag één op goed gesmeerde rolletjes. Je grenzeloze enthousiasme voor alles wat met fysica te maken heeft werkt uiterst motiverend; je directe betrokkenheid bij alles wat je promovendi dagelijks uitspoken is meer dan bewonderenswaardig. Ik zal mijn leven lang met veel plezier terugkijken op de afgelopen vier jaar en daar ben ik je ongelooflijk dankbaar voor.

Daarnaast heb ik erg plezierig samengewerkt met mijn overige collega's in de Kwantumvloeistoffengroep. Dit heeft zowel tot directe als tot indirecte bijdragen aan dit proefschrift geleid. Ten eerste wil ik Dennis Dickerscheid, Mathijs Romans, Jildou Baarsma en Jeroen Diederix bedanken voor het gezamenlijk doen van onderzoek en het schrijven van artikelen die al dan niet in dit proefschrift opgenomen zijn. Ook bedank ik de rest van de groep, met name Arnaud Koetsier, die vlak voor mij zijn queeste begon, Michiel Snoek en Jasper van Heugten. Rembert Duine ben ik dankbaar voor menig leuk en nuttig gesprek over wetenschap en wielrennen. Marius de Leeuw is ruim drie jaar lang mijn zeer prettige kamergenoot geweest. Aangezien ons onderzoek niks met elkaar te maken had, gingen onze dagelijkse gesprekken over andere wezenlijke zaken, zoals de voetbalwedstrijden van het weekend ervoor of de jaarlijkse ITF-cup. Ik bedank Gerard Meijer voor zijn gouden tip om onderzoek te gaan doen in de groep van Henk. Ook bedank ik Gerard, Bretislav Friedrich en de rest van de Koude Moleculen Groep voor de gastvrijheid gedurende mijn meerdere uitjes naar Berlijn. Tot slot wil ik alle collega's van het ITF bedanken voor de leuke sfeer, de gezellige lunches en de

goede ondersteuning.

Let me now switch to English to thank all my foreign colleagues in Utrecht and from all over the world. First of all, I express my gratitude to Lih-King Lim, with whom I shared many fun discussions and summer schools over the years. I thank Achilleas Lazarides and his significant other, Bert van Schaeybroeck, for sharing their talent in science and consumption of Belgian beers. I thank the post-docs in the Quantum Fluids Group, namely Masud Haque and Pietro Massignan, as well as Rachel Maitra, my shiny officemate the last year. I am grateful to Cristiane de Morais-Smith for her careful reading of my thesis and for letting me be an assistant in her statistical field theory course. I thank the experimentalists in our field for performing beautiful experiments, and especially Randy Hulet for many invaluable discussions over the years. I am also grateful to John Gaebler and Jayson Stewart from Deborah Jin's group, and Yong-Il Shin from Wolfgang Ketterle's group for sharing their experimental data. I thank Carlos Lobo and Alex Gezerlis for the data of their Monte-Carlo calculations. Finally, I had a lot of fun during many (inter)national conferences, workshops and summer schools. Thanks to everybody for those great times.

Naast de steun binnen de wetenschappelijke wereld kwam er ook veel steun van buiten de wetenschappelijke wereld. Ik bedank mijn familie en vrienden voor hun oprechte poging om te begrijpen waar ik mee bezig was, en voor alle mooie momenten die we al sportend, stappend, wandelend, pratend, etend, drinkend en reizend samen meemaakten. In het bijzonder geldt dit voor mijn fantastische ouders, van wie ik heel veel hou. Dan blijft er nog één iemand over: lieve Roos, bedankt voor je onvoorwaardelijke steun en liefde de afgelopen vier jaar. Steeds stelde je op het juiste moment de juiste vraag ("Waar deed je ook alweer onderzoek naar?"), en liet je me genieten van alle dingen die het leven naast een promotie mooi maken. Het laatste gaan we twee maanden lang voortzetten in Zuid-Amerika, waarna een heel nieuw leven samen begint. Ik heb er nu al zin in.

Curriculum Vitae

Koos Gubbels werd geboren op 27 augustus 1982 in Tilburg. Het Voorbereidend Wetenschappelijk Onderwijs doorliep hij op het Jacob-Roelandslyceum te Boxtel, waar hij in 2000 het gymnasiumdiploma behaalde. Vervolgens studeerde hij natuur- en sterrenkunde aan de Radboud Universiteit Nijmegen. Zijn afstudeeronderzoek verrichtte hij onder begeleiding van prof. dr. Bretislav Friedrich en prof. dr. Gerard Meijer aan het Fritz-Haber-Institut der Max-Planck-Gesellschaft in Berlijn. Het onderwerp was een theoretische beschrijving van het Stark-afremproces, dat gebruikt wordt om de snelheid van polaire moleculen nauwkeurig te manipuleren. In januari 2006 studeerde hij cum laude af in de richting Theoretische Natuurkunde.

Na zijn studie startte hij met zijn promotieonderzoek onder begeleiding van prof. dr. ir. Henk Stoof aan het Instituut voor Theoretische Fysica van de Universiteit Utrecht. Het promotieonderzoek heeft onder andere geleid tot dit proefschrift. Ook begeleidde hij de werkcolleges van de vakken Thermische Fysica 2 en Statistische Veldentheorie. Voor het laatste vak heeft hij samen met Dennis Dickerscheid en Henk Stoof een tekstboek geschreven, getiteld *Ultracold Quantum Fields*. Gedurende zijn promotie heeft hij deelgenomen aan verschillende conferenties, workshops en zomerscholen, waaronder de 'International School of Physics "Enrico Fermi" Course CLXIV' in Varenna en de 'BEC 2009'-conferentie in Sant Feliu. Hij presenteerde zijn onderzoeksresultaten op diverse gelegenheden in binnen- en buitenland. Bovendien zit hij in de redactie van het Nederlands Tijdschrift voor Natuurkunde.

Naast deze wetenschappelijke activiteiten is Koos ook geïnteresseerd in politiek. Hij is daarom actief lid van de Partij van de Arbeid. Ook heeft hij meegedacht aan de ontwikkeling van een leiderschapsprogramma voor jonge mensen, genaamd 'Young CALL', en deelgenomen aan de proefversie. Tot slot houdt hij zich in zijn vrije tijd bezig met zaalvoetbal, wielrennen en het verkennen van de wereld.